Geology and Mineralogy Research Developments

Crystals and Crystal Growth

Wilfred Carter
Editor

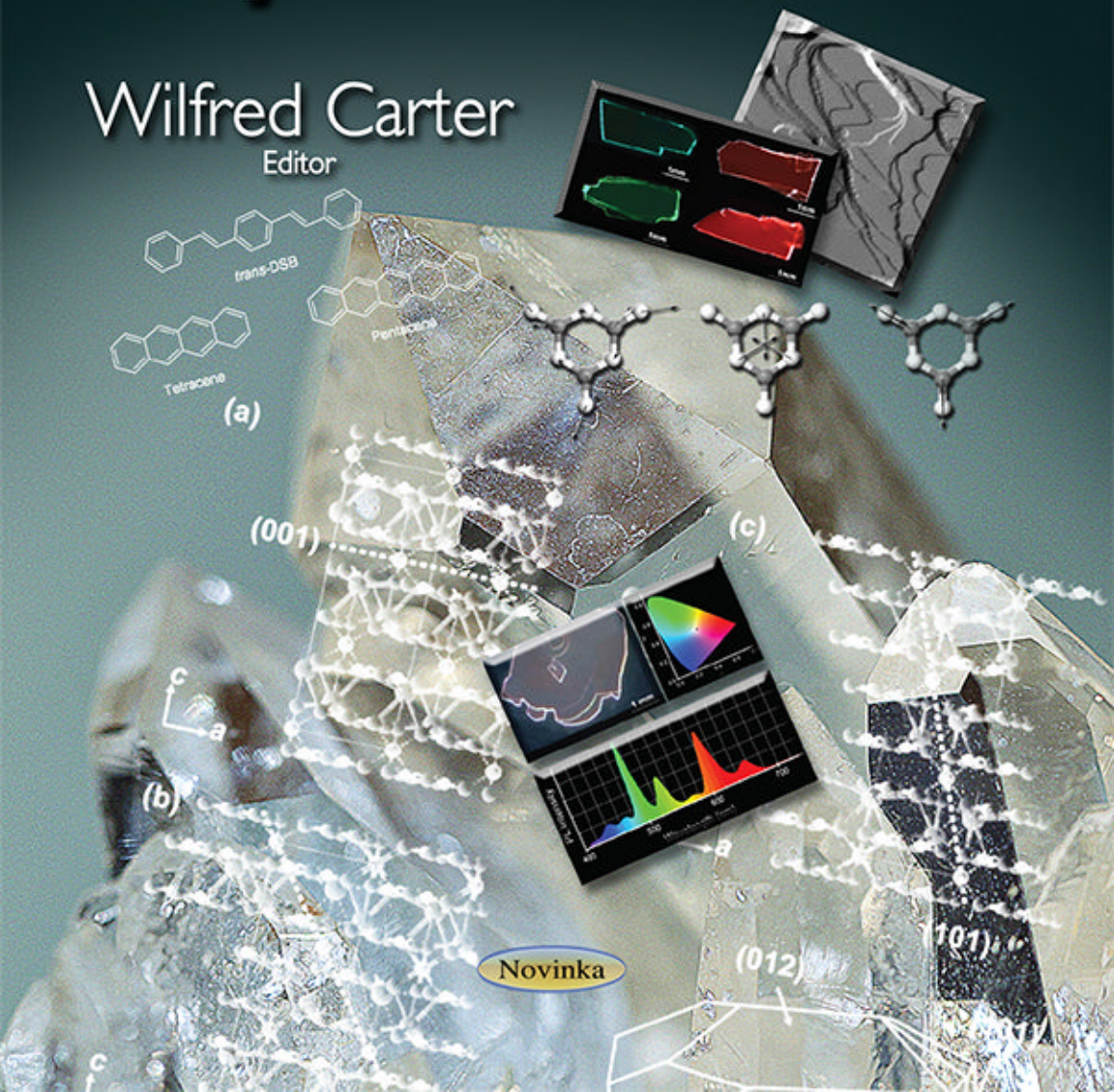

Novinka

GEOLOGY AND MINERALOGY RESEARCH DEVELOPMENTS

CRYSTALS AND CRYSTAL GROWTH

No part of this digital document may be reproduced, stored in a retrieval system or transmitted in any form or by any means. The publisher has taken reasonable care in the preparation of this digital document, but makes no expressed or implied warranty of any kind and assumes no responsibility for any errors or omissions. No liability is assumed for incidental or consequential damages in connection with or arising out of information contained herein. This digital document is sold with the clear understanding that the publisher is not engaged in rendering legal, medical or any other professional services.

GEOLOGY AND MINERALOGY RESEARCH DEVELOPMENTS

Additional books in this series can be found on Nova's website under the Series tab.

Additional e-books in this series can be found on Nova's website under the e-book tab.

GEOLOGY AND MINERALOGY RESEARCH DEVELOPMENTS

CRYSTALS AND CRYSTAL GROWTH

WILFRED CARTER
EDITOR

New York

Copyright © 2015 by Nova Science Publishers, Inc.

All rights reserved. No part of this book may be reproduced, stored in a retrieval system or transmitted in any form or by any means: electronic, electrostatic, magnetic, tape, mechanical photocopying, recording or otherwise without the written permission of the Publisher.

For permission to use material from this book please contact us:
nova.main@novapublishers.com

NOTICE TO THE READER

The Publisher has taken reasonable care in the preparation of this book, but makes no expressed or implied warranty of any kind and assumes no responsibility for any errors or omissions. No liability is assumed for incidental or consequential damages in connection with or arising out of information contained in this book. The Publisher shall not be liable for any special, consequential, or exemplary damages resulting, in whole or in part, from the readers' use of, or reliance upon, this material. Any parts of this book based on government reports are so indicated and copyright is claimed for those parts to the extent applicable to compilations of such works.

Independent verification should be sought for any data, advice or recommendations contained in this book. In addition, no responsibility is assumed by the publisher for any injury and/or damage to persons or property arising from any methods, products, instructions, ideas or otherwise contained in this publication.

This publication is designed to provide accurate and authoritative information with regard to the subject matter covered herein. It is sold with the clear understanding that the Publisher is not engaged in rendering legal or any other professional services. If legal or any other expert assistance is required, the services of a competent person should be sought. FROM A DECLARATION OF PARTICIPANTS JOINTLY ADOPTED BY A COMMITTEE OF THE AMERICAN BAR ASSOCIATION AND A COMMITTEE OF PUBLISHERS.

Additional color graphics may be available in the e-book version of this book.

Library of Congress Cataloging-in-Publication Data

Crystals and crystal growth / Wilfred Carter, editor.
pages cm. -- (Geology and mineralogy research developments)
Includes index.
ISBN: 978-1-63463-822-7 (eBook)
1. Crystals. 2. Crystal growth. 3. Crystallography. I. Carter, Wilfred, 1964- editor.
QD921.C865 2014
548--dc23
2014047568

Published by Nova Science Publishers, Inc. † New York

CONTENTS

Preface		**vii**
Chapter 1	Hydrothermal Crystal Growth from SiO_2 - GeO_2 Solid Solution for Piezoelectric Applications *Mythili Prakasam and Alain Largeteau*	**1**
Chapter 2	*In-Situ* Investigation of the Melt Structures in Borate Crystal Growth Systems *Songming Wan*	**25**
Chapter 3	Doped Organic Crystals with High Efficiency, Color-Tunable Emission toward Laser Application *Yang Zhao and Huan Wang*	**53**
Chapter 4	Modeling Effects of Impurities on Crystal Growth *Issam A. Khaddour*	**71**
Index		**93**

PREFACE

This book discusses several crystals and the crystal growth processes.

Chapter 1 - Hydrothermal crystal growth offers a complementary alternative to many of the classical techniques of crystal growth used to synthesize new materials and grow bulk crystals for specific applications. This specialized technique is often capable of growing crystals at temperatures well below their melting points and thus potentially offers routes to new phases or the growth of bulk crystals with less thermal strain. The hydrothermal process is utilized for growing a wide variety of crystals. Wide field applications such as actuators, high frequency stability with frequency and time control circuits, radio frequency low pass filters for video and digital cameras, initiated research in quest of piezoelectric materials. Currently [Pb (Zr, Ti) O_3] is widely used in piezoelectric materials in the limited temperature range (< 350^oC). Due to lead (Pb) toxicity, researchers worldwide are looking for an alternative. Though alkali niobates could be one of the viable candidates, its low melting point and high volatilization results in inhomogeneity in the grown crystals. Silicon oxide (SiO_2) with α-quartz structure are the current frontrunners for piezoelectric applications due to its high electromechanical coupling co-efficient and Germanium Oxide (GeO_2) is expected to be very interesting but the process to obtain large single crystal is yet to be realized. It is impossible to obtain large crystals of SiO_2 and GeO_2 by conventional crystal growth techniques. However with hydrothermal crystal growth, where the crystal growth is carried out under sub/super critical conditions by varying temperature and pressure, helps in obtaining single crystals at medium temperature. The various parameters and their physico-chemical kinetic processes in obtaining crystals α-quartz of SiO_2 and GeO_2 by hydrothermal

crystal growth will be discussed in detail with a detailed literature review in this chapter.

Chapter 2 - Borate crystals are widely used as nonlinear optical, laser and luminescent materials due to their diversified structures, and good chemical and physical properties. The growth of high-quality borate crystals is required for their applications. A fundamental problem for borate crystal growth is the high-temperature melt structures in the crystal growth systems. They are related not only to the macro-properties of the melts, but also to the micro-processes of the crystal growth. However, the borate melt structures have been poorly understood because of the structural complexity, and the lack of effective experimental techniques and theoretical analysis methods. High-temperature Raman spectroscopy is a powerful tool for the study of borate melt structures, and has been applied to *in-situ* investigate the melt structures in the $Ba_2Mg(B_3O_6)_2$, BaB_2O_4, CsB_3O_5, LiB_3O_5, BiB_3O_6, and $Li_2B_4O_7$ crystal growth systems. Alkali-earth cations and $[B_3O_6]^{3-}$ rings, as the structural units, have been found in the $Ba_2Mg(B_3O_6)_2$ and BaB_2O_4 melts. A boundary layer in which the melt structure gradually changes to the crystal structure has been observed around the LiB_3O_5 or β-BaB_2O_4 (low-temperature phase BaB_2O_4) crystal−solution interface. An isomerization reaction between $[B_3O_3Ø_4]^-$ (Ø = bridging oxygen atom) rings and $[B_3O_4Ø_2]^-$ rings has been found in the CsB_3O_5 or LiB_3O_5 boundary layer, and applied to understand the two crystal growth mechanisms and habits. On the basis of the structural evolution around the growing BiB_3O_6 and $Li_2B_4O_7$ crystals, two polymer-like structural models have been proposed to describe the BiB_3O_6 and $Li_2B_4O_7$ melt structures. The density functional theory (DFT) calculation, as an effective theoretical method, verified the melt structural models, and gave clear assignments of all important vibrational peaks in the melt Raman spectra.

Chapter 3 - Tetracene or pentacene -doped *trans*-1,4-Distyrylbenzene (*trans*-DSB) crystals with high crystalline quality, high doping ratio, large size and excellent optical properties were prepared by physical vapor transport method. Efficient energy transfer from the host *trans*-DSB molecules to the guest molecules and the suppressing of the interaction among the guest molecules lead to color-tunable emission and high luminescent efficiencies. These doped crystals maintain the ordered layer structures and the crystal surface continuities, which are verified by X-ray diffraction (XRD) and atomic force microscopy (AFM) analysis. Further, the white-emission tetracene and pentacene -doped *trans*-DSB crystal with the CIE coordinate (0.36, 0.37) has been obtained by controlling an appropriate mol ratio of guest to host (tetracene: pentacene: *trans*-DSB= 1: 1.35: 23.1).

The primary results of optically pumped laser experiment indicate that these crystals have the potential application for organic laser diodes.

Chapter 4 - This chapter represents specific review on the effects of impurities on the growth from solution. The concept of the impurity partition coefficient and its importance to the recrystallization processes is explained. Further, Kubota-Mullin model as adsorption model describing the effect of the shape, the size and the orientation of the impurity at the interface layer is reviewed, and discussed for the specific cases of sucrose grown from raffinose-doped solutions. Furthermore, benefiting of application of the 2D nucleation models, namely the birth and spread model, to understand the effects of impurities on the kinetics and the interfacial free energy of growth is also illustrated, and deeply discussed. Finally, a hypothetical approach is presented to enable evaluating the effect of macromolecular additives on the occurrence of needle-like crystals.

In: Crystals and Crystal Growth
Editor: Wilfred Carter
ISBN: 978-1-63463-791-6
© 2015 Nova Science Publishers, Inc.

Chapter 1

HYDROTHERMAL CRYSTAL GROWTH FROM SiO_2 - GeO_2 SOLID SOLUTION FOR PIEZOELECTRIC APPLICATIONS

Mythili Prakasam* *and Alain Largeteau***
CNRS, Université de Bordeaux, ICMCB, Pessac, France

Dedicated to Professor Gerard Demazeau on the occasion of his Lifetime Achievement Award in ISHA 2014 for his scientific contribution in high pressure research

ABSTRACT

Hydrothermal crystal growth offers a complementary alternative to many of the classical techniques of crystal growth used to synthesize new materials and grow bulk crystals for specific applications. This specialized technique is often capable of growing crystals at temperatures well below their melting points and thus potentially offers routes to new phases or the growth of bulk crystals with less thermal strain. The hydrothermal process is utilized for growing a wide variety of crystals. Wide field applications such as actuators, high frequency stability with frequency and time control circuits, radio frequency low pass filters for video and digital cameras, initiated research in quest of piezoelectric materials. Currently [Pb (Zr, Ti) O_3] [1, 2] is widely used in piezoelectric materials in the limited temperature range (< 350^{o}C). Due to lead (Pb)

* Corresponding author: prakasam@icmcb-bordeaux.cnrs.fr/ mythili.prakasam@gmail.com.

toxicity, researchers worldwide are looking for an alternative. Though alkali niobates could be one of the viable candidates, its low melting point and high volatilization results in inhomogeneity in the grown crystals. Silicon oxide (SiO_2) with α-quartz structure are the current frontrunners for piezoelectric applications due to its high electromechanical coupling co-efficient and Germanium Oxide (GeO_2) is expected to be very interesting but the process to obtain large single crystal is yet to be realized. It is impossible to obtain large crystals of SiO_2 and GeO_2 by conventional crystal growth techniques. However with hydrothermal crystal growth, where the crystal growth is carried out under sub/super critical conditions by varying temperature and pressure, helps in obtaining single crystals at medium temperature. The various parameters and their physico-chemical kinetic processes [3, 4] in obtaining crystals α-quartz of SiO_2 and GeO_2 by hydrothermal crystal growth will be discussed in detail with a detailed literature review in this chapter.

1. INTRODUCTION

Long range atomic order with repetitive structure gives rise to crystalline form. Crystal growth is the result of phase transformations involving solid→ solid, liquid→ solid or vapor→ solid. In general crystal growth methods are classified into solution growth and melt growth techniques. These crystal growth methods are classified on the type of crystallization and one amongst them is the solution growth. Solution growth can be classified into low temperature solution growth and high temperature solution growth. Melt growth is divided into Czochralski, Bridgman-Stockbager and Verneuil methods. In all the aforesaid techniques, the starting components are melted congruently and then solidified with a controlled cooling and pulling and/or rotation rate. Under melt growth techniques the material is subjected to very high temperatures in order to melt, which could be detrimental for the compounds that is prone to phase transitions and thermal stability or decomposition. Viscosity of melt is another important factor, which could lead the formed product to be amorphous rather than the single crystal. In solution growth, dissolving the solute components in liquid medium or flux is crystallized from supersaturated solutions by decreasing the temperature (at ambient pressures). Crystal growth under high pressure and high temperatures called as hydrothermal method is a solution growth where pressure improves the dissolution phenomenon.

The crystal growth under medium temperature under high pressure is done by means of hydrothermal method. Hydrothermal method can be classified under medium temperature solution growth, which is primarily employed for the materials which has low solubility and undergoing various phase transitions at ambient pressure and even at high/low temperature. The origin of the term Hydrothermal originates from the usage of aqueous solution as solvent. However, in practice there are some of the non-aqueous solutions that are used as solvents, which are called as Solvothermal method. Conventionally hydrothermal method is used to initiate heterogeneous chemical reactions(between solid and liquid phases) in the presence of aqueous solvents under high pressure at medium temperature, which dissolves the solute particles and is capable of precipitating the dissolved solute particles with a temperature gradient which is impossible to obtain under ambient pressure and temperatures. During 18^{th} century, many European mineralogists succeeded in employing hydrothermal technique to obtain minerals. Various groups of materials such as phosphates, arsenates, titanates, nitrides, carbides, vanadates, germanates, tungstates, fluorides, oxides, sulfides, silicates and various organic/ bio materials have been obtained by hydrothermal technique. Hydrothermal process also helps in obtaining new phases of chemical materials with chemical stability, fabrication of nanoparticles with defined size and morphology, decomposition, corrosion and etching of the materials are reported. Initially water was the only liquid that was considered for usage in the hydrothermal method, which resulted in very small size crystals, owing to the inherent low solubility of the solute. This resulted in searching for new solvents other than water. A detailed explanation on the hydrothermal technique for crystal growth is discussed in the following section.

2. HISTORICAL ASPECTS OF HYDROTHERMAL CRYSTAL GROWTH

Hydrothermal method gained popularity in the initial 19^{th} century for the production of quartz single crystals. The first work of crystal growth of α-quartz was carried out by Schafhault and Senarmont in the order of size microscopic. G. Spezia [5] developed a crystal growth technique during 1898 and 1908 with a sealed vessel by incorporating the solution of sodium silicate and natural quartz. The sealed vessel was heated to $350^{o}C$, which lead to obtain crystals of dimensions ~ 15 mm over a period of 7 months; hence the

hydrothermal process was invented. The difficulty to obtain natural quartz for piezoelectrical applications during the second world war lead to the active research for looking into alternative methods to obtain single crystals of Quartz. Currently the technology of α- quartz crystal growth is well developed and is industrialized in various countries across the globe. Hydrothermal crystal growth is preferred generally to obtain large and defect free single crystals (mostly the materials that present structural transitions). Various applications such as piezoelectric, optical, magnetic and biomedical require large defect free crystals that are usually grown by hydrothermal method. Hydrothermal method [6-9] is preferred and is advantageous over other conventional crystal growth techniques due to the following

1. Syntheses of the metastable compounds
2. Stabilization of required oxidation states for the metal compounds
3. Helpful in obtaining the compounds which undergo low temperature phase transitions

As all the reaction kinetics takes place in the closed system at various pressure and temperature (subcritical and supercritical condition), it is possible to define the influence of pressure, temperature and various chemical components in the formation of the chemical components. Benefits of hydrothermal processing also include powder preparation (non-agglomerated, controlled morphology) and reactive sintering to obtain new phases at comparatively low temperatures and high pressures.

Hydrothermal sintering involves the processing of organic/ inorganic compounds, which could undergo thermal decomposition at high temperatures to obtain dense or porous material with distinct microstructures.

3. HYDRODYNAMIC ASPECTS OF HYDROTHERMAL CRYSTAL GROWTH

The basic aspects that are considered during hydrothermal growth are

(1) Wide range of temperature and pressure conditions for various aqueous solutions and their physico-chemical studies are studied.
(2) Effect of the temperature and pressure to yield the single crystals by hydrothermal method

Hydrothermal crystal growth experiments are usually carried in vessels with a gradient of temperature. Regarding the growth of the single crystals by hydrothermal method either by homo/ hetero epitaxial techniques are carried out in the different ways such as

(i) Dissolution of the required starting components (nutrient) in mono/ polyphasic components by convective mass in the dissolution zone transfer reaches in the growth zone and helps in interaction of the dissolved components to deposit the layer on the seed surface.
(ii) Recrystallization of the solute from the saturated solution under sub/supercritical conditions, where the solute transport or deposition occurs by convective mass transfer.

Deviations from Raoult's law takes place when there is a strong interaction between the solute and the solvents. These interactions lead to acquiring knowledge on the influence of the solution components such as type of solvents, their concentrations, and solubility under a particular hydrothermal process. In addition, influence of the starting component (nutrient), final composition of the product, kinetics and growth mechanisms of the single crystals can be studied by the aforesaid interactions.

The change in the thermodynamical system can be elucidated by the change in Gibb's free energy, when the transition from one solvent to another which is shown by the following equation

$$\Delta G = \Delta H - T\Delta S = RT\ln K \rightarrow \quad (1)$$

Where K is equilibrium constant.

It can be observed from equation 1 that the solubility influences the enthalpy and entropy of the system (at constant Pressure "P" and Temperature "T") is different for different solvents. Further solubility of various solutes change according to the solvent used, hence the hydrothermal conditions are different for different kind of compounds. The different aspects of solvents in hydrothermal system are discussed in the following section.

4. HYDROTHERMAL SOLVENT BEHAVIOUR

The synthesis and recrystallization of various compounds and fabrication as single crystals on the seed depends on its chemical and physical properties. Under the hydrothermal conditions, the solubility depends on the type of solvent at different P and T. But the solvent have to be chosen for each compound system based on its solubility and various physico-chemical aspects with changing temperature or pressure. Further it is essential to know the absolute solubility of the crystallizing material and viscosity of the solvent which should have insignificant toxicity and inert with the internal wall of the autoclave (vessel).

Hydrothermal solvent depend on viscosity, dielectric constant, compressibility and co-efficient of expansion. Since solvent viscosity and diffusion are inversely proportional to each other, it leads to rapid diffusion in hydrothermal growth which in turn gives rise to single crystals of well-defined morphology. The higher growth rates can be expected if there is a narrow diffusion zone near the growth interface, which will cause constitutional supercooling and gives rise to dendritic growth. Various mineralizers which help to amplify the dissolution effect such as sodium hydroxide (NaOH), sodium carbonate (Na_2CO_3), Ammonium Fluoride (NH_4F), Potassium hydrogen phosphate (K_2HPO_4) etc., For ex., when 1M NaOH is prepared at room temperature, the viscosity of the hydrothermal solutions reduces to about two orders of magnitude lower than that of ordinary solutions. The above phenomenon can be understood in terms of the thermodynamical and transport properties of supercritical water, which is conversely different than the properties of water at ambient conditions.

In hydrothermal process, as we discussed above the supercritical water acts as a unique medium that accelerates the chemical process of the constituent solute system. The solubility of nonpolar species increases in-contrast to the ionic and polar species which decreases as a result of the solvent polarity. However, the molecular mobility increases due to the decrease in the solvent viscosity. Under hydrothermal conditions, there are drastic changes that lead to ionic hydration, which reduces the dielectric constant and density. Consequently, drastic change in dielectric constant at high pressure and high temperature leads to complete dissociation of electrolyte at ambient temperatures and ambient pressure to be highly associated in the supercritical region. Large compressibility is obtained as a result of hot and less dense fluid. This compressibility is an important factor that is used in the calculation of density change with pressure. In addition the

role of thermal expansion co-efficient is indispensible as an important parameter that helps in obtaining defect free and strainless crystals by hydrothermal technique.

Co-efficient of expansion of water under hydrothermal conditions is large. Supercritical water is obtained above critical temperature (T_c= 374.2^{o}C) and critical pressure (P_c= 22.1 MPa). At the critical point, the phases of liquid and gas are not distinguishable. There are various reports that show the variation of water under ambient/high pressure and ambient/high temperature conditions, which is believed to have played a significant role in the origin of life on earth.

The supersaturation that is established in the hydrothermal system is dependent on the magnitude of the temperature gradient (ΔT) between the dissolution and growth zones. Growth rate is determined by the ratio of increase of seed size and duration of the experiment run. The growth rate increases linearly with supersaturation leading to deposition on each face of the seed, irrespective of the chemical constituents in the hydrothermal system. Significant difference in the crystallization rate on each face shows the primary role of surface processes that take place at the crystal solution interface. Crystallization rate can increase in two ways (i) With system that contains the solvent components, the rate increases sharply at low concentrations and remains practically unchanged at high concentrations and (ii) An increase in growth rate on the faces is observed with the increase in pressure which help to improve the dissolution of the nutrient. Though pressure doesn't have any direct effect on the growth rate of the crystals, it has significant influence on other parameters such as mass transfer and solubility.

5. CRYSTAL GROWTH BY HYDROTHERMAL

Hydrothermal crystal growth method is more analogous to crystal growth from aqueous solution at ambient temperature. Hydrothermal crystal growth is done in a closed vessel under pressure called "vessel". Based on the pressure that is desired in vessel different types of materials are chosen such as glass vessels (low pressures), steel vessels (medium pressures), welded sealed vessel, modified Bridgman and cone enclosure (high pressures). The schematic representation of hydrothermal method is shown in figure 1. The vessel is divided into two zones: (a) dissolution zone and (b) growth zone. If the material has positive solubility, then the charge (nutrient) material is placed in the bottom of the vessel (warm zone), and the seed is suspended in

the top of the vessel, (cool zone) r. In the case of negative solubility of material, the nutrient is at the top (cool zone) and the seed is at the bottom of the vessel (warm zone). The required quantity of aqueous solution is filled in the vessel according to the pressure and temperature required following the thermodynamical conditions desired. The vessel is heated in order to obtain the required temperature gradient. This temperature gradient helps in transporting the solute molecules from the warm zone to the cold zone by the convection process. Thermodynamical parameters such as P, T and ΔT govern to determine the crystal growth rate in addition to the diaphragm opening and the type of solvent used. Table 1 shows the general conditions employed in industries for the growth of α-Quartz crystals. The vessels are constructed in such a way that is capable to work both at high and low pressures. The vessels are made to withstand the various constraints such as pressure, temperature and aggressive fluids over a long period of time. So the material constituting the vessel should have adaptable characteristics. Most of the industrial vessels are made in steel. It is well known that the steel is an alloy based on Iron "Fe" which could react with the solute upon reaction with aggressive solvents.

Table 1. Thermodynamical parameters employed in industries for SiO_2 single crystals

Parameters	High pressure	Low pressure
Temperature	360°C	345°C
Pressure	150 MPa	70-100 MPa
Gradient	25°C	10°C
Solvent	NaOH 1M	Na_2CO_3 0.8M
Crystal growth rate	1 mm/day	0.4 mm/day

This is mostly observed in case of α-quartz crystal growth in the form of thin layer of acmite ($NaFeSi_2O_6$) on the internal wall of vessel, which is very difficult to remove when once formed. This makes passivation cycle necessary before using autoclave for the crystal growth; else this layer becomes too thick. When acmite is thick inside the vessel, it will lead to problem for experiment processing.

6. α-QUARTZ –GENERAL PROPERTIES AND APPLICATIONS

SiO_2 is found both in crystalline and amorphous form in nature. There are about 22 polymorphic modifications with three principal crystalline forms of SiO_2 such as Quartz, Tridymite and Cristobalite. α-Quartz crystal structure can be defined as tetrahedral arrangement with silicon surrounded by four oxygen atoms (Figure 2 (a)). Each silicon atoms are bonded to 4 oxygen atoms. Most oxygen atoms will be bonded to silicon atoms, so that two tetrahedral are joined at a corner. The bond angles around O-Si-O are essentially the tetrahedral angle, 109^o; the Si-O distance is 1.61 Å, (0.16 nm) with very little variation. It is the oxygen bonds between silicon atoms that give SiO_2 many of its unique properties. The bond angle Si-O-Si is nominally about 145^o, but can vary from about 100 to 170^o with very little change in bond energy. Furthermore, rotation of the bond about the axis is almost completely free (Figure 2(b)).

The stability of each of the structural forms of Quartz is different and well defined under equilibrium conditions. Figure 3 shows the phase diagram of SiO_2. High temperature forms of cristobalite and Tridymite can exist in metastable state below its transition temperature. Each crystalline form of quartz, metastable tridymite and metastable cristobalite consists of high and low temperature structural forms called as β and α, respectively. α-Quartz is stable up to 573^oC and is widely used for various technological applications such as piezoelectrics. The low temperature transition from α-β, makes the fabrication of α-Quartz crystals impossible by conventional crystal techniques. The high temperature crystal growth techniques cause cracks on the surface of the crystals which is due to the phase transitions during cooling. Hence hydrothermal crystal growth method is considered to be an apt technique to grow these crystals.

α-Cristobalite is a polymorphic form of silica which has higher solubility than quartz. α-Cristobalite has advantages such as availability in high purity state and can be prepared with relative ease of particles with uniform size. The solubility of quartz in pure water is found to be low for crystal growth (~ 0.1-0.3 wt %), but the solubility could be markedly increased by the addition of OH-, Cl-, F-, Br-,I- and acid media. A slight increase in molarity can accelerate the growth rate of the crystal, where as a large increase in molarity gives rise to additional chemical phases which could deposit at the bottom of vessel that inhibits the solute to be transported to the crystal growth zone. The

minimum molarity that has been studied to result in good growth rate is about 0.25 M NaOH.

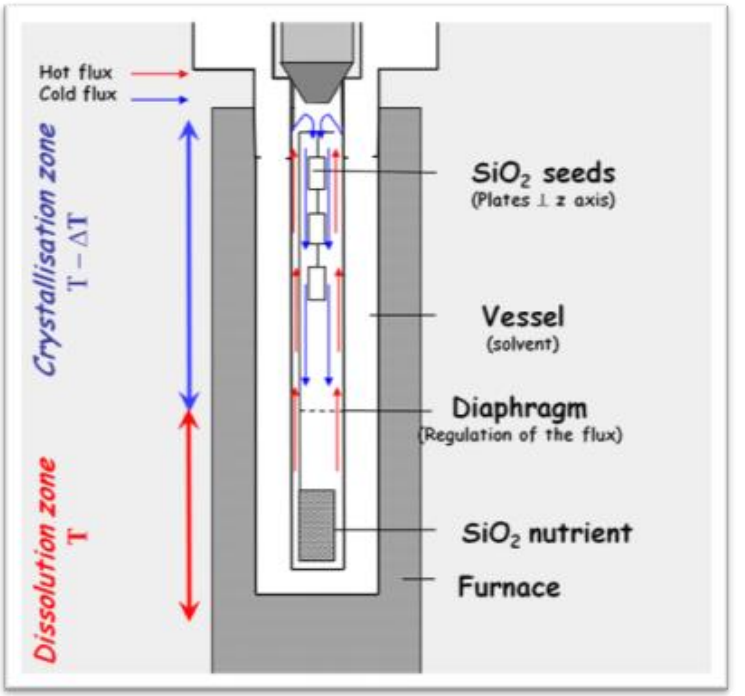

Figure 1. Schematic representation of hydrothermal crystal growth.

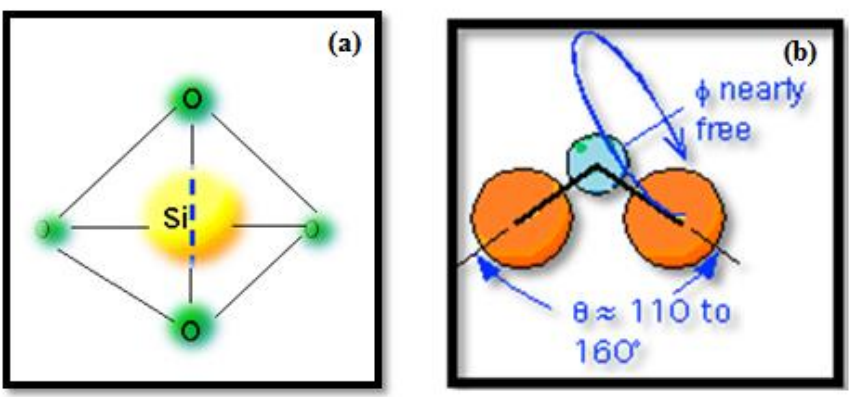

Figure 2. Crystal structure of α-quartz SiO_2 and bond rotation angles in α-quartz SiO_2.

α-Quartz is one of the stable materials used in electronics industry due to its high chemical stability, piezoelectricity and high mechanical strength. Figure 4 shows the various applications of quartz in devices. With its high Q-factor at resonance and low manufacturing costs in addition to the aforesaid properties made Quartz as one of the principal material in employing in frequency controlling devices in electronic equipment. Quartz is also widely known to be a piezoelectric material which exhibit electric charge upon subjecting to pressure. Crystalline quartz with its low temperature co-efficient will lead to a small change in resonant frequency with any difference in temperature with high Q factor at resonance. Presence of any defects such as impurities, cracks or air bubbles significantly reduces the Q-factor. With the help of optimizing the crystal growth parameters it is possible to avoid the defects that are observed in the natural crystals (in terms of composition and structure).

Most of the defects induced in the grown crystals also depend on the nutrient used or solvent used. The defects are also induced from the chemical corrosion caused on the internal wall of vessel depending on the solvent and the metal of the vessel. Fluctuations in the thermodynamical parameters governing the crystal growth and inclusions of foreign particles lead to structural defects in Quartz. Presence of the defects in quartz crystals alters the device properties to a greater extent. Additional benefits of growing the crystals by hydrothermal method is that the crystal grows under less thermal strain and therefore it is possible to control the stoichiometry by producing in the oxidizing or reducing conditions by using some chemicals additive.

7. GERMANIUM OXIDE (GeO_2) CRYSTAL STRUCTURE

Germanium oxide [10-12] is an analogue of silicon oxide structurally and chemically. But it has to be noted that the phase diagram of GeO_2 has comparatively lesser number of structural polymorphs in comparison to SiO_2. The crystalline, glassy and liquid phases of GeO_2 when subjected to high pressures, the resulting changes occur at a comparatively lower pressure than their SiO_2 counterparts. Further variation in the size of Ge in comparison to Si and their relative bond lengths and bond angles are obvious. GeO_2 is also often related to its structure of oxides such as Borates (B_2O_3) other than SiO_2.

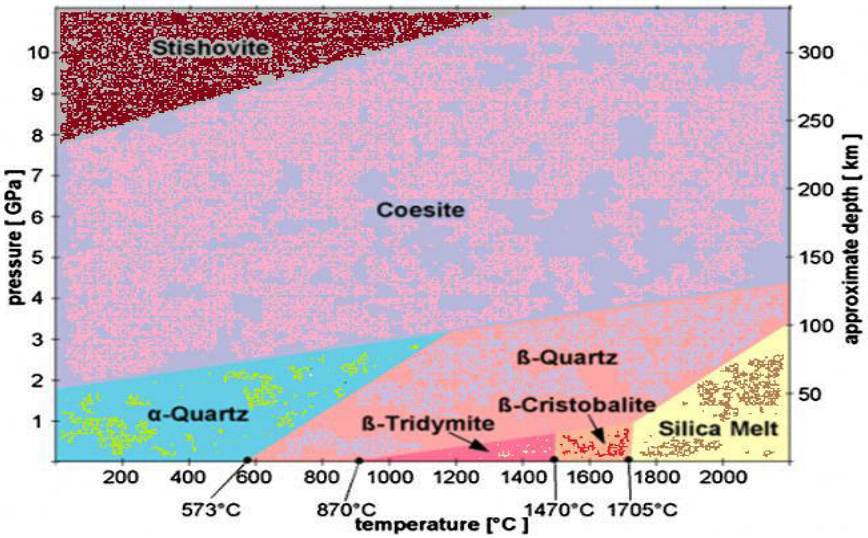

Figure 3. Phase diagram of SiO_2.

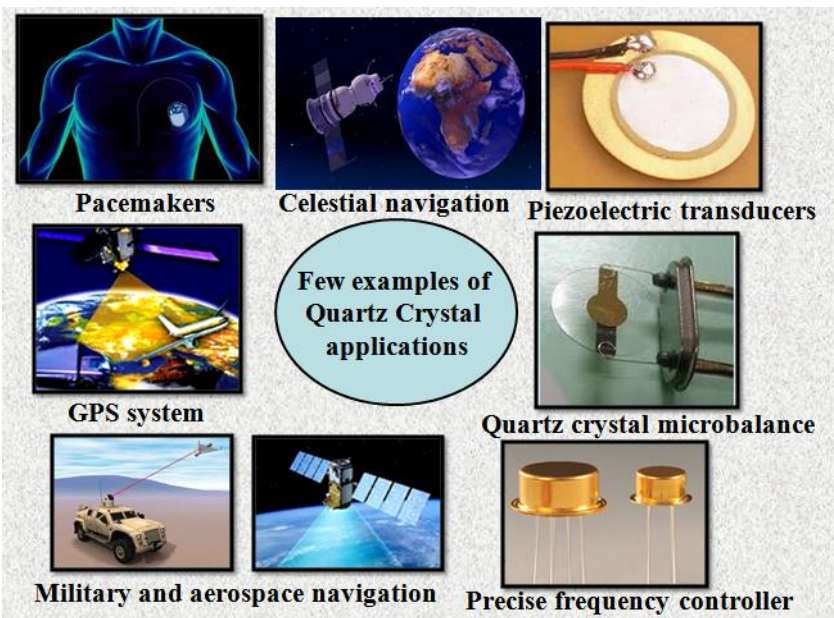

Figure 4. Few examples of Quartz crystal applications.

Crystalline GeO_2 has two structural polymorphs, such as α-quartz like ($P3_221$) trigonal (hexagonal) structure and Rutile type tetragonal ($P4_2/mnm$) structure. α-quartz like structure of GeO_2 has been demonstrated to exhibit stability at high temperature, but with basic differences in the structure. Structural difference essentially leads to the difference in the behavior of α-quartz SiO_2 and GeO_2 under high pressure, which arises from the rotation or tilting of the tetrahedral around the shared bridging oxygen. In particular, α-quartz like structure of GeO_2 undergoes the compression by tilting of the tetrahedral makes germanate structure to undergo the pressure induced transformations at lower pressure than the α-quartz structure. The aforesaid can be verified from the transformation of α-quartz to the high pressure Rutile structure results at 10 GPa, but the α-quartz like structure of GeO_2 occurs at 2 GPa. The atomic bridging structure of α-quartz GeO_2 is shown in figure 5.

8. SiO_2-GeO_2 Based Single Crystals by Hydrothermal Method

α-Quartz is the stable form of SiO_2 under the normal conditions of pressure and temperature. Natural quartz is found in the volcanic rocks and sediments. Natural Quartz is prevalently found in Russia, Brazil and Madagascar. Natural quartz have coloration such as brown, black, blue, pink and yellow due to the presence of various impurities substituting Si^{4+} by atoms such as Li, Na, H, Al, Ti or Co. These types of colored quartz crystals are prevalently used for ornamental purposes. When the quartz crystals are colorless, defectless and transparent, it present a great interest for wide variety of technological applications such as electronics, piezoresonators, microwave wafers, sensors and oscillators. The aforesaid devices require quartz single crystals of very high quality, defect free and preferentially oriented, which are extremely difficult to obtain naturally. The quartz crystals of average quality are mostly used for fabrication of watch and ornaments, and the crystals of high quality are used for spatial and military applications. Excellent crystal quality and its associated piezoelectric properties with little cost of fabrication make α-Quartz one of the widely used materials for application in piezoelectrics.

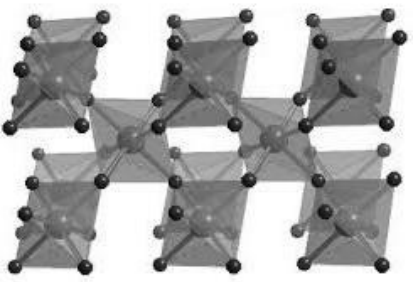

Figure 5. Atomic bridging structure in GeO_2.

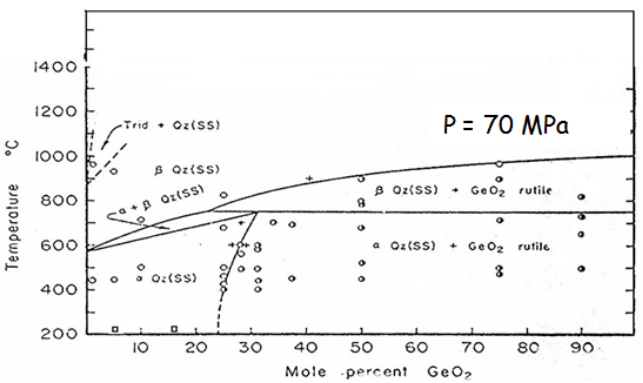

Figure 6. Phase diagram of SiO_2-GeO_2.

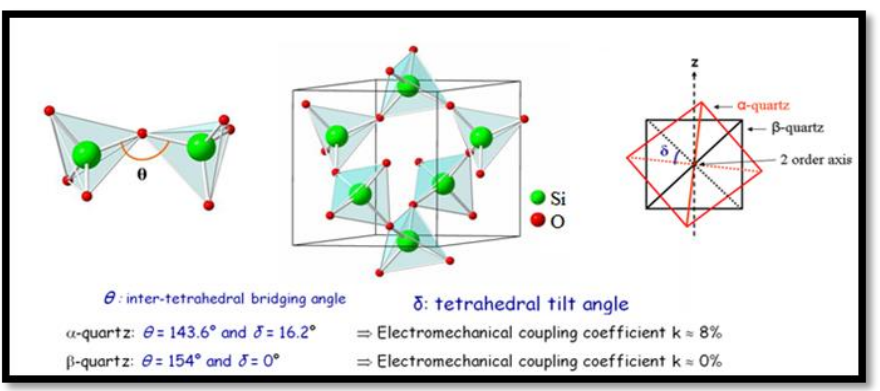

Figure 7. Variation of electromechanical coupling coefficient with inter-tetrahedral bridging and tilt angle in SiO_2.

Miller et al. [13] was the first to report on the phase diagram of SiO_2 and GeO_2 solid solutions (Figure 6). The solid solutions of different compositions were obtained by hydrothermal recrystallization with SiO_2 and GeO_2 precursors in sealed capsules at 700 bars. The maximum miscibility of germanium in the quartz lattice was found to be 31 % wt at 700^oC. If > 31% wt, Germanium appears in the form of rutile with co-ordination number 6, then the lattice of SiO_2 cannot accommodate Ge with co-ordination number 6 in thermodynamic conditions because the domain is biphasic. It has been verified by thermal analyses that the addition of germanium even in minute quantities such as 0.1 changes the transition temperature of $\alpha \longleftrightarrow \beta$ of Quartz from 573^oC to 660^oC.

In contrast to the well developed crystal growth technique of quartz, there are very few details on the growth of SiO_2-GeO_2 solid solution systems. The conventional reflux technique used for the growth of GeO_2 cannot be employed due to the poor solubility of SiO_2 under these conditions. On the other hand, traditionally used crystal growth method of quartz which necessitates the use of mineralizer will reduce the possible content incorporation of Ge in the SiO_2 matrix. Further due to the difference in the solubility limit of SiO_2 and GeO_2, it makes the growth of these crystals very delicate and complicated by the hydrothermal method. In addition, to date no structural refinement of the SiO_2-GeO_2 has been reported, which makes it even more complicated to know about the problems arising due to the inhomogeneity of the composition. Obtaining crystals of SiO_2-GeO_2 will not only help us to know the crystal chemistry but also to improve the piezoelectric properties by adjusting the concentration of Germanium in the lattice of quartz. Solubility of Quartz in water is low, hence mineralizers such as NaOH leads to the impurities such as sodium in the crystal. Quartz lattice is vulnerable to the substitution of ions which are similar to Si^{4+} in terms of ionic radii and valence state. Sometimes, substitution occurs also when the charge is different. Impurities can also enter the interstitially paving way to accommodate large ions to be placed in its structure. The ions such as Ge^{4+}, Sn^{4+}, B^{3+}, Al^{3+}, Ti^{4+}, Pb^{2+}, As^{5+}, Li^{+}, Ag^{+} and Zr^{4+} can be added to incorporate in quartz. The dopant in the quartz seems to enter the lattice either by substituting or in interstitial position.

In the family of materials such as XO_2 (X= Si, Ge) and MPO_4 (M= Fe, Al, Ga, B) family with α-quartz analogue, which is composed of either only XO_4 corner shared tetrahedral or both of MO_4 and PO_4 tetrahedra forming a trigonal system. Previous research works have confirmed experimentally that the large piezoelectric properties of α-$GaPO_4$ and α-GeO_2 materials in comparison to α-

SiO_2, α-$FePO_4$ and α-$AlPO_4$ compounds [14]. The aforesaid materials are directly related to their structural distortion with respect to the β- Quartz structure type. α-β phase transition which appears around 573°C in α-SiO_2 [θ=144.2°] does not occur when the tilt angle δ is over 22° (leading to θ under 136°] (Figure 7). Similarly α-β phase transition doesn't occur in α-GeO_2 and α-$GaPO_4$ Crystals. GeO_2 exhibits two forms of differing anion coordination around the central cation of α-Quartz type with trigonal structure and rutile type modification in Tetragonal structure. Natural GeO_2 is known to be more stable in rutile structure than in the trigonal structure. Under normal atmospheric pressure, the transformation from the rutile-like form to α-Quartz type has been reported to occur in the temperature range of 1024-1045°C. GeO_2 is in stable trigonal phase from 1033°C upto the melting point at 1116°C. GeO_2 crystals grown by hydrothermal method contains high OH inclusions which easily transforms into rutile like structure upon heating upto180°C.

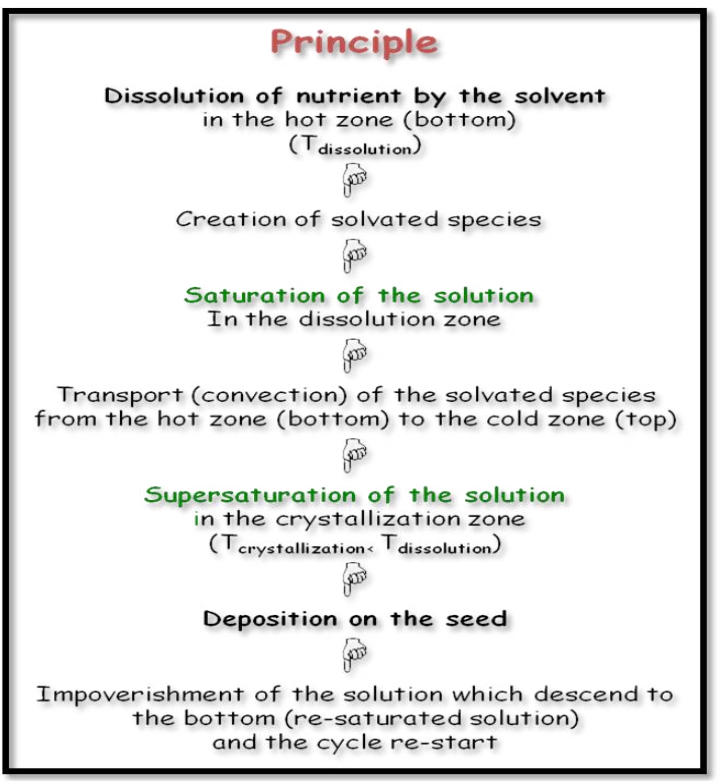
Principle
Dissolution of nutrient by the solvent
in the hot zone (bottom)
($T_{dissolution}$)
Creation of solvated species
Saturation of the solution
In the dissolution zone
Transport (convection) of the solvated species
from the hot zone (bottom) to the cold zone (top)
Supersaturation of the solution
in the crystallization zone
($T_{crystallization} < T_{dissolution}$)
Deposition on the seed
Impoverishment of the solution which descend to
the bottom (re-saturated solution)
and the cycle re-start

Figure 8. The general procedure for the single crystal growth by hydrothermal method.

Conditions for device fabrication of α-Quartz SiO_2 can also be considered valid for α-Quartz GeO_2 for piezoelectric applications. The substitution of Ge atoms in α-Quartz SiO_2 is believed to accentuate the piezoelectric properties and thermal stability of α-Quartz SiO_2. It has been reported that $Si_{0.93}Ge_{0.07}O_2$ has high piezoelectric co-efficient in comparison to SiO_2 [12]. It can be inferred from the phase diagram of SiO_2-GeO_2 that the maximum content of GeO_2 that can form single phase is 31 at % at about 700°C and 70 MPa under hydrothermal conditions. Hydrothermal quartz crystals are generally grown with NaOH (1M) and Na_2CO_3 (0.8M) at about 150 MPa and 360°C. However these conditions doesn't apply for $Si_{1-x}Ge_xO_2$ (SGO), because of the formation of sodium germanate. One of the possibilities to incorporate the higher germanium content in α-Quartz crystals of SiO_2 is by processing the crystal growth experiment at high pressure > 2500 bar and temperatures until 700°C with dilute aqueous alkaline or fluorides solutions. The aforesaid conditions are inappropriate to be employed to obtain large dimensions.

The single crystals of SGO with the α-Quartz type structure is obtained by using Nichrome alloy or stainless steel vessels. In order to avoid this problem, INCONEL 625 (Ni-58%, Cr-20%, Mo-8%, Co, Ta- 3.15% and Fe- 5% atomic) type of alloy is also used. This alloy is based on nickel with very minimum content of Fe, but has all the characteristics that are beneficial for quartz type crystal growth. INCONEL is highly resistive in the base medium, with high elastic constants and good stability of temperature. Design of the vessel geometry also plays a vital role in obtaining the temperature gradient. Other key points are windings for closing the vessel, slot for thermocouple passage and evacuation tube. The aforesaid are the prime places that lead to the leakage. To be leak proof, various types of joints are used, such as cone type gaskets and Bridgman type gaskets. The cone type of gaskets are scratch resistant whereas Bridgman type of gaskets are delicate to operate, extreme precaution should be taken. The 8 screws on top help the obturator to force it up and secure the gasket to be leak proof. Any problem with this closing system will lead to leakage. Though the gasket is sensible to scratches, this system is beneficial as more the pressure is increased more secure are the gaskets. The pressure and temperature are measured with the help of thermocouples and pressure sensors. There are security pressure leakage valves to open up on increase of pressure. By integrating the computer programming with Eurotherm monitors, the temperature is programmed and monitored with the help of Labview. At ICMCB, hydrothermal crystal growth is carried out in the machine designed by M/S HPSystems, Perigny France.

Figure 9 shows the vessel and the basket for nutrient with 2 seed crystals attached that is used before the experiments.

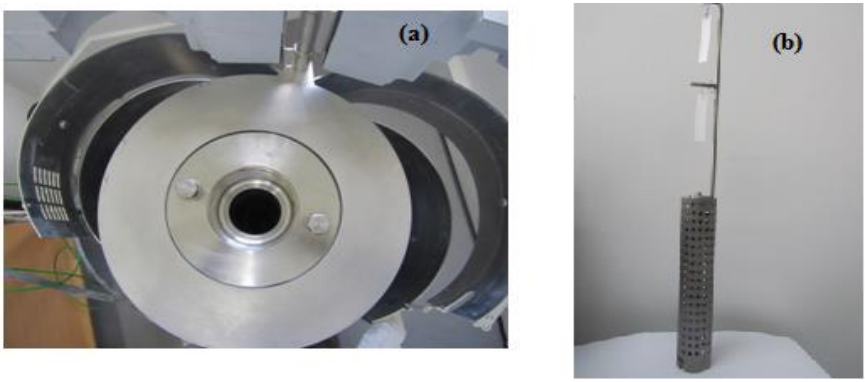

Figure 9. (a) Top view of vessel INCONEL and (b) Basket containing nutrient with seed α-quartz crystal attached.

Synthetic quartz oriented perpendicular to the Z-axis of the crystal is used as the seed (Figure 10 (b)). The surface of the seed is cleaned with HF at 70^{o}C. The seeds are suspended on the rod supported with the nutrient carrying basket. The amount of nutrient in the basket determines the size of the crystal to be grown. The quantity of the water to be filled and the pressure reached in the vessel can be determined by Kennedy's curve (Figure 10 (a)).

The preparation of the nutrient for germanium oxide with silicon oxide requires pre-preparation. Usually SiO_2 is available commercially in three forms, such as amorphous, solid and powder form. α-Quartz SiO_2 analogue of α- Quartz GeO_2 is available in the form of powder. Due to the variation of the solubility and solubility kinetics of GeO_2 and SiO_2, the resulting crystals may be non-stoichiometric. Further the transformation of the rutile form GeO_2 under hydrothermal conditions in pure water above 180^{o}C, results in very low solubility of GeO_2. In order to avoid the aforesaid problems, SiO_2 and GeO_2 are mixed in the desired ratio, and then thermally heated either to form amorphous phase or cristobalite form (Figure 11) in conventional furnace.

SGO nutrient is taken in the basket. A baffle separates the two zones in order to facilitate the growth of crystals with uniform dimensions in the crystallizing zone. The pressure inside the vessel can be varied with the content of solvent and nutrient that also regulates the temperature difference between the crystal growth and dissolution zone. When the temperature is high enough to initiate crystal growth, the nutrient dissolves and saturates the

solution. The vessel is cold in the top which results in supersaturation of the solution. The deposition from the supersaturated solution causes the growth of crystal on the seed. The nutrient required for continuous growth is obtained by convection currents caused by the temperature gradient. The baffle regulates the transport of the growth species from the saturated solution (warm zone) to the growth zone (cool zone). This process is continuous and leads to the growth of large crystals. The starting materials will be dissolved directly in the growth vessel; hence the nutrient is taken in the basket, which will be introduced in the vessel. The basket facilitates to hold the nutrient and at the same time it avoids the easy management of charge to be removed after the experiment. A small perforation in the basket allows also the thermocouple to pass through until the bottom of vessel. The temperature and the pressure in the vessel are recorded with the help of thermocouple and pressure sensor. The temperature ranges from 300^{o}C to 500^{o}C and the pressure ranges from 100 MPa to 300 MPa to grow the quartz single crystals with a temperature gradient between 5^{o}C to 100^{o}C. Quartz crystals are grown on the seeds of oriented α-quartz single crystals SiO_2, which are prepared by cleaning the surface of the seeds with HF/ NaOH.

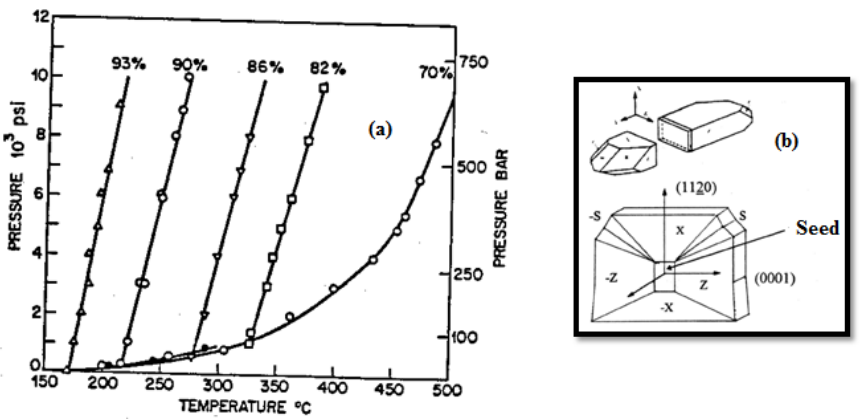

Figure 10. (a) Kennedy's curve and (b) Z-oriented seed of Quartz crystal.

Hydrothermal crystal growth in the vessel is dependent on the supersaturation conditions in the cool zone and crystal growth rate, which in turn is dependent on the kinetics between the starting compounds i.e., SiO_2 and GeO_2. The starting nutrient compounds based on SiO_2 and GeO_2 varies primarily into two principal groups such as crystalline phase with cristobalite

type structure with composition $Si_{1-x}Ge_xO_2$ (x=0.20) Crystal growth experiments of SGO, when done with NaOH, the growth rate of quartz increases. However the concentration of NaOH <0.2M, when the quantity of NaOH increases the growth decreases. Formation of $Na_4Ge_9O_{20}$ phases in the residual nutrient is observed at the end of the crystal growth, which will decrease the quantity of Ge in the crystal grown. When pure water is used as the solvent, the thermodynamical conditions should be varied in order to forcibly dissolve the nutrients. In the aforesaid case, high temperatures T> 400^{o}C and P > 200 MPa is required. In this case, the content of Ge is high, but the distribution is less homogeneous. In some cases, homogeneous distribution of Germanium is reported when the temperature is less than 415^{o}C. The high solubility of Ge in water is one of the prime reasons for which the composition of the grown crystal can be not similar as that of the nutrient. Further with the increase of Ge content, there are cracks observed inside the seed used in pure SiO_2 due to the high stress by the structural difference between the SGO crystal and SiO_2 seed interface. The transport of species can be judged by the temperature gradient in the vessel. A small gradient allows the transport of species in a very controlled manner and it increases the crystalline quality, but it decreases the growth rate. On the other hand, the increase of Ge content in $Si_{1-x}Ge_xO_2$ increases the germanium species in the pure water as solvent.

Figure 11. Nutrient preparation in SiO_2 sintered crucible for SiO_2-GeO_2 solid solutions.

High pressure crystal growth experiments to obtain SGO crystals were carried out in the vessel designed and developed by M/S HPSystems, France, which is capable of working until 3500 bar, 450^{o}C with vessel capacity

of 1.5 l. Figures 12 and 13 shows the various components of the hydrothermal equipment used at ICMCB for growth of SGO crystals.

Bulk crystals of SGO (t=4 mm) were obtained after a period of 2 months. Electron probe microscope analysis has confirmed the presence of Ge in the lattice of SGO, which is shown in Figure 14.

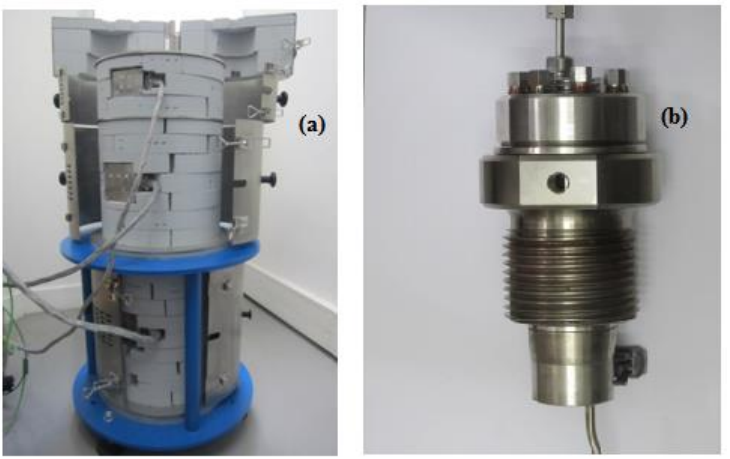

Figure 12. (a) The three zones furnace with adjustable refractory element and (b) Gasket and 8 screw (obturator).

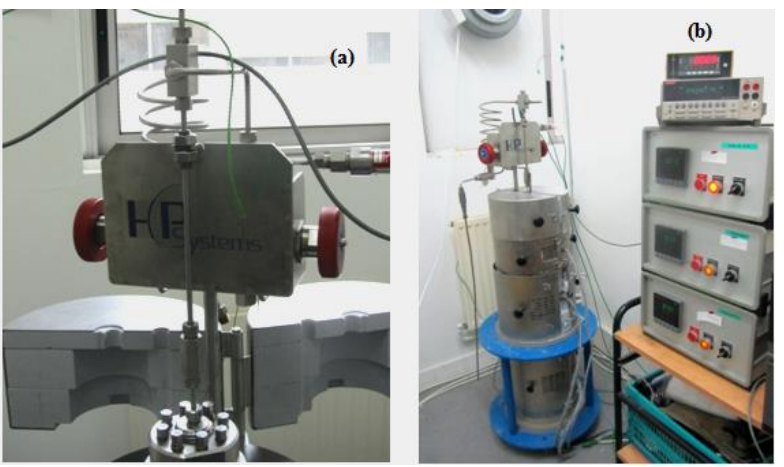

Figure 13. (a) Top view of high pressure system (top heat protecting system open) and High pressure security valve/regulation part and (b) Complete view of hydrothermal system interfaced with computer.

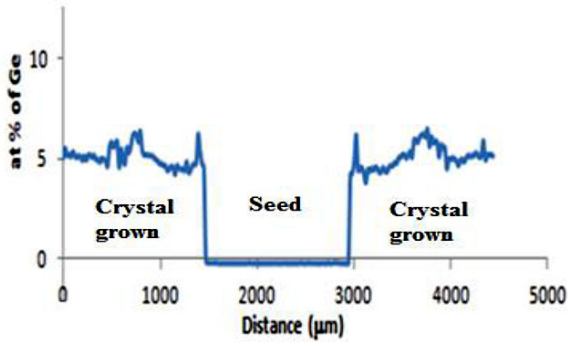

Figure 14. EPMA of the grown SGO single crystals by hydrothermal method.

CONCLUSION

Quartz crystals are currently well known for their remarkable properties such as piezoelectricity. By substituting "Si" ions with "Ge" is a way to increase the piezoelectricity. In order to construct the devices, large defect free single crystals are needed. Due to the phase transitions, hydrothermal crystal growth technique is one of the best methods to obtain large size crystals with Z parallel faces for piezoelectric properties. In order to grow the SiO_2 doped with GeO_2, it is necessary to prepare the cristobalite nutrient to obtain homogeneous composition. Further high pressure helps in conjunction with other parameters such as temperature gradient helps in obtaining SiO_2 doped with Ge. Various aspects of hydrothermal crystal growth have been discussed in terms of solvents and instrumentation in detail.

REFERENCES

[1] Shujun Zhang, YitingFei, Bruce, H. T. Chai, Eric Frantz. & David W. (2008). Snyder, XiaoningJiang, and Thomas R. Shrout, *Appl. Phys. Ltrs*. *92*, 202905.

[2] Mark, J.& Schulz, Mannur, J. (2003). Sundaresan, Jason McMichael, David Clayton, Robert Sadlerand Bill Nagel, *Journal of Intelligent Material systems and structures*,*14*, 693.

[3] Largeteau, A., Darraq, S., Goglio,G. &Demazeau, G. (2008). *High Pressure Research*, *28*(4),503.

[4] Ranieri, V., Darracq, S., Cambon, M., Haines, J., Cambon, O., Largeteau, A. &Demazeau, G. (2011). *Inorg. Chem.*,*50*, 4632.
[5] Giorgio Spezia, (1905). *Proceedings of the Royal Academy of Sciences in Turin*, *40*,254.
[6] Robert, A. (1987). *Laudise, Chemical And Engineering News*, *65*(39) 30.
[7] Brice, J. C. (1985). *Reviews of Modem Physics*, *57* (1), 105.
[8] Gary Johnson and Jonathan Foise, (1996). *Encyclopedia of Applied Physics*., *15*, 365.
[9] Byrappa,K. Masahiro Yoshimura, (2001). *Handbook of Hydrothermal TechnologyNorwich*, New York: Noyes Publications.
[10] Lignie, A., Menaert, B., Armand, P., Pena, A., Debray, J. &Papet, P.(2013). *Cryst. Growth Des*., 13, 4220.
[11] Yu, V., Pisarevsky, O., Yu. Silvestrova, E., Phillippot, D.V., Balitsky, D.&Yu., Pisharovsky, V.S. (2000). Balitsky, IEEE/EIA *International Frequency Control Symposium and Exhibition*, 177.
[12] Grimm, H., Dorner, B.(1975). *J. Phys. Chem. Solids*, *36*, 407.
[13] Miller, W. S., Dachille, F.&Shafer, E. C. (1963). R. Roy, *Am. Mineral*.*48*,1024.
[14] Philippot, E, Palmier, D. Pintard, M. Goiffon, A. (1996) *Journal of Solid State Chemistry*, *123*, 1.

In: Crystals and Crystal Growth
Editor: Wilfred Carter
ISBN: 978-1-63463-791-6
© 2015 Nova Science Publishers, Inc.

Chapter 2

IN-SITU INVESTIGATION OF THE MELT STRUCTURES IN BORATE CRYSTAL GROWTH SYSTEMS

Songming Wan
Anhui Key Laboratory for Photonic Devices and Materials,
Anhui Institute of Optics and Fine Mechanics,
Chinese Academy of Sciences, Hefei, P. R. China

ABSTRACT

Borate crystals are widely used as nonlinear optical, laser and luminescent materials due to their diversified structures, and good chemical and physical properties. The growth of high-quality borate crystals is required for their applications. A fundamental problem for borate crystal growth is the high-temperature melt structures in the crystal growth systems. They are related not only to the macro-properties of the melts, but also to the micro-processes of the crystal growth. However, the borate melt structures have been poorly understood because of the structural complexity, and the lack of effective experimental techniques and theoretical analysis methods. High-temperature Raman spectroscopy is a powerful tool for the study of borate melt structures, and has been applied to *in-situ* investigate the melt structures in the $Ba_2Mg(B_3O_6)_2$, BaB_2O_4, CsB_3O_5, LiB_3O_5, BiB_3O_6, and $Li_2B_4O_7$ crystal growth systems. Alkali-earth cations and $[B_3O_6]^{3-}$ rings, as the structural units, have been found in the $Ba_2Mg(B_3O_6)_2$ and BaB_2O_4 melts. A boundary layer in

which the melt structure gradually changes to the crystal structure has been observed around the LiB_3O_5 or β-BaB_2O_4 (low-temperature phase BaB_2O_4) crystal−solution interface. An isomerization reaction between $[B_3O_3Ø_4]^-$ (Ø = bridging oxygen atom) rings and $[B_3O_4Ø_2]^-$ rings has been found in the CsB_3O_5 or LiB_3O_5 boundary layer, and applied to understand the two crystal growth mechanisms and habits. On the basis of the structural evolution around the growing BiB_3O_6 and $Li_2B_4O_7$ crystals, two polymer-like structural models have been proposed to describe the BiB_3O_6 and $Li_2B_4O_7$ melt structures. The density functional theory (DFT) calculation, as an effective theoretical method, verified the melt structural models, and gave clear assignments of all important vibrational peaks in the melt Raman spectra.

1. INTRODUCTION

Anhydrous borate crystals are characterized by their structural diversity since boron combines with oxygen not only in three-fold (triangular) but also in four-fold (tetrahedral) coordination, the triangular and/or tetrahedral boron−oxygen moieties can further polymerize by sharing common oxygen atoms to form larger borate clusters, such as chains, sheets, and three-dimensional networks [1]. Up to now, more than 1,100 anhydrous borate crystals have been found and structural determined [2], quite a few of them are used as nonlinear optical (NLO) [3] and birefringent devices [4–6], laser hosts [7–9], surface and bulk acoustic wave devices [10], and neutron detecting materials [11].

Enormous efforts have been made in the past three decades to grow borate crystals [12]. However, the problem of reproducible growth of large and high-quality borate crystals is far from being solved. The primary difficulties include: (1) The high viscosity of borate melts possibly due to their tendency to form various complicated structures, which limits mass transport and then leads to inclusions and voids heavily concentrated in the crystal boules. (2) The incongruent melting character of some borate crystals. Their growth generally relies on a very time-consuming *trial-and-error* method to determine suitable fluxes. The above-mentioned difficulties incent us to study the basic problems related to the growth of borate crystals in order to find the optimized methods to solve these difficulties.

As we know, almost all borate crystals are grown from high-temperature melts (or solutions) with the transformation from the melt (or solution) structures to the crystal structures. The knowledge of the melt (or solution)

structures is of highest priority for the investigation of the borate crystal growth mechanism which is related to a variety of crystal growth phenomena and the formation of various crystal defects. Moreover, the melt structure is the intrinsic factor to govern the melt macro-properties, such as viscosity, density, and surface tension, which often determine the crystal growth conditions. However, an accurate structural description of a borate melt is very difficult not only due to the lack of experimental techniques but also the limitation of theoretical methods.

2. HIGH-TEMPERATURE RAMAN SPECTROSCOPY

As compared with borate crystal structures that can be determined by X-ray or neutron diffractive method, the borate melt structures have not been solved very well. In order to avoid experimental difficulties associated with high-temperature conditions, investigators predominantly used borate glasses as the proxies for the borate melts based on the conjecture that a glass structure is closely analogous to the melt structure from which it was quenched [13]. However, this method is still debatable because a glass structure only represents the super-cooled melt structure that has undergone a cooling and a glass transition process before the melt transforms to the glass. Both of the processes will influence the glass structure [14]; therefore, an accurate description of a melt structure requires *in-situ* experimental techniques.

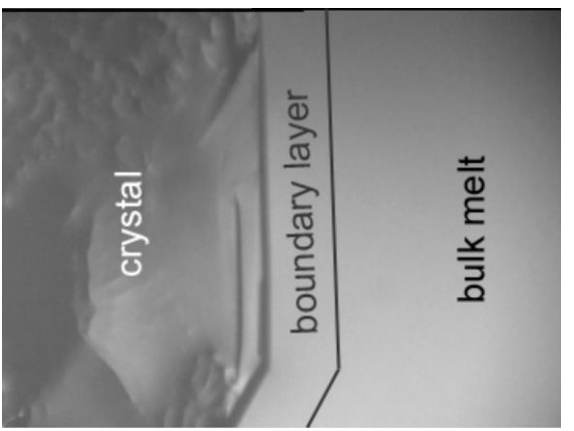

Figure 1. Crystal, boundary layer and bulk melt in a high-temperature crystal growth system.

Moreover, the investigation of the melt structures in borate crystal growth systems demands the experimental technique being capable of micro-scale analysis. As we know, a crystal growth process takes place near a crystal−melt interface. The melt structure adjacent to the interface is under the influence of the well-ordered atomic potential of the interface. As a result, a transition region of melt structure should exist near the interface [15–17]; we call it boundary layer (see Figure 1). Such a boundary layer has been supported by an increasing number of experimental results. The melt structure in the boundary layer is essential to understand the crystal growth mechanism and other interfacial transport phenomena, and the key to deduce the bulk melt structure. Generally, the boundary layer is less than 1mm in thickness, which further requires the *in-situ* experimental techniques having the ability of micro-scale analysis to investigate the melt structure in the boundary layer.

Compared with other popular high-temperature *in-situ* experimental techniques, including high-temperature X-ray diffraction [18], neutron diffraction [19], X-ray photoelectron diffraction [20], nuclear magnetic resonance [21], and high resolution transmission electron microscopy [22], high-temperature Raman spectroscopy combines the advantages of high-temperature, *in-situ*, and micro-scale analysis. Besides, high-temperature Raman spectroscopy is more convenient than high resolution transmission electron microscopy, more sensitive to hyperfine structures than X-ray diffraction, neutron diffraction, and nuclear magnetic resonance techniques [23], and thus very suitable for the melt structure study, especially for which of the boundary layer.

Raman spectroscopy is based on the Raman scattering phenomenon that was first observed experimentally in 1928 by C. V. Raman, an Indian physicist who received the Nobel Prize in 1930 [24]. He found that, when light traverses a transparent material, some of the deflected (scattered) light changes in wavelength. The Raman spectrum is represented by the intensity of the scattered light as a function of the frequency shift between the incident and scattered light. The spectrum contains the vibrational information of a molecule (or crystal lattice) and constitutes a fingerprint by which the molecular (or crystal lattice) structure can be identified. However, Raman scattering is inherently a weak process, the high sensitivity of Raman spectroscopy must rely on sufficiently intense radiation sources. The introduction of laser radiation sources has revolutionized this spectroscopic technique [25]. Today, Raman spectroscopy is a well-established tool for molecular (or crystal lattice) structure analysis. However, most of Raman spectroscopic studies are limited to room temperature because the high-

temperature Raman spectroscopy suffers from the intense black-body radiation from samples and furnaces that often covers the useful Raman signals.

In order to eliminate the influence of the black-body radiation, various high temperature Raman spectroscopic techniques have been developed, including: (1) spatial resolution technique [26]. By using a confocal micro-Raman method, most stray light out of the optical focus is rejected. (2) accumulated time resolution technique [27]. By using pulsed laser sources, the time required to record a Raman spectrum is markedly reduced, which significantly decreases the photon counting of stray light. Meanwhile, the high power of the pulsed lasers can greatly enhance the signal-to-noise ratio. More recently, an Intensified Charge Coupled Device (ICCD) detector was applied in a high-temperature Raman spectrometry by You et al. as a new time resolution technique [28]. The ICCD detector is precisely synchronized with the laser pulse, and then the stray light outside the pulse duration is eliminated. (3) ultraviolet laser technique. The short wavelength laser can enhance the Raman scattering intensity, and eliminate the influence of fluorescence [29].

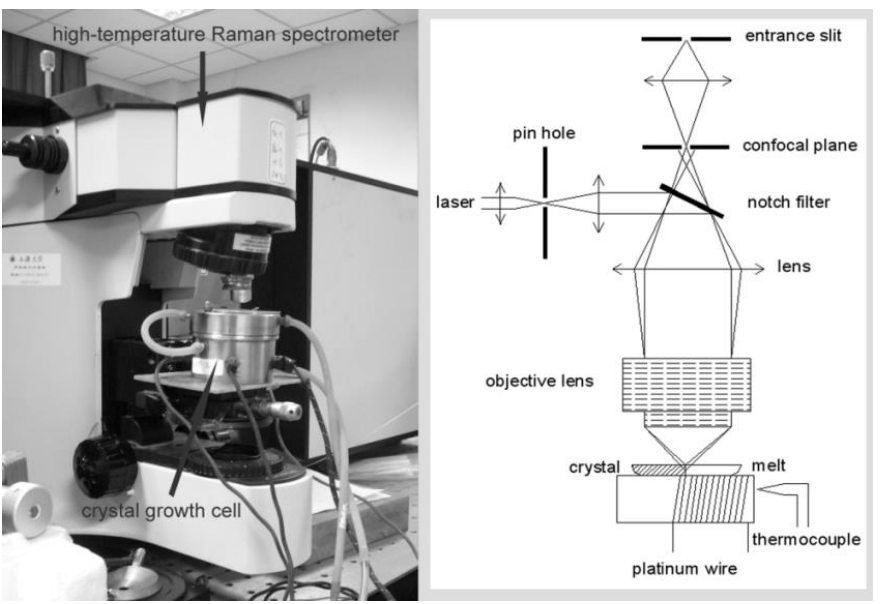

Figure 2. A typical experimental system for the study of high-temperature melt structures.

A typical experimental system for the study of borate melt structures comprises two components (see Figure 2) [30]: a Raman spectrometer and a crystal growth cell. Raman spectra are recorded on the high-temperature Raman spectrometer (Jobin Y'von LABRAM HR800 in our experiments) with a back scattering configuration. The excitation source is the 532 nm line of a Q-switch pulsed SHG-Nd: YAG laser. The laser beam is introduced into a sample, and the Raman scattering light is collected by a confocal lens system. The growth cell is fabricated from high-grade stainless steel and consists of a water jacket surrounding the main sample chamber. A platinum boat with the size of $5 \times 10 \times 20$ mm^3 is placed in the center of the chamber and heated on the right side by a platinum wire winding. The heating system provides a horizontal temperature gradient in the boat. The measuring temperature of the experimental system is up to 1200 ^oC, and the spatial resolution is less than 2 μm.

3. THE DENSITY FUNCTIONAL THEORY METHOD

Although high-temperature Raman spectroscopy is the best experimental technique to study borate melt structures, the conversion of the vibrational peaks seen in a Raman spectrum into the structural information remains difficult. The main difficulties arise from: (1) the great structural diversity of borate melts. The triangular and/or tetrahedral boron–oxygen moieties often polymerize to various poly-anions by sharing oxygen atoms. (2) the complexity of borate Raman spectra. Even worse, different poly-anions probably give rise to Raman peaks in the same region. (3) the weakness of high-temperature Raman peaks. Furthermore, a Raman peak sharp at low-temperatures often broadens at high-temperatures, and overlaps with adjacent peaks. (4) The powerful tool is still scarce for the theoretical analysis on borate Raman spectra.

Traditionally, Raman peaks of a borate melt are structurally assigned by comparison with the spectra of borate crystalline compounds based on the assumption that the structural units present in melts resemble those present in the crystalline compounds [23, 31]. However, such an approach will be invalid if a melt structure is different from any crystalline compound structure. *ab* initio calculation is regarded as the alternative to the traditional approach, and has been used to investigate the borate melt structures that are difficult to obtain by conventional experimental methods alone. If the calculated method is reliable, and the calculated Raman spectrum of a guessed melt structural

model is consistent with the experimental Raman spectrum, one can conclude that the guessed model can be used to describe the melt structure.

The Hartree–Fock method, usually performed using the Gaussian program, is the old method widely used to calculate the equilibrium structures, Raman frequencies, and Raman peak intensity of borate glasses [32]. From the beginning of this century, the method has been extended to study borate melt structures by You et al. [33]. A larger amount of valuable information about borate melt structures has been obtained. However, the method has several drawbacks leading to relatively poor prediction of melt structures, for example: (1) The method is suitable for isolated small clusters, but not for the larger borate clusters that are very likely to exist in borate melts. (2) The solvent effect (the interactions of the clusters with the surrounding), which severely influences the calculated results, is hard to be formulated in the Hartree–Fock method. (3) The method often results in systematic errors of calculated Raman frequencies due to the lack of good modeling of the electronic orbitals.

Breakthrough studies on borate melt structures and Raman spectra benefit from the development of the density functional theory (DFT) which was established by Hohenberg, Kohn, and Sham nearly 50 years ago [34]. The density functional perturbation theory (DFPT), made by Baroni, Gonze and their co-workers, extends the scope of the DFT Hamiltonian [35–37]. In the framework of DFPT, Raman spectra can be accurately calculated by coupling a standard DFT method with a linear response phonon model.

The Cambridge Sequential Total Energy Package (CASTEP) [38], originally developed in the Theory Condensed Matter Group at Cambridge University, is regarded as the most validated commercial software to predict material structures and their Raman spectra. The package uses a total energy plane-wave pseudo-potential method. In the mathematical model used in the method, the pseudo-potentials are used to describe the electron–ion interactions, the electronic wavefunctions are expanded through a plane-wave basis set, and the exchange and correlation effects are included within either the local density (LDA) or the generalized gradient (GGA) approximation. In CASTEP, Raman frequencies are computed by diagonalization of dynamical matrices, and the Raman activity tensor/intensity of each mode is given by the derivative of the dielectric permittivity tensor with respect to the mode amplitude. CASTEP currently provides two different methods (the DFPT method and the "finite displacement" method) for calculating Raman frequencies, and uses a hybrid method combining DFPT with the "finite displacement" method for calculating Raman activity tensors/intensities. In

addition, the CASTEP calculation can provide the atomic displacements of each peak/mode in a Raman spectrum.

The DFT method has been applied recently to a larger number of crystalline materials. Good agreement with experimental results was achieved [39]. Considering that CASTEP has been used to study liquids and melts are special liquids existing under high-temperature conditions, we attempted to apply CASTEP to simulate the Raman spectra of borate melts, and found that the results obtained by CASTEP are much better than those obtained by other traditional methods. I am sure that the CASTEP method combining with high-temperature spectroscopy will open a new way to explore the structures of borate and other inorganic melts. The following are the last applications of high-temperature spectroscopy and the DFT method in the borate melt structure studies.

4. MELT STRUCTURES IN SOME BORATE CRYSTAL GROWTH SYSTEMS

(1) Melt Structures in the $Ba_2Mg(B_3O_6)_2$ and BaB_2O_4 Crystal Growth Systems

The $Ba_2Mg(B_3O_6)_2$ (BMBO) and high-temperature phase BaB_2O_4 (α-BBO) crystals are excellent uniaxial crystals with large birefringences, a wide transparence range and good physicochemical stability. Both of them can be employed to produce various prisms, polarizers, beam displacements, and beam splitters, especially those used in the deep ultraviolet region [4–6]. The low-temperature phase BaB_2O_4 (β-BBO) is an excellent NLO crystal widely used in laser and optoelectronic devices [3]. The three crystals are all made up of alkaline earth ions and $[B_3O_6]^{3-}$ planar six-membered rings.

The BMBO and BaB_2O_4 crystals melt congruently, but the BaB_2O_4 crystal undergoes a phase transition at about 925^{o}C. Wang et al. demonstrated that the α-BBO crystals doped with a small amount Sr^{2+} are stable at room temperature; therefore, the Sr^{2+}-doped α-BBO crystal, along with the BMBO crystal, can be grown by the Czochralski or Kyropoulos method [40]. Unlike the two crystals, β-BBO crystals are commonly grown from the Na_2O/NaF flux due to the phase transition [12]. Very little research has been carried out on the melt structures in the three crystal growth systems although the structures are believed to be essential to understand various growth phenomena. For the β-

BBO crystal growth system, Kouta et al. proposed that a melt with a pre-ordering structure formed near the growth interface during the crystal growth process, and further presumed that planar $[B_3O_6]^{3-}$ rings were the growth units [41]; but molecular dynamic (MD) studies showed that the $[B_3O_6]^{3-}$ rings in the crystal structure quickly disappeared in the melt just after the crystal melted and formed long chain structures [42]. The focus of their disputes is whether the $[B_3O_6]^{3-}$ rings exist near the growth interface.

First of all, we need to identify the characteristic Raman peaks of the $[B_3O_6]^{3-}$ ring. Although the Raman spectrum of the β-BBO crystal has been investigated extensively, the mode assignments of the $[B_3O_6]^{3-}$ ring are still in debate. Using the BMBO crystal as an example, we re-investigated the characteristic Raman peaks of the $[B_3O_6]^{3-}$ ring, and gave more accurate assignments for its vibrational modes [43]. The site group analysis results

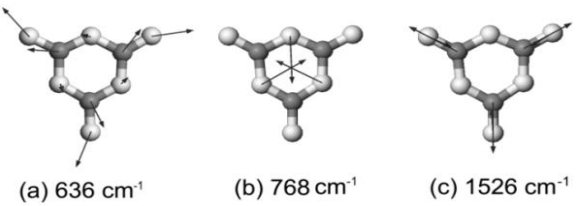

Figure 3. Atomic displacements of three symmetrical vibrations of $[B_3O_6]^{3-}$ six-membered rings.

Table 1. Site group analysis for the BMBO lattice modes

Ion	Number of free ion vibration			Free ion symmetry	Site symmetry	Unit cell symmetry
	N_{tr}	N_{ro}	N_{in}	D_{3h}	C_3	S_6
B_3O_6			3	A_1'		
		1	2	A_2'	A	A_g
	1		5	E'		
				A_1''	E	E_g
	1		2	A_2''		
		1	2	E''		A_u
Ba^{2+}	1				A	
	1				E	E_u
Mg^{2+}	1				A_u	
	1				E_u	

(Table 1) show that the total lattice modes of the BMBO crystal are $10A_g$ + $11A_u$ + $10E_g$ + $11E_u$, among them, $10A_g$ + $10E_g$ are Raman active. All of the Raman active modes have been identified on the basis of the CASTEP calculated results. The Raman peaks arising from the internal modes of the $[B_3O_6]^{3-}$ ring are above 220 cm^{-1}, and the external below 220 cm^{-1}. Two strong Raman peaks located at 636 cm^{-1} and 768 cm^{-1} (calculated values) and four Raman peaks in the range of 1510−1570 cm^{-1} are the characteristic Raman peaks of the $[B_3O_6]^{3-}$ ring. All of them belong to the A_g mode. The peak at 636 cm^{-1} is assigned to the breathing mode of the boron and extra-ring oxygen atoms, 736 cm^{-1} the breathing mode of the intra-ring oxygen atoms, and 1510−1570 cm^{-1} the breathing mode of the boron atoms, as shown in Figure 3.

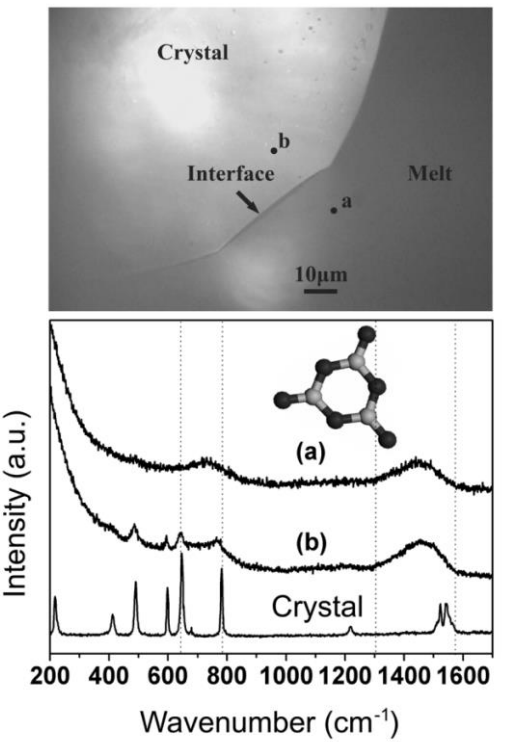

Figure 4. Measurement positions (top) and their corresponding Raman spectra (bottom). Position a is in the melt and 10 μm from the interface; positions b is in the crystal and 10 μm from the interface. The inset is the structure of the $[B_3O_6]^{3-}$ ring.

A BMBO single crystal grown by the Kyropoulos method was cut into slices slightly smaller than the platinum boat (see Figure 2). One such slice was then mounted in the boat with its right part heated to the temperature just above its melting point (1095 ^{o}C). After that, the temperature was slowly decreased to allow the crystal to grow gradually to the right, and then a stable crystal−melt interface was produced. Finally, the laser beam was focused on different positions near the crystal−melt interface to study the structures of the crystal and the melt. The melt structures near the α-BBO crystal–melt interface were studied in the same manner.

Two wide bands in the range of 600–850 cm^{-1} and 1300–1600 cm^{-1} appear in the BMBO melt Raman spectrum, as shown in Figure 4. Both of them can be attributed to the merger of the characteristic Raman peaks of the $[B_3O_6]^{3-}$ rings; we thus conclude that the $[B_3O_6]^{3-}$ rings are the dominant boron–oxygen structural units in the melt near the BMBO crystal–melt interface [44]. Similarly, the $[B_3O_6]^{3-}$ rings were found as the main structural units in the melt near the α-BBO crystal–melt interface [45]. It is noteworthy that the 600–850 cm^{-1} bands of the two melts peak at the different positions. As mentioned above, the bands arise from the merger of two A_g modes whose Raman peaks are centered at around 640 and 770 cm^{-1}. The intensity of the

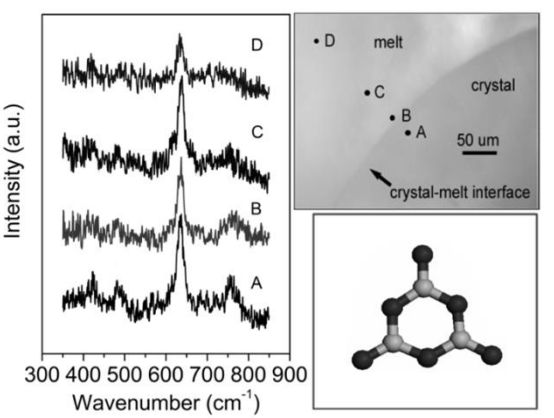

Figure 5. A typical α-BBO crystal–melt interface with the measurement positions (upper right) and their corresponding Raman spectra (left). Position A is in the crystal and 25 μm from the interface; positions B, C and D are in the melt, and 5 μm, 55 μm and 155 μm from the interface, respectively. The bottom right illustration is the structure of the $[B_3O_6]^{3-}$ ring.

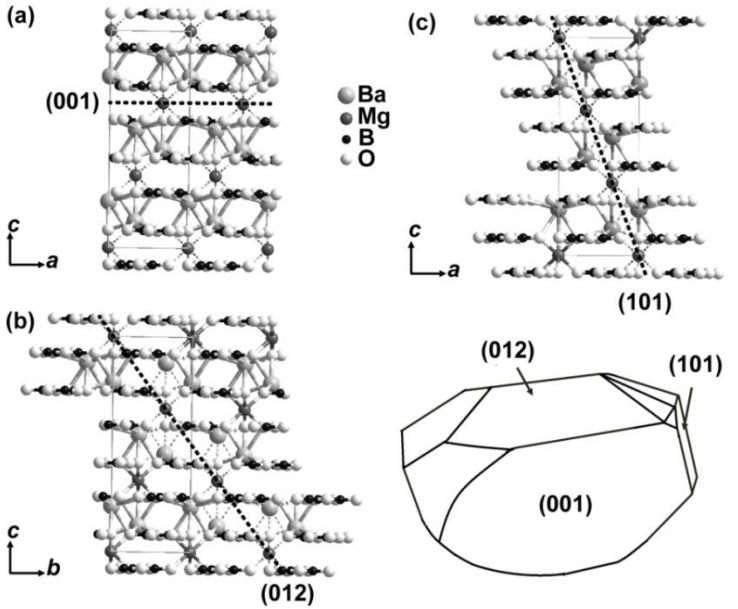

Figure 6. Packing arrangement of BMBO crystal structure as viewed along (a) the *b* axis, (b) the *a* axis, and (c) the *b* axis, and BMBO crystal morphology (bottom right).

640 cm^{-1} peak is much stronger than that of the 770 cm^{-1} peak in the α-BBO melt Raman spectrum (see Figure 5), but comparable in the BMBO melt Raman spectrum, which results in the merged band peaking at lower frequency in the α-BBO melt Raman spectrum as compared with that in the BMBO melt Raman spectrum.

On the basis of the experimental results, the BMBO crystal morphology (growth habit) was explained by the attachment energy theory [44]. In principle, the morphology of a crystal is determined by the relative growth rates of different crystal faces. The face that grows slower appears to be the larger developed face. Based on the Hartman–Perdok theory, the growth rate of a crystal face is proportional to its attachment energy (E_{att}, defined as the energy released when one additional growth slice of thickness d_{hkl} is attached to the crystal face identified by the Miller indices *hkl*). During the melting process of the BMBO crystal, the crystal structure breaks into Ba^{2+} ions, Mg^{2+} ions and $[B_3O_6]^{3-}$ rings, indicating both of the Ba–O and Mg–O bonds are the weak bonds in the crystal structure. The (001) (101) and (012) crystal faces that are linked by the weak bonds have smaller attachment energies and slower growth rates, and thus present in the final morphology (see Figure 6). The

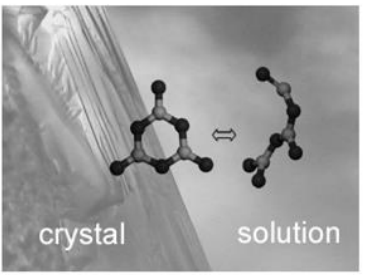

Figure 7. An isomerization reaction taking place near the β-BBO crystal–solution interface.

α-BBO crystal morphology was explained by the periodic bond chain (PBC) theory [45]. At the α-BBO crystal–melt interface, the $[B_3O_6]^{3-}$ rings and Ba^{2+} cations stack mainly along four types of PBCs. The four PBCs constitute three F faces, *i.e.* $\{10\bar{1}2\}$, $\{01\bar{1}4\}$, and $\{10\bar{1}10\}$ faces, which present in the final crystal morphology. The predicted results both of the BMBO and α-BBO crystals are in good agreement with the observed.

Na_2O, as a flux, is widely used to produce large-sized and high-quality β-BBO crystals [12]. In order to simulate the β-BBO crystal growth, a small slice of the β-BBO single crystal was placed on the cool side of the platinum boat; the raw material (70 mol% BaB_2O_4−30 mol% Na_2O) was placed on the hot side. The platinum boat was heated slowly until the raw material melted completely and the crystal began to melt. By slowly decreasing the temperature, a new β-BBO crystal grew gradually from the old crystal surface; finally, a stable crystal–solution interface was established. After that, the high-temperature Raman spectra were recorded from different positions near the crystal–solution interface [46].

The experimental results show that a wide band in the range of 950−1250 cm^{-1} presents in the Raman spectrum of the bulk solution, but disappears in the Raman spectra of the solution near the interface. The spectral difference clearly indicates a boundary layer existing near the β-BBO crystal–solution interface. The thickness of the boundary layer is less than 85 μm. The CASTEP calculations further proved that the wide band in the range of 950−1250 cm^{-1} is associated with a special chain-type $[B_3O_6]^{3-}$ group. The chain-type $[B_3O_6]^{3-}$ groups transforms to the ring-type $[B_3O_6]^{3-}$ groups in the boundary layer (see Figure 7). The $[B_3O_6]^{3-}$ rings play a role of the basic units of the β-BBO crystal growth. According to the results, the β-BBO crystal growth habit (morphology) can be explained very well.

(2) Melt Structures in the CsB_3O_5 and LiB_3O_5 Crystal Growth Systems

Both CsB_3O_5 (CBO) and LiB_3O_5 (LBO) are excellent NLO crystals due to their relatively large effective NLO coefficients, a high laser damage threshold, and a wide optical transparency range. The LBO crystal allows temperature-controllable non-critical phase matching (NCPM) in a wide wavelength range, and is a material of choice for high power lasers [47]. Compared with the LBO crystal, the CBO crystal is more efficient for the generation of the third harmonic of the 1064 nm radiation of Nd: YAG lasers [48]. Both of the crystals are built up of $[B_3O_3Ø_4]^-$ six-membered rings (see the bottom right illustration in Figure 8, Ø = bridging oxygen atom) and alkali metal ions.

CBO melts congruently but LBO melts incongruently. Thus, CBO crystals can be grown by the Kyropoulos method, but LBO crystals must be grown by the flux method [12]. The B_2O_3 flux was firstly reported in 1989 by Chen et al. [49], and was widely used to industrially produce LBO crystals in the following decade. Significant progress in the growth of larger LBO crystals has been achieved since 1996 with the development of MoO_3-based fluxes [50]. Using the fluxes, high-quality LBO crystals with the weight up to 2.0 kg have been produced [51–53].

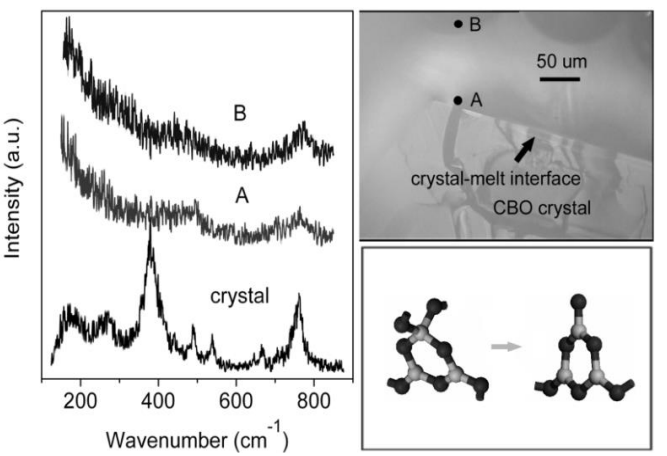

Figure 8. A typical CBO crystal–melt interface with the measurement positions (upper right), and their corresponding Raman spectra (left). The bottom right illustration is the isomerization reaction taking place near the CBO crystal–melt interface. Position A and B are in the melt, and 5 μm and 100 μm from the interface, respectively.

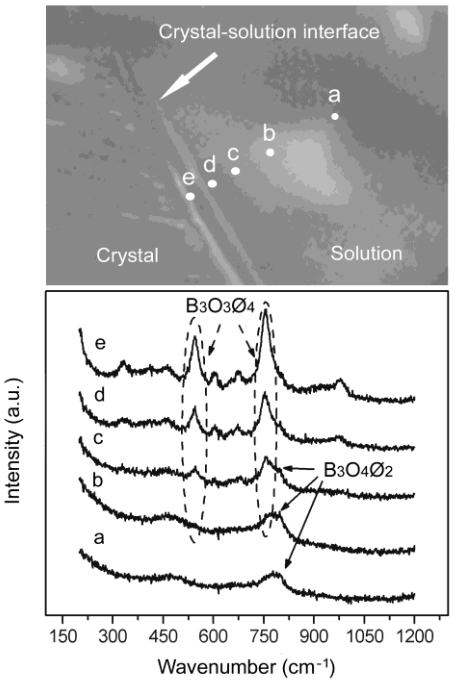

Figure 9. A typical LBO crystal–solution interface with the measurement positions (top) and their corresponding Raman spectra (bottom). The distances from the interface to the measurement position a, b, c and d are 100, 50, 20 and 5 μm, respectively.

In order to understand the structural origins of CBO crystal Raman peaks, the CBO crystal Raman spectrum was studied by CASTEP [54]. The CASTEP calculated results show the crystal characteristic peaks are located at around 760 cm^{-1} and 380 cm^{-1}, and related to the breathing vibration of the $[B_3O_3Ø_4]^-$ rings (760 cm^{-1}) and the bending vibration of the $BØ_4$ units in the $[B_3O_3Ø_4]^-$ rings (380 cm^{-1}).

A similar experimental process, as described in the above α-BBO experiment, was carried out for establishing a stable CBO crystal–melt interface. Figure 8 shows the Raman spectra recorded from different positions near the CBO crystal–melt interface [30]. When the measurement position moves from the crystal to the melt, the crystal 380 cm^{-1} peak vanishes, but the 760 cm^{-1} band remains. According to the CASTEP results of the CBO crystal, the spectral changes imply that an isomerization reaction between $[B_3O_3Ø_4]^-$ rings and $[B_3O_4Ø_2]^-$ rings takes place near the crystal–melt interface, as shown in Figure 8.

The isomerization reaction was also found during a CBO crystal melting process. On the basis of the isomerization reaction, the CBO melt structure near its melting point was deduced by You et al. [54]. When the crystal melts, the continuous three-dimensional crystal network collapses and transforms into spiral chains, its basic unit is a $[B_3O_4Ø_2]^-$ ring. On the basis of the $[B_3O_4Ø_2]^-$ chain model, the CBO melt Raman spectrum was simulated by using the Gaussian software [54]. The simulation was based on a traditional restricted Hartree–Fock method with the 6–31G(d) basis set. Considering the influence of the surrounding, the two bridging oxygen atoms in the $[B_3O_4Ø_2]^-$ ring are saturated by two hydrogen atoms. The calculated frequencies and intensities were corrected with a scaling factor (0.8970) and Bose–Einstein population factors, respectively. The calculated results provided the valuable vibrational information of the $[B_3O_4Ø_2]^-$ ring, and further interpreted the Raman spectral changes taking place in the crystal melting process.

In order to simulate the LBO crystal growth from the B_2O_3 flux, we established a crystal–solution coexisting system constituted by the LBO crystal and the $Li_2O{\cdot}4B_2O_3$ high-temperature solution. The solution structures near the crystal–solution interface were investigated by high-temperature Raman spectroscopy [55]. The results are shown in Figure 9, which reveals a boundary layer with the thickness of about 50 μm existing near the interface. Similarly to the structural changes observed near the CBO crystal–melt interface, the isomerization reaction between the $[B_3O_3Ø_4]^-$ and $[B_3O_4Ø_2]^-$ rings was also found in the LBO crystal boundary layer.

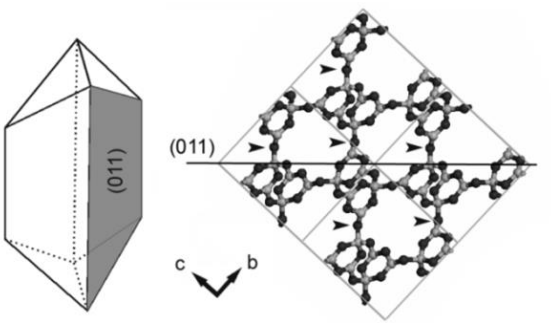

Figure 10. Morphology of CBO crystal grown from the CBO melt (left), and packing arrangement of CBO crystal as viewed along the *a* axis (right). The bridging oxygen atoms between two $[B_3O_3Ø_4]^-$ rings are pointed by the arrows.

The structural evolution taking place near the crystal–melt interfaces can be used to explain the growth habits of the CBO and LBO crystals [30, 55]. On the molecular level, the CBO or LBO crystal growth is accompanied by the conversion from the $[B_3O_4Ø_2]^-$ rings to the $[B_3O_3Ø_4]^-$ rings, which reveals that the B_4–Ø bonds (B–Ø bonds of $BØ_4$ tetrahedra) are weak bonds in the crystal structures. Therefore, the face only containing $BØ_4$ tetrahedra has a lower attachment energy and a lower growth rate, and should thus be a larger developed face. According to the CBO crystal structure, the faces only containing the B_4–Ø weak bonds are parallel to the (101), $(\bar{1}01)$, $(10\bar{1})$, (011), $(0\bar{1}1)$, and $(01\bar{1})$ faces (The case of the (011) face is shown in Figure 10.), and should thus be the larger developed faces. A similar analysis reveals that the LBO crystal tends to grow with the well-developed {011} and {201} faces, but not with the {001} faces. These predicted growth habits are all in good agreement with the experimental results.

(3) The Melt Structure in the BiB_3O_6 Crystal Growth System

The α-BiB_3O_6 (BIBO) crystal is an outstanding NLO material, possessing exceptionally large NLO coefficients, a wide transparency range, a high damage threshold and a large angular acceptance [56]. BIBO crystallizes in the monoclinic space group *C*2. Its crystal structure is made up of Bi^{3+} layers and boron–oxygen layers; the boron–oxygen layer is constituted by boron–oxygen triangles and tetrahedra in a ratio of 2:1 [57]. The crystal melts congruently at 708 ^oC, and thus can be grown by the Kyropoulos method [12].

High-temperature Raman spectroscopy and CASTEP have been used to study the melt structure in a BIBO crystal–melt coexisting system [58]. The experimental process is similar to that in the study of the BMBO melt structure. The BIBO melt Raman bands are located around 370 cm^{-1}, 630 cm^{-1}, and in the range of 1200–1500 cm^{-1}. As compared with the crystal Raman band, the melt Raman band in the range of 1200–1500 cm^{-1} increases in intensity. Meanwhile, the strong crystal peak located at 574 cm^{-1} disappears when the crystal melts. In order to interpret the structural origins of the spectral changes, some important crystal Raman peaks were assigned on the basis of the CASTEP calculated results. The crystal Raman peaks in the high frequency region (1200–1500 cm^{-1}) are associated with the stretching vibrations of the boron–oxygen bonds in the boron–oxygen triangles. The 574 cm – 1 (calculated)

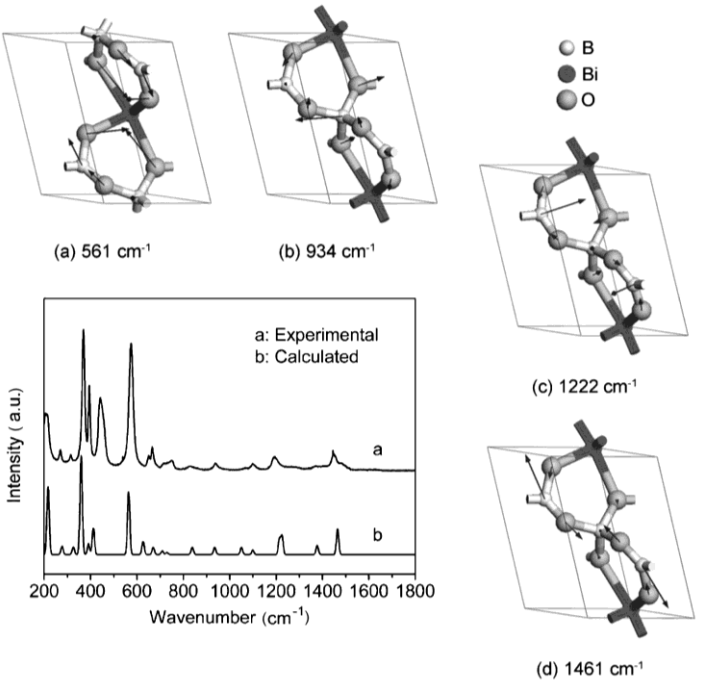

Figure 11. Experimental and calculated Raman spectra of BIBO crystal (bottom left), and the atomic displacements of the calculated peaks located at 561 cm^{-1}, 934 cm^{-1}, 1222 cm^{-1}, and 1461 cm^{-1}.

value: 561 cm^{-1}) crystal peak arises from the Bi–Ø symmetric stretching vibration of the $BiØ_4$ pyramids, as shown in Fig 11. The spectral changes reflect that the Bi–Ø bonds disappear due to the crystal melting, and the concentration of the boron–oxygen triangles in the BIBO melt is more than that in the BIBO crystal. The new boron–oxygen triangles come from the transformation from the four-fold coordinated boron atoms (in the crystal) to the three-fold coordinated boron atoms (in the melt).

On the basis of the BIBO crystal growth habit, a polymer model was proposed to describe the BIBO melt structure [58]. The melt is made up of Bi^{3+} ions and special $[B_3O_5Ø_2]^{3-}$ (Ø = bridging oxygen) structural units (see Figure 12 and 13) which further polymerize into $[B_3O_5Ø_2]_n$ chains by sharing oxygen atoms. The CASTEP calculations were carried out to simulate the BIBO melt Raman spectrum based on the structural unit [58]. The calculated melt Raman spectrum shows good agreement with the experimental (see

Figure 12). All of the vibrational bands in the melt Raman spectrum are assigned (see Figure 13).

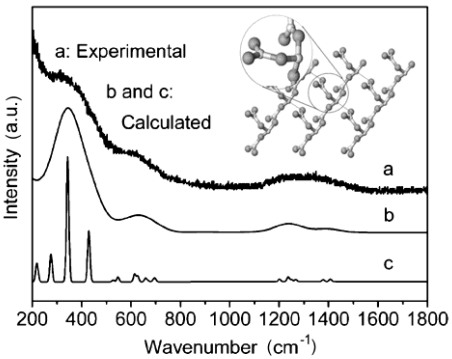

Figure 12. Experimental and calculated Raman spectra of BIBO melt. (a) Experimental Raman spectrum; (b) calculated Raman spectrum broadened by Gaussian line shape function with a FWHM (full width at half maximum) of 50 cm^{-1}; (c) calculated Raman spectrum broadened by Gaussian line shape function with a FWHM of 5 cm^{-1}. Inset: BIBO melt structure.

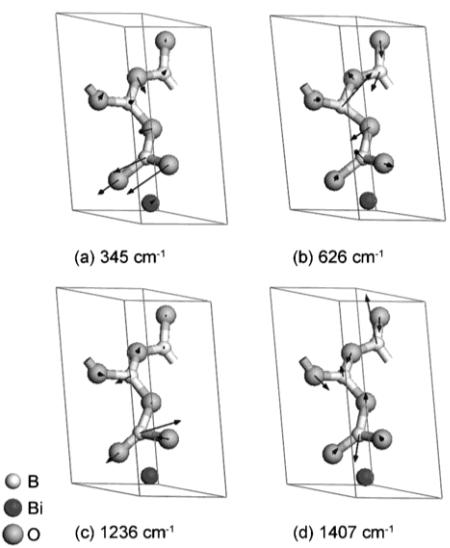

Figure 13. Atomic displacements of four main peaks in the calculated BIBO melt Raman spectrum.

The strongest band below 400 cm^{-1} is mainly attributed to the wagging vibration of the side $BO_2Ø$ triangle as a whole; the band located around 630 cm^{-1} is assigned to the bending vibrations of the $[B_3O_5Ø_2]_n$ chain; the bands in the range of 1200–1500 cm^{-1} arise from the stretching vibrations of the boron–oxygen (B–Ø or B–Ø) bonds in the boron–oxygen triangles. To the best of our knowledge, this is the first study to determine a high-temperature melt structure by the means of Raman spectroscopy combined with the DFT method.

(4) The Melt Structure in the $Li_2B_4O_7$ Crystal Growth System

The $Li_2B_4O_7$ (LTB) single crystal is a superior substrate for surface and bulk acoustic wave devices [10], and also used for the generation of the fourth and fifth harmonics of Nd: YAG lasers [59] and for neutron detection [11]. The crystal belongs to the tetragonal space group $I4_1cd$ with the unit cell parameters a = 9.477 Å, c = 10.286 Å, and Z = 8. Its structure is made up of $[B_4O_5Ø_4]^{2-}$ tetraborate groups and Li^+ ions [60]. The LTB crystal melts congruently and is often grown from a LTB melt by the Czochralski or Bridgman method [12].

High temperature Raman spectroscopy was used to investigate the melt structure in a LTB crystal–melt coexisting system [61]. The experimental process is similar to that in the study of the BMBO melt structure. After the LTB crystal melting, (1) the intense crystal peaks located around 720 cm^{-1} and in the range of 900–1200 cm^{-1} disappeared; (2) the high-frequency peaks in the range of 1300–1500 cm^{-1} anomalously blue-shifted (see Figure 14). In order to understand the structural origins of the spectral changes, the LTB crystal Raman spectrum was studied by CASTEP [61]. According to the CASTEP results, the Raman peaks in the 600–850 cm^{-1} range are assigned to the breathing vibrations of the boron–oxygen six-membered rings; the intense peaks located in the range of 900–1200 cm^{-1} mainly arise from the asymmetrical vibrations of the $BØ_4$ units; the high-frequency peaks located around 1436 cm^{-1} are assigned to the stretching vibrations of the extra-ring B_3–Ø bonds (B–Ø bonds of boron−oxygen triangles), as shown in Figure 15. The spectral changes during the melting process indicate that: (1) boron–oxygen six-membered rings remain in the melt although their structures might be different from those in the LTB crystal; (2) new structural units with extra-ring B_3–O bonds (not B_3–Ø bonds) present in the LTB melt because strong

Raman peaks located around 1500 cm^{-1} are often attributed to the stretching vibrations of the extra-ring B_3–O bonds.

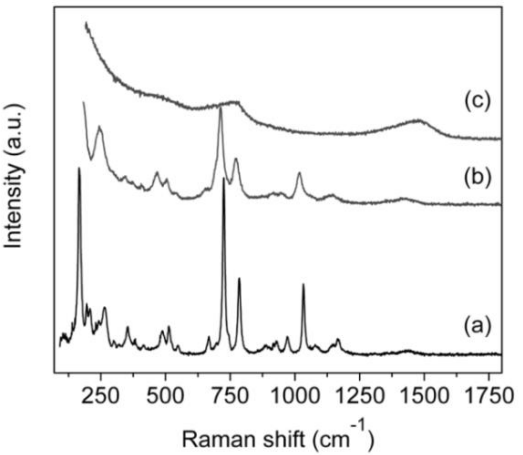

Figure 14. Raman spectra of LTB crystal and melt. (a) Crystal Raman spectrum recorded at 30 ^oC; (b) crystal Raman spectrum recorded at 500 ^oC; (c) melt Raman spectrum recorded near the melting point.

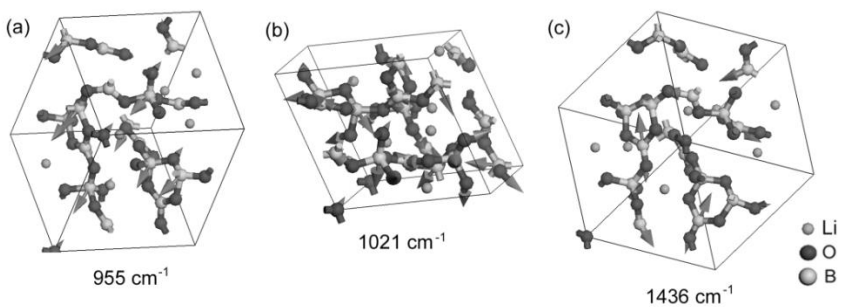

Figure 15. Atomic displacements of three important crystal Raman peaks.

A structural model has been proposed to describe the LTB melt on the basis of the above structural analysis [61]. The melt is made up of polymer-like boron–oxygen chains; its basic unit is the $[B_4O_6Ø_2]^{2-}$ group which is formed by a $[B_3O_4Ø_2]^-$ six-membered ring and a $[BOØ_2]^-$ triangle linked by a bridging oxygen atom. DFT calculations verified the melt structural model and provided accurate assignments for the vibrational bands present in the LTB

melt Raman spectrum (see Figure 16 and 17) [61]. The Raman band in the range of 250–500 cm^{-1} is attributed to the motions of the Li^+ ions; the Raman band in the range of 600–800 cm^{-1} is mainly related to the out-plane bending vibrations of the boron–oxygen triangle and the breathing vibration of the six-membered ring; the Raman band in the range of 1300–1600 cm^{-1} primarily arises from the stretching vibrations of the extra-ring B_3–O bond.

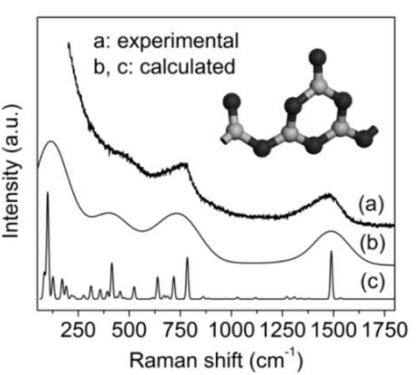

Figure 16. Experimental and calculated Raman spectra of the LTB melt. (a) Experimental Raman spectrum; (b) calculated Raman spectrum broadened by Gaussian line shape function with a FWHM of 200 cm^{-1}; (c) calculated Raman spectrum broadened by Gaussian line shape function with a FWHM of 10 cm^{-1}.

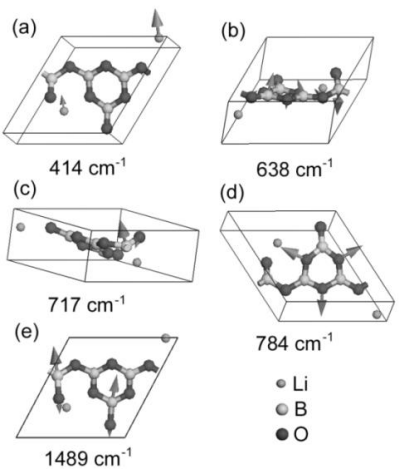

Figure 17. Atomic displacements of five strong peaks in calculated LTB melt Raman spectrum.

CONCLUSION

High-temperature Raman spectroscopy is an effective experimental tool to *in-situ* investigate high-temperature melt (solution) structures; the DFT calculation is a reliable theoretical method to establish the links between Raman spectra and micro-structures of crystals and melts. High-temperature Raman spectroscopy combining with the DFT calculation have successfully been applied to study the melt structures in some borate crystal growth systems. The following are some important conclusions drawn from our research: (1) Stable boron−oxygen groups, such as $[B_3O_6]^{3-}$ rings, can exist in not only crystal structures but also the corresponding melt structures. (2) An isomerization reaction, arising from the transformation between four-fold and three-fold coordinated boron atoms, is the most important micro-process taking place near the CBO, LBO, BIBO, and LTB crystal−liquid (melt or solution) interfaces. (3) When the CBO, BIBO, and LTB crystals melt, the continuous three-dimensional crystal networks collapse and transform into special borate−oxygen chains that have not been found in borate crystal structures. (4) Boundary layers whose solution structures are different from that in the bulk solutions have been found around the LBO and β-BBO crystal−solution interfaces. The boundary layers are about 50 μm in thickness. (5) The melt structures near the crystal–melt interfaces can be used to predict borate crystal growth habits, the predicted results are all in good agreement with the experimental.

I believe that the experimental and theoretical methods provided here can be extended to study the melt structures of many other inorganic compounds more than borates. The conclusions drawn in the chapter can help us deeply understand the macro-properties of borate melts and the micro-processes of borate crystal growth.

ACKNOWLEDGMENTS

The author thank the National Natural Science Foundation of China (Grant No. 50932005 and 51372246) for the financial support.

REFERENCES

[1] G. Heller, "Structural Chemistry of Boron and Silicon," in Topics in Current Chemistry, edited by F. L. Boschke (Springer-Verlag, New York, 1986), Vol. 131, pp. 39−98.

[2] ICSD—Inorganic Crystal Structure Database, National Institute of Standards and Technology and Fachinformationszentrum Karlsruhe, 2008.

[3] P. Becker, *Adv. Mater*., 1998, 10, 979−992.

[4] G. Q. Zhou, J. Xu, X. D. Chen, H. Y. Zhong, S. T. Wang, K. Xu, P. Z. Deng, and F. X. Gan, *J. Cryst. Growth*, 1998, 191, 517−519.

[5] S. Y. Zhang, X. Wu, Y. T. Song, D. Q. Ni, B. Q. Hu, and T. Zhou *J. Cryst. Growth* 2003, 252, 517−519.

[6] R. K. Li, and Y. Y. Ma, *CrystEngComm*, 2012, 14, 5421−5424.

[7] N. I. Leonyuk, and L. I. Leonyuk, *Prog. Cryst. Growth Charact. Mater*. 1995, 31, 179−278.

[8] Z. M. Liao, I. Jovanovic, C. A. Ebbers, Y. T. Fei, and B. Chai, *Opt. Lett.*, 2006, 31, 1277−1279.

[9] Y. J. Chen, Y. D. Huang, X. Q. Lin, Q. G. Tan, Z. D. Luo, and Y. F. Lin, *Appl. Phys. Lett.*, 2005, 86, 021115.

[10] R. W. Whatmore, N. M. Shorrock, C. O'hara, F. W. Ainger, and I. M. Young, *Electron. Lett.*, 1981, 17, 11−12.

[11] C. W. E. van Eijk, in Proceedings of the International Conference on Inorganic Scintillators and their Applications: Shanghai, China, 22–25 September, 1997, p. 3.

[12] S. M. Wan, "The Growth of Borate Crystals," in New Developments in Crystal Growth Research, edited by G. V. Karas (Nova Science Publishers, Virgina. 2005), pp. 1−38.

[13] E. F. Riebling, "Borate Glass," in Materials Science Research, edited by L. D. Pye, V. D. Frechette, and N. J. Kreidl (Plenum Press: New York, 1978), Vol. 12, p. 387.

[14] G. S. Henderson, G. Calas, and J. F. Stebbins, *Element*, 2006, 2, 269−273.

[15] W. J. Huisman, J. F. Peters, M. J. Zwanenburg, S. A. Vries, T. E. Derry, D. Abernathy, and J. F. Van der Veen, *Nature*, 1997, 390, 379−381.

[16] W. A. Curtin, *Phys. Rev. Lett.*, 1987, 59, 1228−1231.

[17] V. Ginkin, A. Kartavykh, and M. Zabudko, *J. Cryst. Growth*, 2004, 270, 329−339.

[18] N. Funamori, S. Yamamoto, T. Yagi, and T. Kikegawa, *J. Geophys. Res. Solid Earth*, 2004, 109, 1−8.
[19] C. Landron, L. Hennet, T. E. Jenkins, G. N. Greaves, J. P. Coutures, and A. K. Soper, *Phys. Rev. Lett.*, 2001, 86, 4839−4842.
[20] U. Breuer, O. Knauff, and H. P. Bonzel, *Phys. Rev., B* 1990, 41, 10848–10851.
[21] J. F. Stebbins, "Dynamics and Structure of Silicate and Oxide Melts: Nuclear Magnetic Resonance Studies," in Review in Mineralogy, edited by J. F. Stebbins, P. F. McMillan, and D. B. Dingwell (Mineralogical Society of America: Washington DC. 1995), Vol. 32, pp. 191−246.
[22] S. H. Oh, Y. Kauffmann, C. Scheu, W. D. Kaplan, and M. Rühle, *Science* 2005, 310, 661−663.
[23] T. Yano, N. Kunimine, S. Shibata, and M. Yamane, *J. Non-Cryst. Solids*, 2013, 321, 137−168.
[24] C.V. Raman, and K.S. Krishnan, *Nature*, 1928, 121, 501−502.
[25] M. C. Tobin, "Laser Raman spectroscopy," in Chemical Analysis, a Series of Monographs on Analytical Chemistry and Its Application, edited by P. J. Elving and I. M. Kolthoff (Wiley-Interscience: New York, 1971), pp. 1−30.
[26] B. O. Mysen, and J. D. Frantz, *Chem. Geol.*, 1992, 96, 321−332.
[27] Yu. K. Voron'ko, A. B. Kudryavtsev, V. V. Osiko, and A. A. Sobol', "Study of Melt Structure and Crystallization Processes by High-temperature Raman Spectroscopy," in Growth of Crystal, edited by S. Bagdasavov, and E. L. Lube (Consultants Bureau: New York, 1991), Vol.16, pp. 199−217.
[28] J. L. You, G. C. Jiang, H. Chen, Y. Q. Wu, K. D. Xu, and S. L. Zhang, in Synopsis of International Conference on Raman Spectroscopy: Gold Coast, Australia, 8–13 August, 2004, pp. 224−225.
[29] M. Yashima, M. Kakihana, R. Shimidzu, H. Fujimori, and M. Yoshimura, *Appl. Spectrosc.*, 1997, 51, 1224−1228.
[30] S. M. Wan, X. Zhang, S. J. Zhao, Q. L. Zhang, J. L. You, L. Lu, P. Z. Fu, Y. C. Wu and S. T. Yin, *Cryst. Growth Des.*, 2008, 8, 412−414.
[31] A. A. Osipov, and L. M. Osipova, *Physica B*, 2010, 405, 4718−4732.
[32] T. Uchino, and T. Yoko, *Solid State Ionics*, 1998, 105, 91−96.
[33] J. L. You, G. C. Jiang, H. Y. Hou, H. Chen, Y. Q. Wu, and K. D. Xu, *J. Raman Spectrosc*., 2005, 36, 237−249.
[34] P. Hohenberg, and W. Kohn, *Phys. Rev. B* 1964, 136, 864−871.
[35] X. Gonze, *Phys. Rev., A* 1995, 52, 1096−1114.

[36] S. Baroni, S. de Gironcoil, A. D. Corso, and P. Giannozzi, *Rev. Mod. Phys.*, 2001, 73, 515−562.
[37] D. Porezag, and M. R. Pederson, *Phys. Rev., B* 1996, 54, 7830−7836.
[38] M. D. Segall, P. J. D. Lindan, M. J. Probert, C. J. Pickard, P. J. Hasnip, S. J. Clark, and M. C. Payne, *J. Phys.: Condens. Matter.,* 2002, 14, 2717−2744.
[39] V. Milman, K. Refson, S. J. Clark, C. J. Pickard, J. R. Yates, S. P. Gao, P. J. Hasnip, M. I. J. Probert, A. Perlov, and M. D. Segall, *J. Mol. Struc. (THEOCHEM)* 2010, 954, 22−35.
[40] G. F. Wang, Q. Z. Huang, and J. K. Liang, *Acta Chim. Sinica, (Chinese)* 1984, 42, 503−508.
[41] H. Kouta, S. Imoto, and Y. Kuwano, *J. Cryst. Growth*, 1993, 128, 938−944.
[42] H. Ogawa, and Y. Waseda, *J. Cryst. Growth*, 1993, 128, 945−949.
[43] X. S. Lv, Y. L. Sun, J. Han, G. X. Gu, S. M. Wan, M. J. Cheng, S. L. Pan, and Q. L. Zhang, *J. Cryst. Growth*, 2013, 363, 220−225.
[44] X. S. Lv, Y. L. Sun, X. L. Tang, S. M. Wan, Q. L. Zhang, J. L. You, and S. T. Yin, *J. Cryst. Growth*, 2013, 371, 107−111.
[45] S. M. Wan, X. Zhang, S. J. Zhao, Q. L. Zhang, J. L. You, H. Chen, G. C. Zhang, and S. T. Yin, *J. Appl. Cryst.*, 2007, 40, 725−729.
[46] S. S. Liu, G. C. Zhang, S. M. Wan, X. X. Jiang, Y. Y. Wang, Z. S. Lin, and Y. C. Wu, *J. Appl. Cryst.*, 2014, 47, 739−744.
[47] J. Y. Huang, Y. R. Shen, C. T. Chen, and B. C. Wu, *Appl. Phys. Lett.*, 1991, 58, 1579−1581.
[48] Y. C. Wu, P. Z. Fu, J. X. Wang, Z. Y. Xu, L. Zhang, Y. F. Kong, and C. T. Chen, *Opt. Lett.*, 1997, 22, 1840−1842.
[49] C. T. Chen, Y. C. Wu, A. D. Jiang, G. M. You, R. K. Li, and S. J. Lin, *J. Opt. Soc. Am. B*, 1989, 6, 616−621.
[50] C. Parfeniuk, I. V. Samarasekera, F. Weinberg, J. Edel, K. Fjeldsted, and B. Lent, *J. Cryst. Growth*, 1996, 158, 514−533.
[51] I. Nikolov, D. Perlov, S. Livneh, E. Sanchez, P. Czechowicz, V. Kondilenko, and D. Loiacono, *J. Cryst. Growth*, 2011, 331, 1−3.
[52] A. Kokh, N. Kononova, G. Mennerat, Ph. Villeval, S. Durst, D. Lupinski, V. Vlezko, and K. Kokh, *J. Cryst. Growth*, 2010, 312, 1774−1778.
[53] Z. G. Hu, Y. Hao, Y. C. Yue, and X. S. Yu, *J. Cryst. Growth*, 2010, 335, 133-137.

[54] M. Hou, J. L. You, S. Patrick, G. C. Zhang, S. M. Wan, Y. Y. Wang, Z. F. Ji, L. H. Wang, P. Z. Fu, Y. C. Wu, and S. T. Yin, *CrystEngComm.*, 2011, 13, 3030−3034.

[55] D. Wang, S. M. Wan, S. T. Yin, Q. L. Zhang, J. L. You, G. C. Zhang, and P. Z. Fu, *CrystEngComm.*, 2011, 13, 5239−5242.

[56] H. Hellwig, J. Liebertz, and L. Bohaty, *Solid State Commun.*, 1998, 109, 249−251.

[57] R. Frohlich, L. Bohaty, and J. Liebertz, *Acta Crystallogr., Sect. C: Cryst. Struc. Commun.*, 1984, 40, 343−344.

[58] Y. L. Sun, S. M. Wan, X. S. Lv, X. L. Tang, J. L. You, and S. T. Yin, *CrystEngComm.*, 2013, 15, 220−225.

[59] R. Komatsu, T. Sugawara, K. Sassa, N. Sarukura, Z. Liu, S. Izumida, Y. Segawa, S. Uda, T. Fukuda, and K. Yamanouchi, *Appl. Phys. Lett.*, 1997, 70, 3492−3494.

[60] S. Natalis, B. Rimman, S. Jurii, F. Stanislav, and Y. Olga, *J. Alloys Compd.*, 2007, 428, 290−296.

[61] S. M. Wan, X. L. Tang, Y. L. Sun, G. C. Zhang, J. L. You, and P. Z. Fu *CrystEngComm.*, 2014, 16, 3086−3090.

In: Crystals and Crystal Growth
Editor: Wilfred Carter
ISBN: 978-1-63463-791-6
© 2015 Nova Science Publishers, Inc.

Chapter 3

DOPED ORGANIC CRYSTALS WITH HIGH EFFICIENCY, COLOR-TUNABLE EMISSION TOWARD LASER APPLICATION

Yang Zhao and Huan Wang*
College of Chemistry and Chemical Engineering,
Northeast Petroleum University, Daqing, P. R. China

ABSTRACT

Tetracene or pentacene -doped *trans*-1,4-Distyrylbenzene (*trans*-DSB) crystals with high crystalline quality, high doping ratio, large size and excellent optical properties were prepared by physical vapor transport method. Efficient energy transfer from the host *trans*-DSB molecules to the guest molecules and the suppressing of the interaction among the guest molecules lead to color-tunable emission and high luminescent efficiencies. These doped crystals maintain the ordered layer structures and the crystal surface continuities, which are verified by X-ray diffraction (XRD) and atomic force microscopy (AFM) analysis. Further, the white-emission tetracene and pentacene -doped *trans*-DSB crystal with the CIE coordinate (0.36, 0.37) has been obtained by controlling an appropriate mol ratio of guest to host (tetracene: pentacene: *trans*-DSB= 1: 1.35: 23.1).

* Corresponding author: Huan Wang. College of Chemistry and Chemical Engineering, Northeast Petroleum University, 199 Fazhan Road, Daqing 163318 P. R. China. E-mail: wanghuan83214@gmail.com.

The primary results of optically pumped laser experiment indicate that these crystals have the potential application for organic laser diodes.

INTRODUCTION

Organic single crystals constructed by π-conjugated molecules have attracted great attention in the field of organic optoelectronic materials [1]. The academic motivation for organic single crystal research is their definite structures, which provides a model to investigate the basic interactions between the molecules (supramolecular interaction), and the relationship between molecular stacking modes and optoelectronic performance (luminescence and carrier mobility) [2]. In the meanwhile, the superiorities of organic crystals such as high thermal stability, high ordered structure and high carrier mobility make them attractive candidates for optoelectronic devices such as optically pumped lasers [3], field-effect transistors [4], electroluminescence [5], and photovoltaic cell [6].

The solid state organic lasers have been demonstrated clearly by some groups. Typically, F. Hide et al. [7] observed gain narrowing from the optically pumped thin-film waveguide. N. Tessler et al. [8] made the first vertical microcavity laser based on conjugated polymers as gain materials. Subsequently, optically pumped laser action has been demonstrated in a broad range of conjugated polymers and oligomers [9]. Despite success in optically pumped lasing, the electrically pumped 'injection laser' remains a significant challenge. There are three main issues to be considered relating to the feasibility of electrically pumped organic semiconductor lasers: i) the required current densities, ii) the additional losses due to the contacts, and iii) the additional losses due to the injected charges referred to as polarons and triplet formation [10]. All three main issues outlined above relate to the low mobility of organic semiconductors. The low mobility makes it hard to achieve high current densities. It also means that losses due to absorption of the contacts cannot simply be resolved by making the light-emitting layer much thicker so that the electric field of the guided mode has little overlap with the contacts. The high concentration of polarons is due to their low mobility. Hence higher mobility helps with each of these issues, so recent reports of a polyfluorene-based material with mobility of 10^{-2} cm^2/Vs are encouraging [11]. In fact, OLED materials development has evolved in a different direction toward amorphous materials because they are less prone to recrystallization and less susceptible to intermolecular interactions, which can quench luminescence.

Consequently, the organic crystals combining efficient light emission and high charge-carrier mobility could be suitable as the candidates for electrically driven organic lasers because firstly their inherent long-range structural ordering could effectively avoid excitons annihilations that causing the sharp decrease of luminescence quantum efficiency under the high current densities [12], and secondly their thicknesses (usually 1~10 μm), much larger than most of spin-coated and vacuum-deposited films', benefit to move the light-emitting active layer far away from the loss regions contacted with the metal electrode in the vertical diode structure.

For the traditional organic optoelectronic polycene materials such as tetracene, pentacene, it is difficult to get high-luminescence-efficiency crystals and their crystals are hardly applied in electroluminescence or lasers. As we know, doping dye molecules into certain host materials is a general method to increase the luminescent efficiency of the guest molecules for the organic amorphous materials [13]. Another merit of doping is that it can shift the emission away from the absorption region of the host to decrease the absorption loss of lasers. Thus, achieving desirable light-emission doped crystal is significant towards laser application because high carrier mobility is regarded as the inherent characteristics compared with the amorphism. Doped organic molecular crystals have been paid much attention as early as 1970's and stimulated emissions in some systems were observed in succession [14]. Further in-depth photophysical characterizations of doped systems revealed the relationships between basic optoelectronic functions and molecular structures [15]. But most of them were based on micro- or nano-crystals due to crystal growth method selected, in which lack of structural definition and smaller size limited the application in optoelectronic devices. This might be due to the lattice mismatch and the weak intermolecular interactions in organic crystals resulting in the difficulty of large-size doped crystal growth. Physical vapor transport (PVT) method is the common one to obtain high-quality and large-size organic single crystal [16]. Based on the principle of structural comparability (including molecular structures and their stacking modes) and spectrum overlap between the host and guest (ensuring efficient energy transfer), we successfully dope a certain quantity of tetracene or pentacene (doping ratios approximate to 10%) into *trans*-1,4-Distyrylbenzene (*trans*-DSB) crystal by PVT method, and maintain the structural orderings of doped crystals as proved by X-ray diffraction (XRD) and atomic force microscopy (AFM) analysis. These doped crystals have large sizes (several millimeters), high luminescent efficiency (65±4% for the undoped *trans*-DSB, 74±4% for the tetracene-doped *trans*-DSB, and 28±4% for the pentacene-doped *trans*-

DSB crystals) and color-tunable emission (blue for the undoped *trans*-DSB, green for the tetracene-doped *trans*-DSB and red for the pentacene-doped *trans*-DSB crystals). The spectra narrowings caused by amplified spontaneous emission (ASE) from the undoped *trans*-DSB, tetracene-doped *trans*-DSB and pentacene-doped *trans*-DSB crystals are observed, which show the potential application of light-emitting transistors, diodes and lasers. The molecular structures of *trans*-DSB, tetracene and pentacene are shown in Figure 1a.

As shown in Figure 1b-d, 1b is the pure undoped *trans*-DSB crystal; 1c is the tetracene-doped *trans*-DSB crystal (tetracene: *trans*-DSB=1: 14.7, mol ratio); and 1d is the pentacene-doped *trans*-DSB crystal (pentacene: *trans*-DSB=1: 13.1, mol ratio). Blue, green and red emissions from the three crystals are observed, respectively. The three crystals have the slice shape, smooth surface and large size of several millimeters. The emissions from the edges of the crystals are stronger than that from the body surfaces, which indicates that the self-waveguided emission occurs in the crystals.

MORPHOLOGY AND STRUCTURE OF THE CRYSTALS

Figure 2a-c shows the AFM height images at the edge areas of the *trans*-DSB, tetracene-doped *trans*-DSB and pentacene-doped *trans*-DSB crystals. Step-like morphologies have been found.

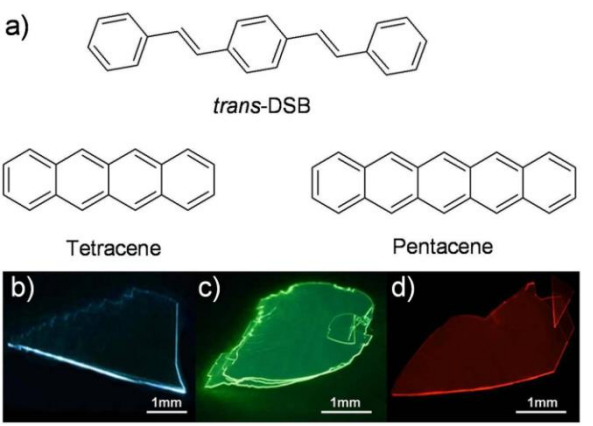

Figure 1. (a) The molecular structures of *trans*-DSB, tetracene, pentacene; (b) The pure undoped *trans*-DSB crystal; (c) Tetracene-doped *trans*-DSB crystal (tetracene: *trans*-DSB=1: 14.7, mol ratio); (d) Pentacene-doped *trans*-DSB crystal (pentacene: *trans*-DSB=1: 13.1, mol ratio) photographs under the ultraviolet lamp.

From the cross-section analyses, the average heights of steps observed on the three crystal surfaces are about 1.91 nm, 1.93 nm and 1.98 nm, respectively. The step heights of undoped and doped crystals are nearly not different. Figure 2d shows the diffraction patterns of Wide-angle X-ray diffraction (XRD) on the slice crystals.

As can be seen, the diffraction peaks occur equidistantly with angle degree varying, the baselines of the XRD patterns are straight and the diffraction peaks are very sharp, so these slice crystals should have the good ordered layer structures. The lattice parameters of *trans*-DSB were reported by Wu et al. [17]: a=5.87 Å, b=7.70 Å, c=34.87 Å. Possible herringbone arrangement of *trans*-DSB molecules in crystal was recognized in previous work [18].

According to the Bragg equation the thicknesses of one molecular layer of *trans*-DSB, tetracene-doped *trans*-DSB and pentacene-doped *trans*-DSB crystals are calculated to be 1.72, 1.74 and 1.75nm, respectively, which correspond to the one-step height of these crystals in AFM image. The values are summarized in Table 1.

Comparing the lattice constant with the XRD results, we notice that the primary diffraction spacing of *trans*-DSB crystal is approximately identical to the monolayer height (c/2= 17.43 Å) of *trans*-DSB molecules along *ab*-plane direction, which indicate that the *ab*-plane is parallel to the crystal surface of *trans*-DSB. Also, the directions of intermolecular π-π stacking of the undoped *trans*-DSB crystal, and of the tetracene-doped *trans*-DSB crystal and pentacene-doped *trans*-DSB crystal are all along *ab*-plane, based on the analysis of XRD patterns.

Table 1. Summaries of the molecular layer thicknesses and step heights of undoped and doped crystals through XRD and AFM analyses

Crystal	*trans*-DSB	Tetracene-doped *trans*-DSB	Pentacene-doped *trans*-DSB
Layer thickness (nm)/XRD	1.72	1.74	1.75
Step height (nm)/AFM[a]	1.91 (±0.15)	1.93 (±0.15)	1.98 (±0.15)

[a]Step heights from cross-section analyses in different regions of crystal surface exist slightly differences and the values listing in the table is the statistic average. The value ±0.15 in parentheses represents statistic zone. The calculated layer thickness corresponded well with the step height observed by AFM, but generally ~0.2 nm smaller than AFM results, due to systematic error brought by instrument existing in the process of scanning AFM images.

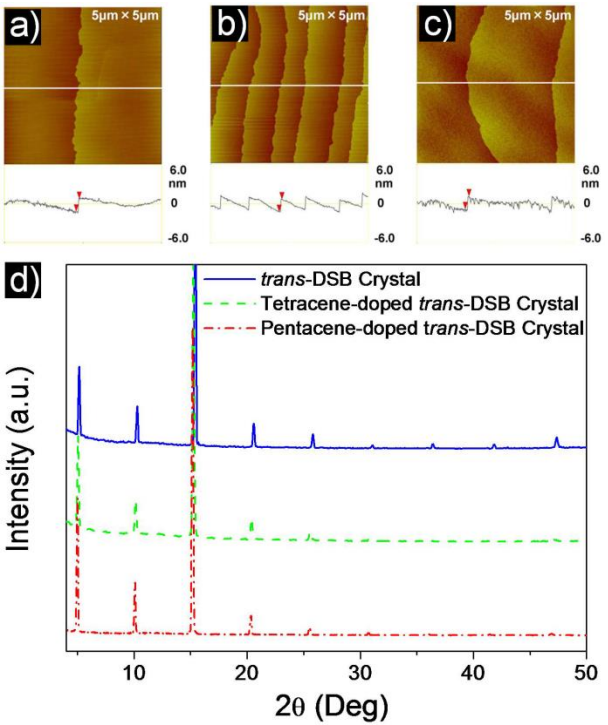

Figure 2. (a) *trans*-DSB; (b) tetracene-doped *trans*-DSB; (c) pentacene-doped *trans*-DSB slice crystal surface AFM height images; (d) XRD patterns of *trans*-DSB crystal, tetracene-doped *trans*-DSB crystal and pentacene-doped *trans*-DSB crystal.

The results of AFM morphologies and X-ray diffraction patterns suggest that all the crystals (undoped and doped) have the layer-by-layer structure and each layer corresponds to a molecular monolayer.

So the structural ordering of the host *trans*-DSB crystals has been retained after doping a certain quantity of tetracene or pentacene molecules into them. Doping tetracene or pentacene into *trans*-DSB crystal leads the layer space to a little larger, which may be due to the disturbance of the intrinsic *trans*-DSB crystal lattices caused by the embedment of doped molecules.

Structural comparability of the host and guest molecules is an important precondition for realizing the successful growth of heavy doping and large size crystal by PVT method, which is beneficial for different intermolecular combination in the crystal formation process and structural ordering maintenance. In our doped system, both *trans*-DSB as the host molecules and tetracene or pentacene as the guest molecules are all the linear configurations

and the molecules in the crystals are arranged in similar configuration, namely "herringbone" type structure in *ab*-plane, as proved in previous work [19], where edge-to-face arene-arene interactions are much stronger than intermolecular interactions along c axis direction, thus easy to form layer-by-layer structures. Further, in the doped crystal formation process, host and guest molecules could freely diffuse onto crystal surface from vapor, and then combine with neighboring molecules through intermolecular interaction to form an intact layer. A certain quantity of doped guest molecules may replace the locations of original host molecules in crystal lattice. The emission wavelengths and quantum yields of these several undoped and doped crystals are summarized and listed in the Table 2.

OPTICAL PROPERTIES

Figure 3a shows the absorption spectra of *trans*-DSB crystal, tetracene-doped *trans*-DSB crystal and pentacene-doped *trans*-DSB crystal. The tetracene or pentacene -doped crystals display the similar absorption consistent with that of undoped crystal that nearly comes from host *trans*-DSB crystal. Figure 3b shows the emission spectra of *trans*-DSB crystal, tetracene-doped *trans*-DSB crystal and pentacene-doped *trans*-DSB crystal. The PL spectra of tetracene-doped *trans*-DSB crystal shows that the emission mainly comes from the tetracene molecules verifying the energy transfer.

The emission peaks of tetracene molecules in the doped crystals have about 20 nm red shifts relative to that of tetracene molecules in solution, which may be caused by the conjugated effect of tetracene with the surrounding *trans*-DSB molecules (The 0-1 transition emissions of tetracene solution and crystal are about 511 nm and 531 nm, respectively). The similar phenomenon is also observed in the pentacene-doped *trans*-DSB crystal.

Table 2. Summaries of the emission wavelengths and quantum yields of some undoped and doped crystals

Crystal	Emission Wavelenght (nm)			Quantum Yield
	0-0	0-1	0-2	
Trans-DSB	444	467	500	65±4%
Tetracene-doped *trans*-DSB	497	531	572	74±4%
Pentacene-doped *trans*-DSB	603	654	–	28±4%

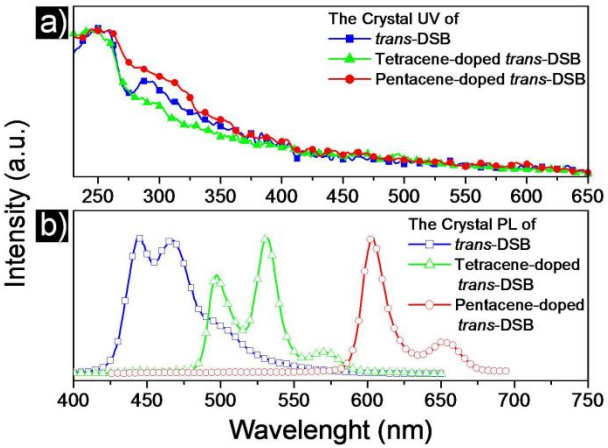

Figure 3. (a) The absorption spectra of *trans*-DSB crystal, tetracene-doped *trans*-DSB crystal and pentacene-doped *trans*-DSB crystal; (b) The emission spectra of *trans*-DSB crystal, tetracene-doped *trans*-DSB crystal and pentacene-doped *trans*-DSB crystal.

The herringbone arrangement of tetracene and pentacene molecules in the solid-state can quench the luminescence sharply, so their luminescent efficiencies in aggregated state are no more than 1%.

But doping tetracene or pentacene into a host crystal could effectively avoid the intermolecular aggregates. The crystalline-state PL efficiencies of the tetracene-doped *trans*-DSB and pentacene-doped *trans*-DSB crystals are as high as 74±4% and 28±4%, respectively.

The absorption and emission separation of doped crystals will be advantageous in the lasers due to effectively decreasing the loss brought from self-absorption.

By controlling the doped content of tetracene or pentacene molecules in *trans*-DSB crystals, several crystals with different color emission are obtained, as shown in Figure 4. From the photographs of these doped crystals, the emissions from the edges are stronger than those from the body surfaces, which favor the application in laser. The respective ratios of guest molecules to host molecules in different color emission crystals could be estimated by chromatograph analysis.

For example, the mol ratios of tetracene to *trans*-DSB in the crystals shown in Figure 1c (green emission) and Figure 4a (sky-blue emission) are approximate 1:14.7 and 1:33, respectively. And the mol ratios of pentacene to *trans*-DSB in the crystals shown in Figure 1d (deep-red emission) and Figure 4c (light-red emission) are approximate 1:13.1 and 1:27.8, respectively.

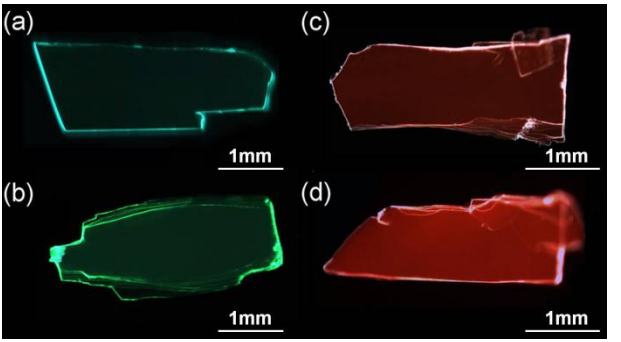

Figure 4. The photographs of tetracene-doped *trans*-DSB crystals with different color emission (a, b); pentacene-doped *trans*-DSB crystals with different color emission (c, d) under the ultraviolet lamp.

With the increase of the doped content of tetracene or pentacene molecules the energy transfer from the host to the guest increases, while induces the decrease of the host emission. It is found that the ratio of guest molecules to the host molecules is mainly influenced by the growth-zone temperature. The higher the growth-zone temperature is, the bigger the ratio of guest molecules to the host molecules is, and the worse the quality of the crystals is. This is because when the growth-zone temperature is higher, the disturbance of host-crystals lattice is more intense inducing the guest molecules to be more easily embedded into the host-crystals.

AMPLIFIED SPONTANEOUS EMISSION EXPERIMENT

Doping of organic amorphous films with dye molecules has been widely utilized to tune the emission wavelength and reduce the lasing threshold by shifting the emission to longer wavelengths where the residual absorption is smaller [20]. Here, we realize the blue, green and red amplified spontaneous emission (ASE) from the organic crystals by the doping method. Under the ultraviolet lamp, the emissions from the edges of all tested crystals are stronger than that from the body surface, which indicates that the self-waveguided emission occurs. Waveguided propagation of the emission is thought to be one prerequisite for lasing. In the optically pumped laser experiment the slice crystals are glued on the surface of the quartz substrates.

Due to the strong intermolecular aggregates, pure tetracene and pentacene crystals show very low luminescent efficiencies (no more than 1%), and the

ASE phenomena of them have never been reported. The fluorescence quantum yield is not only determined by the radiative rate, but also by the emissive traps in the condensed phase. Although *trans*-DSB crystallizes in a herringbone arrangement, the quantum yield is as high as up to 65±4%. This is because the *trans*-DSB crystal has low defect concentrations, as proved in previous work [18b]. However, the doped *trans*-DSB crystals with tetracene or pentacene present high luminescent efficiencies and the ASEs from tetracene or pentacene in the doped crystals can be observed, which is mainly ascribed to the suppressing of the interaction among the doped molecules. When the incident laser fluence is increased, the emission peak intensities nonlinearly grow, accompanied by the narrowing of the emission spectra, which indicated the narrowing is caused by gain- narrowing, namely ASE. For tetracene-doped *trans*-DSB crystal, the FWHMs of the peak at 531 nm (0-1 transition) change from 18 nm at 2.4 μJ/pulse to 4 nm at 120 μJ/pulse and the threshold for the ASE is about 12 μJ/pulse from the non-linear variation of the peak intensity with the pump energy increasing. Figure 5 shows the blue (467 nm), green (531 nm) and red (660 nm) ASEs spectra of undoped *trans*-DSB, tetracene-doped *trans*-DSB and pentacene-doped *trans*-DSB crystals. The ASEs from the pure *trans*-DSB, tetracene and pentacene -doped *trans*-DSB crystals are all occurs at the emission of 0-1 transition, which suggests that the 0-1 transition has the highest gain and the self absorption causes the relatively lower gain of 0-0 transition. PL quantum efficiency, minimum FWHM and threshold defined of undoped or doped crystals have been summarized in the Table 3.

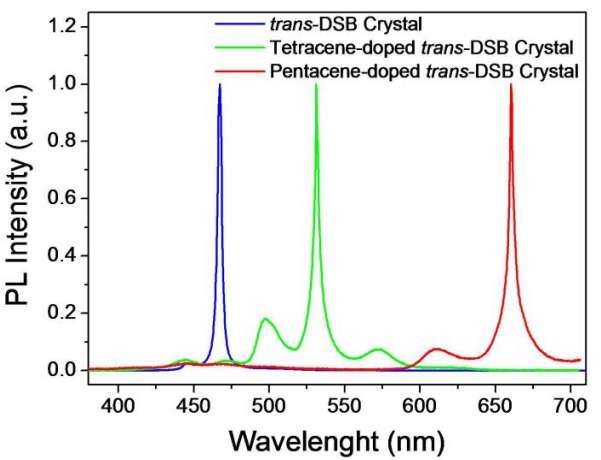

Figure 5. The ASEs spectra of undoped *trans*-DSB, tetracene-doped *trans*-DSB and pentacene-doped *trans*-DSB crystals.

Table 3. PL quantum efficiency (QE), Min. FWHM and threshold of ASE for different organic crystals

Crystals		*Trans*-DSB	Tetracene	Pentacene	Tetracene-doped *trans*-DSB	Pentacene-doped *trans*-DSB
PL QE		65±4%	<1%	<1%	74±4%	28±4%
Min. FWHM (nm)		4 nm	No	No	4 nm	4 nm
Threshold	(μJ/pulse)	9.7	No	No	12	70.4
	(KW/cm^2)	48.5	No	No	60	352

WHITE-LIGHT EMISSIVE DOPED CRYSTAL AND TIME-RESOLVED PROPERTIES

By optimizing the crystal growth conditions a series of doubly doped white-emission crystals (tetracene and pentacene -doped *trans*-DSB) with the Commission International del'Eclairage (CIE) coordinates approaching to an ideal white light (0.33, 0.33) were obtained (Figures 6a). Figures 6b and 6c show the CIE coordinates of (0.36, 0.37) and photoluminescence (PL) spectrum corresponding to the tetracene and pentacene -doped *trans*-DSB crystal (tetracene: pentacene: *trans*-DSB= 1: 1.35: 23.1, determined by chromatograph analysis) in Figure 6a.

Figure 7a shows the PL decay curves of tetracene-doped *trans*-DSB crystals with different mol ratios (tetracene: *trans*-DSB= 1: 33, 1: 18), and the white-emission tetracene and pentacene -doped *trans*-DSB crystal (tetracene: pentacene: *trans*-DSB= 1: 1.35: 23.1, mol ratio) monitored at the emission wavelength of 444 nm. The decay time of the donor *trans*-DSB in tetracene-doped *trans*-DSB crystals with two different mol ratios (tetracene: *trans*-DSB= 1: 33, 1: 18) are 1.49 ns and 1.04 ns, respectively.

However, the decay time of the donor *trans*-DSB in the white-emission tetracene and pentacene -doped *trans*-DSB crystal (tetracene: pentacene: *trans*-DSB= 1: 1.35: 23.1, mol ratio) decreases to 0.11 ns, where the mol ratio of tetracene to *trans*-DSB (1: 23.1) is in between 1: 33 and 1: 18. That means not only the existence of energy transfer from the donor *trans*-DSB to the acceptor tetracene, but also from *trans*-DSB to the acceptor pentacene in the white-emission doped crystal. Figure 7b shows the PL decay curves of tetracene-doped *trans*-DSB crystals with different mol ratios (tetracene: *trans*-DSB= 1: 33, 1: 18), and the white-emission tetracene and pentacene -doped

trans-DSB crystal (tetracene: pentacene: *trans*-DSB= 1: 1.35: 23.1, mol ratio) monitored at the emission wavelength of 531 nm.

The decay time of the acceptor tetracene in tetracene-doped *trans*-DSB crystals with two different mol ratios (tetracene: *trans*-DSB= 1: 33, 1: 18) are 10.01 ns and 14.51 ns, respectively. However, the decay time of the acceptor tetracene in the white-emission tetracene and pentacene -doped *trans*-DSB crystal (tetracene: pentacene: *trans*-DSB= 1: 1.35: 23.1, mol ratio) decreases to 2.37 ns. That indicates the efficient energy transfer from tetracene to pentacene exists in the white-emission doped crystal. Figure 7c shows the PL decay curves of pentacene-doped *trans*-DSB crystals with different mol ratios (pentacene: *trans*-DSB= 1: 28, 1: 16), and the white-emission tetracene and pentacene -doped *trans*-DSB crystal (tetracene: pentacene: *trans*-DSB= 1: 1.35: 23.1, mol ratio) monitored at the emission wavelength of 608 nm. The decay time of the acceptor pentacene in the white-emission doped crystal is 8.06 ns between the ones (6.92 ns and 8.29 ns) of pentacene-doped *trans*-DSB crystals with two different mol ratios (pentacene: *trans*-DSB= 1: 28, 1: 16).

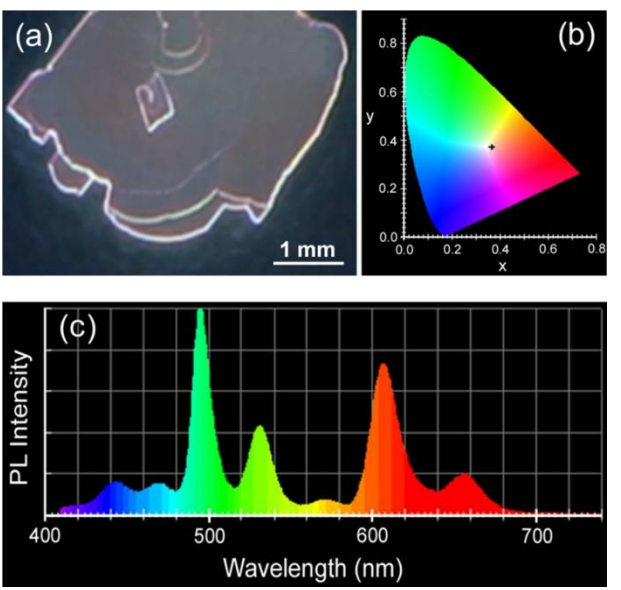

Figure 6. (a) Photograph of white-emission tetracene and pentacene -doped *trans*-DSB crystal (tetracene: pentacene: *trans*-DSB= 1: 1.35: 23.1, mol ratio) under the irradiation of ultraviolet lamp (365 nm); (b) CIE chromaticity diagram marked as a cross (0.36, 0.37) corresponding to the emission of the crystal. (c) PL spectrum of the tetracene and pentacene -doped *trans*-DSB crystal (λ_{ex} = 400 nm).

This indicates the decay time of pentacene molecules in doped crystals is proportional to its doping concentration. Based on the above analyses, there are the energy transfer not only from *trans*-DSB to tetracene and pentacene, but also from tetracene to pentacene in the white-emission tetracene and pentacene -doped *trans*-DSB crystal. A summary of transient PL decay time for the above systems is given in Table 4.

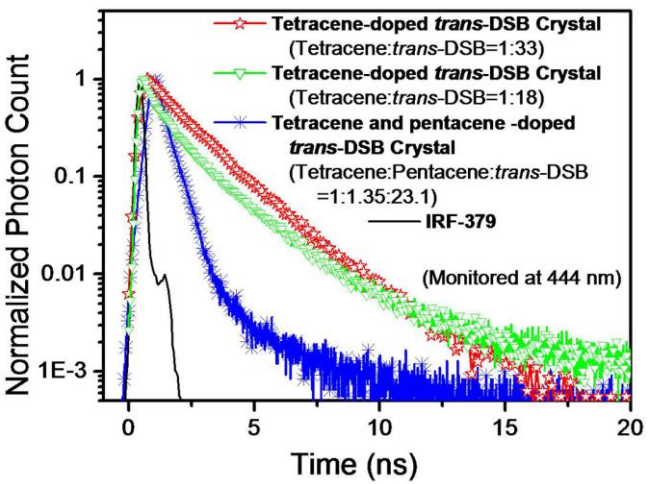

a

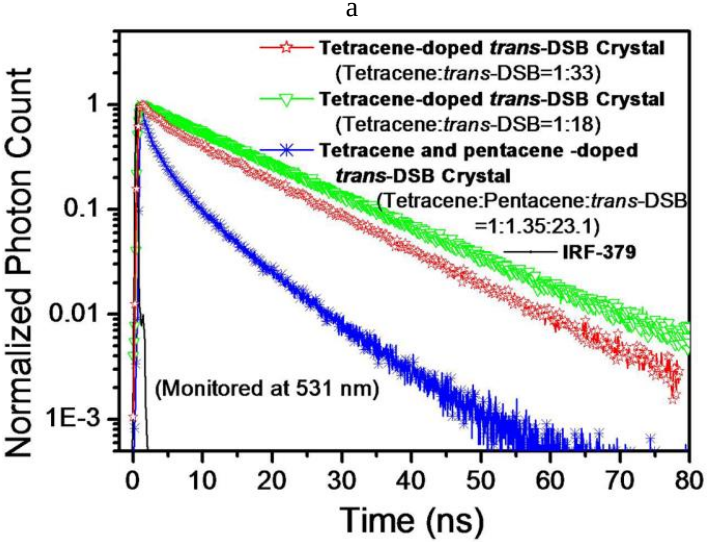

b

Figure 7. (Continued).

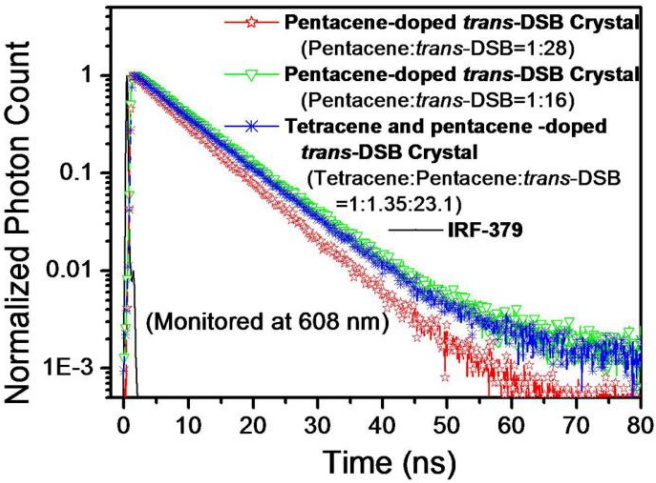

c

Figure 7. Time-resolved fluorescences of tetracene-doped *trans*-DSB with different mol ratios (tetracene: *trans*-DSB= 1: 33, 1: 18), pentacene-doped *trans*-DSB with different mol ratios (pentacene: *trans*-DSB= 1: 28, 1: 16), and white-emission tetracene and pentacene -doped *trans*-DSB (tetracene: pentacene: *trans*-DSB= 1: 1.35: 23.1, mol ratio) crystals monitored at different emission wavelengths: (a) λ_{em} =444 nm; (b) λ_{em} =531 nm; (c) λ_{em} =608 nm. The black solid lines show the decay curves of IRF-379.

CONCLUSION

The physical vapor transport method is verified to get the doped organic crystals effectively and several color-tunable, large-size and high-quality doped organic crystals are obtained. The results of XRD and AFM indicate that the ordered layer structure and thin film surface continuity of the host crystals have been maintained after doping a certain quantity of tetracene or pentacene into them. The structural comparability of host and guest molecules is an important factor in the doped crystal growth, specially for the ones with large size and heavy doping. Efficient energy transfer exists in doped crystals verified by steady-state and time-resolved fluorescence spectroscopy. Pure *trans*-DSB, tetracene and pentacene -doped *trans*-DSB crystals show the blue, green and red emission, respectively.

Further, the white-emission tetracene and pentacene -doped *trans*-DSB crystal with the CIE coordinate (0.36, 0.37) has been obtained by controlling an appropriate mol ratio of guest to host (tetracene: pentacene: *trans*-DSB= 1:

1.35: 23.1) in which the energy transfer exist not only from *trans*-DSB to tetracene and pentacene, but also from tetracene to pentacene. The primary results of optically pumped laser experiment indicate that these crystals have the potential application for organic laser diodes.

Table 4. Decay data of the white-emission tetracene and pentacene -doped trans-DSB crystal (tetracene: pentacene: *trans*-DSB= 1: 1.35: 23.1, mol ratio), tetracene-doped *trans*-DSB crystals with different mol ratios (tetracene: *trans*-DSB= 1: 33, 1: 18), and pentacene-doped *trans*-DSB crystals with different mol ratios (pentacene: trans-DSB= 1: 28, 1: 16) at the emission wavelengths of 444 nm, 531 nm and 608 nm

Crystal	Decay time τ (ns)	Percentage (%)	Mean lifetime τ (ns)	λ_{em} (nm)
Tetracene and pentacene -doped *trans*-DSB crystal (tetracene: pentacene: *trans*-DSB= 1: 1.35: 23.1)	0.79 0.09	2.67 97.33	0.11	444 nm
	7.30 0.86	23.39 76.61	2.37	531 nm
	8.06	100	8.06	608 nm
Tetracene-doped *trans*-DSB crystal (1: 33)	2.28 1.04	36.09 63.91	1.49	444 nm
	13.23 2.110	71.07 28.93	10.01	531 nm
Tetracene-doped *trans*-DSB crystal (1:18)	1.94 0.50	34.47 65.20	1.04	444 nm
	14.51	100	14.51	531 nm
Pentacene-doped *trans*-DSB crystal (1: 28)	6.92	100	6.92	608 nm
Pentacene-doped *trans*-DSB crystal (1: 16)	8.29	100	8.29	

REFERENCES

[1] Pope, M., Kallmann, H. P., Mangnante, P. *J. Chem. Phys*. 1963, 38, 2042-2043.; b) Avanesjan, O. S., Benderskii, V. A., Brikenstein, V. K., Broude, V. L., Korshunov, L. I., Lavrushko, A. G., Tartakovskii, I. I. *Mol. Cryst. Liq. Cryst*. 1974, 29, 165-174.; c) Fichou, D., Delysee, S., Nunzi, J. M. *Adv. Mater*. 1997, 9, 1178-1181.; d) Butko, V. Y., Chi, X., Ramirez, A. P. *Solid State Commun*. 2003, 128, 431-434.

[2] Reese, C., Bao, Z. N. *J. Mater. Chem*. 2006, 16, 329-333.; b) Xie, Z. Q., Yang, B., Li, F., Cheng, G., Liu, L. L., Yang, G. D., Xu, H., Ye, L., Hanif, M., Liu, S. Y., Ma, D. G., Ma, Y. G. *J. Am. Chem. Soc*. 2005, 127, 14152-14153.

[3] Yanagi, H., Ohara, T., Morikawa, T. *Adv. Mater*. 2001, 13, 1452-1455.; b) Ichikawa, M., Hibino, R., Inoue, M., Haritani, T., Hotta, S., Koyama, T., Taniguchi, Y. *Adv. Mater*. 2003, 15, 213-217.

[4] Sundar, V. C., Zaumseil, J., Podzorov, V., Menard, E., Willett, R. L., Someya, T., Gershenson, M. E., Rogers, J. A. *Science* 2004, 303, 1644-1646.; b) Briseno, A. L., Mannsfeld, S. C. B., Ling, M. M., Liu, S., Tseng, R. J., Reese, C., Roberts, M. E., Yang, Y., Wudl, F., Bao, Z. N. *Nature* 2006, 444, 913-917.

[5] Hisao, Y., Takayuki, M., Hotta, S. *Appl. Phys. Lett*. 2002, 81, 1512-1514.

[6] Tseng, R. J., Chan, R., Tung, V. C., Yang, Y. *Adv. Mater*. 2008, 20, 435-438.

[7] Hide, F., M. Díaz-García, A., Schwartz, B. J., Andersson, M. R., Pei, Q., Heeger, A. J. *Science* 1996, 273, 1833-1836.

[8] Tessler, N., Denton, G. J., Friend, R. H. *Nature* 1996, 382, 695-697.

[9] Tessler, N. *Adv. Mater*. 1999, 11, 363-370.; b) Bulovic, V., Kozlov, V. G., Khalfin, V. B., Forrest, S. R. *Science* 1998, 279, 553-555.; c) Moll, N., Mahrt, R. F., Bauer, C., Giessen, H., Schnabel, B., Kley, E. B., Scherf, U. *Appl. Phys. Lett*. 2002, 80, 734-736.; d) Reufer, M., Riechel, S., Lupton, J. M., Feldmann, J., Lemmer, U., Schneider, D., Benstem, T., Dobbertin, T., Kowalsky, W., Gombert, A., Forberich, K., Wittwer, V., Scherf, U. *Appl. Phys. Lett*. 2004, 84, 3262-3264.; e) Heliotis, G., Xia, R. D., Turnbull, G. A., Andrew, P., Barnes, W. L., Samuel, I. D. W., Bradley, D. D. C. *Adv. Funct. Mater*. 2004, 14, 91-97.

[10] Samuel, I. D. W., Turnbull, G. A. *Chem. Rev*. 2007, 107, 1272-1295.

[11] Yap, B. K., Xia, R. D., Campoy-Quiles, M., Stavrinou, P. N., Bradley, D. D. C. *Nat. Mater*. 2008, 7, 376-380.

[12] Takenobu, T., Bisri, S. Z., Takahashi, T., Yahiro, M., Adachi, C., Iwasa1, Y. *Phys. Rev. Lett*. 2008, 100, 066601.

[13] Tang, C. W., VanSlyke, S. A., Chen, C. H. *J. Appl. Phys*. 1989, 65, 3610-3616.

[14] Naboikin, Y. V. L., Ogurtsova, A., Podgornyi, A. P., Malkes, L. Y. *Sov. J. Quantum. Electron* 1978, 8, 457-461.; b) Avanesyan, H. S., Benderskii, V. A., Brikenshtein, V. K., Lavrushko, A. G., Filippov, P. G. *Phys. Stat. Sol*. (a) 1975, 30, 781-789.; c) Schwoerer, M., Wolf, H. C. *Organic Molecular Solids*; Wiley-VCH 2007.

[15] Egelhaaf, H.-J., Gierschner, J., Oelkrug, D. *Synth. Met*. 2002, 127, 221-227.; b) Gierschner, J., Egelhaaf, H.-J., Oelkrug, D., Müllen, K. J. *Fluorescence* 1998, 8, 37-44.; c) Oelkrug, D., Tompert, A., Gierschner, J., Egelhaaf, H.-J., Hanack, M., Hohloch, M., Steinhuber, E. *J. Phys. Chem. B* 1998, 102, 1902-1907.; d) Zhao, Y. S., Fu, H. B., Hu, F. Q., Peng, A. D., Yang, W. S., Yao, J. N. *Adv. Mater*. 2008, 20, 79-83.

[16] Laudise, R. A., Kloc, C., Simpkins, P. G., Siegrist, T. *J. Cryst. Growth* 1998, 187, 449-454.

[17] Wu, C. C., Delong, M. C., Vardeny, Z. V., Ferraris, J. P. *Synth. Met*. 2003, 137, 939-941.

[18] Spano, F. C. *Ann. Rev. Phys. Chem*. 2006, 57, 217-243.; b) Gierschner, J., Ehni, M., Egelhaaf, H.-J., Milián Medina, B., Beljonne, D., Benmansour, H., Bazan, G. C. *J. Chem. Phys*. 2005, 123, 144914.

[19] Cuppen, H. M., Graswinckel, W. S., Meekes, H. *Cryst. Growth Des*. 2004, 4, 1351-1357.; b) Ruiz, R., Choudhary, D., Nickel, B., Toccoli, T., Chang, K. C., Mayer, A. C., Clancy, P., Blakely, J. M., Headrick, R. L., Iannotta, S., Malliaras, G. G. *Chem. Mater*. 2004, 16, 4497-4508.

[20] McGehee, M. D., Heeger, A. *J. Adv. Mater*. 2000, 12, 1655-1668.

In: Crystals and Crystal Growth
Editor: Wilfred Carter
ISBN: 978-1-63463-791-6
© 2015 Nova Science Publishers, Inc.

Chapter 4

MODELING EFFECTS OF IMPURITIES ON CRYSTAL GROWTH

Issam A. Khaddour*
Faculty of Pharmacy, AlAndalus University,
AlQadmous, Tartus, Syria

ABSTRACT

This chapter represents specific review on the effects of impurities on the growth from solution. The concept of the impurity partition coefficient and its importance to the recrystallization processes is explained. Further, Kubota-Mullin model as adsorption model describing the effect of the shape, the size and the orientation of the impurity at the interface layer is reviewed, and discussed for the specific cases of sucrose grown from raffinose-doped solutions. Furthermore, benefiting of application of the 2D nucleation models, namely the birth and spread model, to understand the effects of impurities on the kinetics and the interfacial free energy of growth is also illustrated, and deeply discussed. Finally, a hypothetical approach is presented to enable evaluating the effect of macromolecular additives on the occurrence of needle-like crystals.

* Phone: +963 953389614, Email: issamoali99@gmail.com, P.O.Box: (297), Banias, Tartous, Syria.

1. INTRODUCTION

When crystallizing a particular solute from solvent, the presence of other dissolved solutes may profoundly affect the measured growth rates, or the observed crystalline habits, by adsorbing selectively on certain faces of the crystal. Even if foreign solutes are present at low concentrations, their effect may still significant to be considered as impurities [1]. The solvent from which the crystals are grown is, in the strictest sense, an impurity, as a change of the solvent frequently results in a change of crystal habit as well as the growth of different faces [2]. The selection of the solvent is important, because the nature of the solvent-solute interactions at the crystal surface greatly influences the equilibrium shape of the crystal. The crux of the matter is that a given crystallographic orientation on a crystal exposes a particular set of atoms of the solute molecule; therefore, different orientations have varying affinities for the solvent. These varying affinities impart different growth rates to the crystal faces and therefore influence the shape. To date there have been two different approaches to clarify the effect of a solvent on crystal growth and morphology. In one theory, favorable interactions between solute and solvent on specific faces lead to reduced interfacial free energy, causing transition from smooth to rough interface and concomitant faster surface growth. Alternatively, it has been proposed that preferential adsorption at specific faces will inhibit their growth as removal of bound solvent poses an additional energy barrier for continued growth [3, 4]. Consequently, when a growth is inhibited in a direction perpendicular to a given face, the area of this face is expected to increase in relation to the areas of the other faces of the same crystal.

Impurities can affect the solution structure changing by that the equilibrium concentration and hence the supersaturation. So, they alter the characteristics of the adsorption layer at the crystal-solution interface and influence the integration of growth units [5]. Further, impurities may adsorb at the kinks, at the steps, or at the ledges during the face growth. Then if the kink site adsorption is possible, growth retardation could be affected at relatively very low impurity concentrations in the solution. More impurity would be needed if the step site adsorption is the case, and higher impurity concentrations may be required if adsorption only occurs on a ledge or face site [6].

Furthermore, impurities (additives) can inherently be present in the crystallizing medium, or they are intentionally added. In the later it is usually named additives. Generally, additives (impurities) are divided into three categories: tailor-made additives, small-molecule additives, and

macromolecules. Tailor made-additive are ones that are structurally related, practically identical, to the solute molecule. Small molecule additives include surfactants and fatty acids, assuming that the crystallizing solute has a molecular weight of no more than 200 - 500 Daltons. A macromolecular additive or impurity could be a protein, polymer, or peptide.

The aim of this chapter is to provide some basics, guides, and notes on studying the effect impurities on crystallization kinetics for the growth from solution. So, the concept distribution coefficient of the impurity is explained and its importance is discussed. Further, two models describing the effects of impurities on crystal growth are presented, and their application on growth data, mainly for sucrose crystals, are shown and the results are discussed. Both terms additives and impurities will be interchangeably used in this chapter.

2. DISTRIBUTION COEFFICIENT OF IMPURITY

The term distribution coefficient is used to measure the degree of the incorporation of a certain impurity in the crystal. The equilibrium thermodynamic distribution coefficient K_0 (dimensionless) is usually defined as the ratio of concentration of impurity in the crystal divided by that in the solution [7].

$$K_0 = \frac{\gamma_{iL}}{\gamma_{iL}^{Sat}} \frac{c_{SL}^{Sat}}{c_{iL}^{Sat}} \frac{c_{iL}}{c_{SL}} exp\left(-\frac{\Delta H_{sol,iS}+T\Delta S_{therm,iL}}{R_G T}\right) \quad (1)$$

c_{iL} and c_{SL} are the actual concentration (in mole fraction) of impurity and solute in solution and c_{SL}^{Sat} and c_{iL}^{Sat} are the equilibrium (saturation) corresponding concentrations, γ_{iL}^{Sat} and γ_{iL} are the activity coefficients of the impurity at its equilibrium (solubility) and actual concentrations in the solutions corresponding to concentrations c_{iL} and c_{iL}^{Sat}, respectively, R_G (J/mol K) is the universal gas constant, T (K) is the absolute temperature, $\Delta H_{sol,iS}$ (J/mol) is the heat of solution of the impurity in the solid state, and $\Delta S_{therm,iL}$ (J/mol) is the change in the thermal entropy of the impurity caused by its transfer from the solution to the crystal. For $K_0 < 1$, the crystal–medium interface serves as a filter to impurity particles, and performing the recrystallization process will result in improvement in the purity of the crystalline product. But, when $K_0 = 1$ the material will not be purified by repeated crystallizations. For $K_0 > 1$, the impurity concentrates in the crystal.

In this regard, it is found that the structural similarity between the solute unit and the impurity unit enhances the incorporation of the impurity into the crystal, so increasing the distribution coefficient value [8]. However, lower quality and smaller crystals will be produced when $K_0 < 1$, as the impurity is accumulates at interface. On the other hand, crystals of better quality and larger sizes will be expected for the cases when $K_0>1$ [7].

Sound measurement of incorporation of impurities requires estimation of the effective segregation coefficient K_{eff}, which is the ratio of impurity concentration in the crystal to its average concentration at the crystal-medium interface. Hall [9] and Burton et al. [10] proposed some forms for the K_{eff} as function of the normal growth rate R (m/s) for the case of growth from melt. Regarding that the volume diffusion is controlling the growth rate, Burton et al. [10] suggested the following form to estimate the value of K_{eff}

$$K_{eff} = \frac{K_0}{K_0+(1-K_0)\exp(-R\delta/D)} \quad (2)$$

D (m^2/s) is the diffusion coefficient of the impurity species, and δ (m) is the boundary layer thickness. The model is based upon the assumption of increased concentration of the impurity molecules in the boundary layer around the growing crystal due to partial rejection of impurities. Further, the model predicts extremely highly purified (in essence 100% purity) crystals at vanishing or very slow growth rates [11]. Although, this model was not found to be particularly applicable to growth from solution;1 Promraksa et al. [12] used equation (2) to measure the dextran partition coefficient for sucrose crystallization in presence of 1:1 mixtures of two molecular fractions of dextran (75 and 250 kDa), with variable concentrations (1000 and 2000 ppm/Brix), and at different temperatures (30,40,50 ºC). They found that the effective partition coefficient of dextran, at 30 ºC and variable supersaturations (σ), is almost constant and equal to ≈ 0.02, see Figure 1. However, 4 - 5 times higher values for the effective partition coefficient of dextran, from sucrose growth at 40 and 50 ºC, were respectively reported at the same supersaturations. It is worth to mention that the increase of the dextran concentration from 1000 to 2000 ppm/Brix did not show remarkable change in the effective distribution coefficient. They also found that the effectiveness of the dextran mixture increases with increase of the growth rate of sucrose. As conclusion, it could be beneficial to recrystallize sucrose to purify it from similar fractions of the dextran being incorporated in the sucrose crystals, but at very slow growth rates.

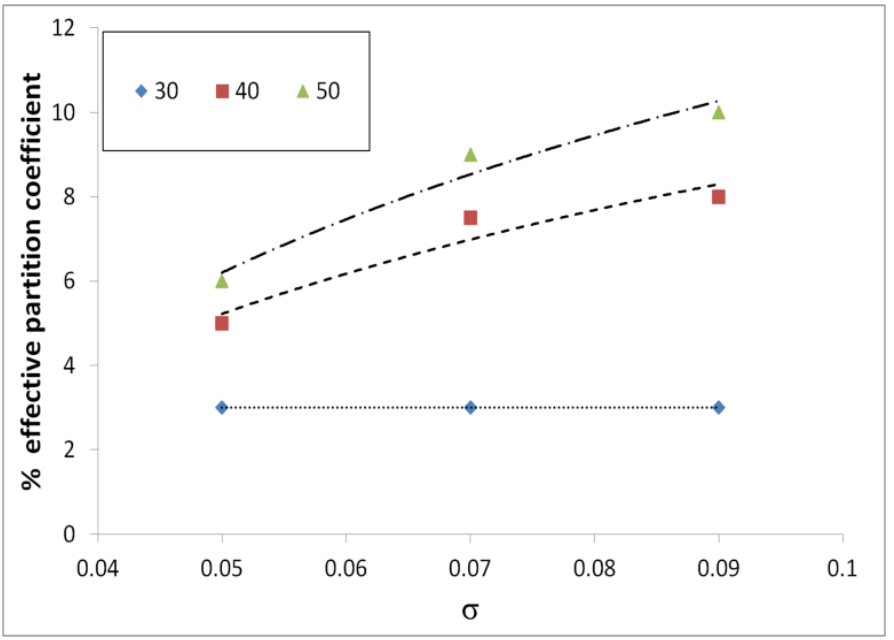

Figure 1. Illustrative chart of the partition coefficient for dextran in sucrose crystallization at different temperatures (30, 40, 50 ºC), represented as function of relative supersaturation. Adopted from Promraksa et al. [12]

3. Modeling Impurity Effects

An impurity is considered immobile when it exerts a pinning mechanism of the face growth, whereby the progress of the growth layers on a crystal surface is blocked by individually adsorbed impurity species [13]. Actually the term immobile impurity is relative; more specifically, the additive must have an adsorption lifetime much longer than the characteristic time for surface growth [4]. A complete stoppage of growth would occur when the surface distance between the adsorbed impurity species l (m) is less than $2\rho_c$, where ρ_c (m) is the radius of a 2D critical nucleus:

$$\rho_c = \frac{\gamma d}{k_B T \ln(1+\sigma)} \tag{3}$$

γ (J/m^2) denotes the solid-liquid interfacial free energy, d (m) is the size of the growth unit, k_B (J/K) is the Boltzmann constant. For a spaced distance

$l > 2\rho_c$ that step would pass between the impurity units, however, because of its curvature, it is expected to continue to grow at lower rate than without any impurity present, see Figure 2 [13].

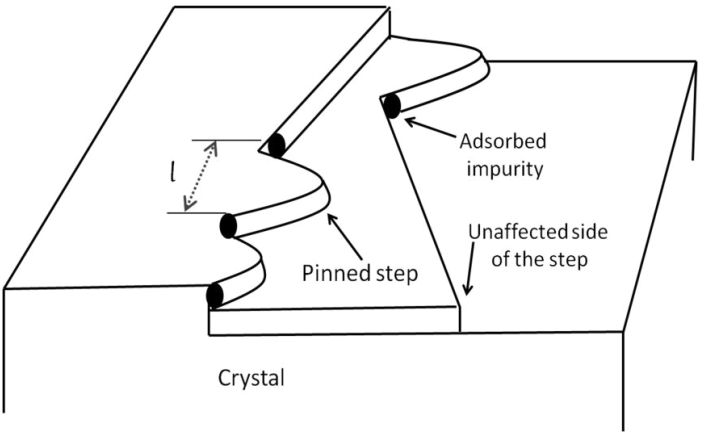

Figure 2. Schematic illustration of the retardation effect of the surface-adsorbed impurities on the advancement of the steps.

3.1. Kubota-Mullin Model

The early mathematical version of this model assumes that the blockage of the surface active sites, i.e., kink sites, by impurities is related to the impurity concentration in solution through Langmuir adsorption isotherm [14, 15]. Further improvement to this approach included the addition of the impurity effectiveness factor α_{eff}, which is used to relate the lateral growth velocity in the presence of an impurity v_i (m/s) to its counterpart for the growth from pure solution v (m/s) [16],

$$v_i/v = 1 - \alpha_{eff}\theta_{eq} \tag{4}$$

where θ_{eq} is the fractional surface coverage by the adsorbed impurity at equilibrium, and it is determined applying Langmuir isotherm as follows

$$\theta_{eq} = K_L c_i/(1 + K_L c_i) \tag{5}$$

where c_i (mole fraction) denotes the concentration of the impurity in the solution and K_L (dimensionless) is Langmuir constant. If the linear growth rates R_i (m/s), from impure solution, and R (m/s), from pure solution, are proportional to the corresponding lateral growth velocities, then

$$R_i/R = 1 - \alpha_{eff} K_L c_i/(1 + K_L c_i) \tag{6}$$

Thus, when $\alpha_{eff} = 1$, and $\theta_{eq} = 1$, results $R_i = 0$. However, when $\alpha_{eff} > 1$ and $\theta_{eq} < 1$ then $R_i \to 0$, but when $\alpha_{eff} < 1$ the growth rate R_i never approaches zero even for $\theta_{eq} = 1$.

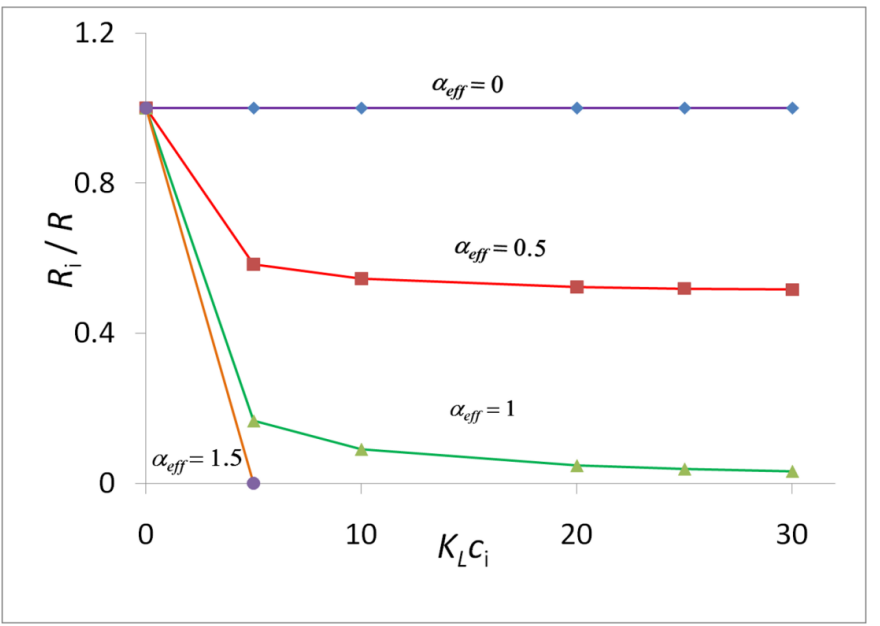

Figure 3. Relationships between the relative growth rate and the dimensionless impurity concentration $K_L c_i$ for different values of the impurity effectiveness factor α_{eff}. [17]

Figure 3 depicts the dependence of the relative growth rate R_i/R_L on the dimensionless impurity concentration $K_L c_i$ at different values of the effectiveness factor. When $\alpha_{eff} > 1$, the relative growth rate decreases very rapidly with increasing $K_L c_i$, reaching zero at very small values of $K_L c_i$. For $\alpha_{eff} = 1$, $R_i/R_L \to 0$ asymptotically.

When adsorption of impurity occurs at kinks, the linear coverage of the kink sites along the advancing steps by the adsorbed impurity units θ_l is equal to the fractional coverage of the surface θ_{eq}, and may be expressed in the form [7]

$$\theta_l = \lambda_o / l \tag{7}$$

where λ_o (m) is the average distance between the kink sites along the advancing step [4, 18]. The equivalent expression of Equation (6) is given as [19]

$$R_i / R = 1 - \rho_c / l \tag{8}$$

Then the effectiveness factor can be presented in the form [5]

$$\alpha_{eff} = \gamma d / k_B T \ln(1 + \sigma) l \tag{9}$$

The introduction of the effectiveness factor enables evaluating the growth suppression characteristics of an impurity which are expected to depend on the size, shape, or orientation of the impurity molecules (a stereochemical effect) [20]. Equation (9) contains several variables where the solid-liquid interfacial free energy of the 2D nucleation is the most important. This variable is mainly related to the orientation, but also affected by the shape, size of the additive molecule, the temperature and the supersaturation degree [21-23].

Further, differential heat of adsorption Q_{diff} (J/mol) can be estimated after the knowledge of the value of the Langmuir constant using the equation [7]:

$$K_L = exp\left(Q_{diff} / R_G T\right) \tag{10}$$

In general, Q_{diff}, for a certain material, decreases steadily with increasing of the adsorbed amount [24]. However, development of Kubota-Mullin model was carried out on the basis of the Langmuir adsorption isotherm, where the differential heat of adsorption Q_{diff} does not depend on the surface coverage [7].

The author applied this model to estimate the influence of raffinose, as added impurity, on the advancement of the steps in the direction [010] at the face (100) for data published by Albon and Dunning [25], see Figure 4.

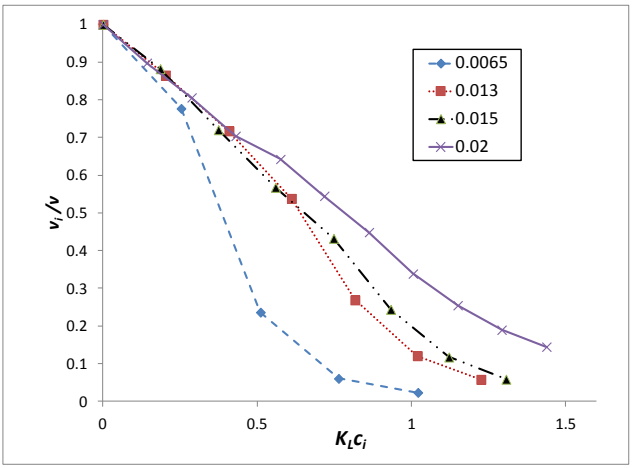

Figure 4. Relative step velocity on the [010] direction at the face (100) of the sucrose crystals grown in presence of variable concentrations of raffinose at different supersaturations, and at 30 ºC.

Table 1. Effectiveness factor, Langmuir constant, differential heat of adsorption and the maximum surface coverage ratio of raffinose obtained applying of Kubota-Mullin model for sucrose growth at different supersaturations and at 30 ºC

Parameter	Relative supersaturation			
	0.0065	0.013	0.015	0.02
α_{eff}	2	1.5	1.45	1.3
K_L	443.8	355.1	325	232.7
Q_{diff}	15.4	14.8	14.6	13.7
θ_{eq}(max.)	0.51	0.56	0.57	0.57

Estimation of the effectiveness factors and the corresponding Langmuir constants, presented in Table 1, is performed using Solver in Excel application. Table 1 shows higher step-advancement retardation effect of raffinose at lower supersaturations. α_{eff} is reduced by 25% when supersaturation is doubled. Results indicate that raffinose shows the effects of strong adsorbing impurity which effectively retards the growth rate at relatively low concentrations.

Further, Sgualdino et al. [26] tested growth kinetics of (110), $(10\bar{1})$, (100) and $(\bar{1}\bar{1}0)$ as the four most important F (flat) forms of sucrose crystal grown from pure solutions and from raffinose doped solutions. They found, applying

Kubota-Mullin model, that raffinose strongly hinders the growth rates of the forms (110), $(10\bar{1})$, (100) and $(\bar{1}\bar{1}0)$, and the effects increases with increasing of added concentrations of raffinose, see Figure 5. Hence raffinose can markedly affect the growth kinetics through the reduction of the density of kinks available to the incorporation of the incoming sucrose molecules. However, the effect on mobility reduction of step ledges due to the raffinose molecules firmly incorporated on the surface terraces cannot be neglected. The author believes that existence of a threshold concentration of raffinose ($\approx 3\%$) for its effect on the growth of the form $(\bar{1}\bar{1}0)$ can be due to the relatively high adsorption energy of raffinose on this face, and/or due to that the retarding effect of growth of raffinose on this face occurs only by adsorption at terraces, but for other faces the adsorption occurs mainly at kink sites. Fitting the data to Kubota-Mullin and Cabrera Vermilyea models shows that the resulted curves from both models are overlapping at the late stages of growth and a distinct discrepancy appear between these curves in the early stage of growth. However, Kubota Mullin model represented better the data than Cabrera Vermilyea model. So indicating that raffinose adsorbs mainly at the kink sites in the early stages of growth, but the later adsorption (second part of the growth curves) occurs at kinks and terraces simulataneously, and mostly at similar probabilities. The author belives that, when the retarding effect of raffinose is driven by kinks-adsorbed impurity mechanism, the growth inhibition effect takes place through changes in the step structure; thereafter a dramatic increase in the interfacial free energy will result in.

As the solution of the Kubota Mullin model is numerical, so the change of the initially proposed limits of the targeted variables, i.e., K_L and α_{eff}, will affect the values obtained by the numerical solution. So, the solution is only valid in its relative sense, but proper to explain the data. However, the values of the real parameters can be different from the ones obtained by numerical solutions. In this course, Sgualdino et al. [26] pointed out a contradiction between their value for K_L from at 40 ºC, and the one obtained by Kubota [20] at 30 ºC from analyzing Albon and Dunning data. Their interpretation includes that the adsorption process is an exothermic process, so they expected lower values of K_L at 40 ºC than at 30 ºC, but the opposite occurred. The above-mentioned analysis by the author, for the same data from Albon and Dunning [25] work, shows further discrepancy with both estimations of the K_L by Sgualdino et al. [26] and Kubota [20], where lower K_L values than those presented by Kubota are found, and much lower effectiveness factors were also estimated, see Table 1. Again the author believes that the reason lies in

the applied numerical method for estimating the K_L and α_{eff}. For example the author found that the different and the repeated trials, for obtaining a solution by Solver, to be insensitive to a very wide ranges of K_L. In other words, when α_{eff} is set in advance at certain value, then changes of hundred thousand or million in K_L values will not result any change of the set initial value of α_{eff}. In fact, such insensitivity can be understood from Equation (10), where K_L values follow exponentially the changes in the Q_{diff}. So, small changes in the heat of adsorption dQ_{diff} result in big variations ΔK_L in the Langmuir constant.

Furthermore, and similarly to Black et al. [15], Sgualdino et al. [26] proposed that the growth of the (100) faces of the sucrose crystal, in presence of raffinose, is selectively inhibited, because this corresponds to a molecular orientation in which raffinose can sit with its fructose component on the surface, and the galactose unit projecting out of the surface to inhibit subsequent growth.

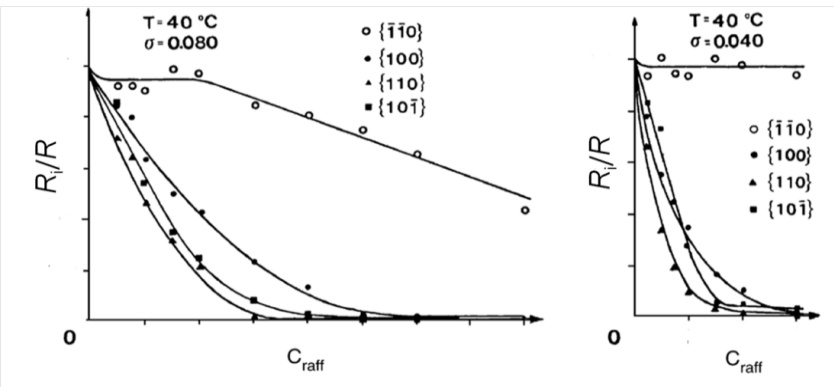

Figure 5. Schematic representation of relative growth rates of four forms of the sucrose crystal in presence of variable concentrations of raffinose at two different relative supersaturations (left: σ = 0.08, and right σ = 0.04) and temperature of 40 ºC [26].

3.2. Birth and Spread Model

This model allows for both nucleation and subsequent step advancement at a finite rate. Figure 6 shows the surface pattern of face (100) of the sucrose crystal grown from pure solutions, where multiple nucleation and subsequent spread are depicted [27].

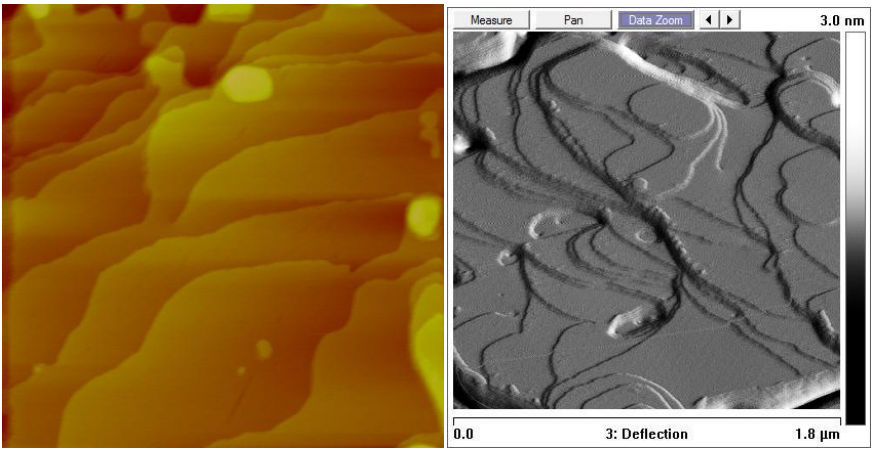

Figure 6. Atomic force microscopy images showing the occurrence of multiple 2D nucleation events for the growth of the face (100) of the sucrose crystal.

In effect, birth and spread model was developed to evaluate growth from pure solutions, where multiple 2D nucleation mechanism is expected to dominate. However, Khaddour et al. [21] applied birth and spread model to evaluate growth kinetics of sucrose in presence of variable concentrations of different molecular fractions of dextran at 40 and 50 ℃, respectively. In this regard, the found dead supersaturation zones, see example in Figure 7, can be safely ignored as these are mainly a property of the face growth rate, and not for the overall growth rate, even when tailor-made additives are used at high concentrations. Further, the found dead zones, for pure and impure solutions can be a time dependent parameters; for that it is neglected in the application of birth and spread model for the impure systems. At 40 ℃, the various dextran fractions caused slight enhancing effects of the overall normal growth rates of sucrose. Such general enhancing effect was understood from applying birth and spread model. The application of the birth and spread model is carried out using Equation (11),

$$R = C_4\sigma^{2/3}[\ln(1+\sigma)]^{1/6}exp\left[-C_2/3T^2\ln(1+\sigma)\right] \tag{11}$$

where C_4 (m/s) is a constant given by

$$C_4 = 2h^{1/6}{v_m}^{5/6}(\omega/\pi)^{1/3}(n_1 D_S\beta\gamma_o C_{SE}/x_S)^{2/3} \tag{12}$$

where v_m (m^3) is the volume of the growth unit, ω (m/s) is the average speed of the surface adsorbed molecules, D_S (m^2/s) is the surface diffusion coefficient of the adsorbed molecule, β and γ_o are the step and kink retardation factors, respectively, and C_{SE} (m^{-2}) is the equilibrium concentration of the solute on the surface. x_s (m) is the mean diffusion distance of the solute on the surface during time τ_s (s), $x_S^2 \cong bD_S\tau_s$, where b is a constant that varies from 2, 4 and 6 for one-, two-, or three-dimensional diffusion.

Application of birth and spread model is to be done by graphing $\ln\left[\left(\frac{R}{\sigma^{2/3}[\ln(1+\sigma)]^{1/6}}\right)\right]$ versus $\left(\frac{1}{3T^2\ln(1+\sigma)}\right)$, see equation (11). The interfacial free energy between the supersaturated solution and the crystal surface is then estimated using equation (13), where C_2 values are determined from the slope of the obtained equations from the fitting by linear regression type. Finally, the values of the kinetic coefficient C_4 is determined from the corresponding intercept, see Figure 8.

$$C_2 = \pi h v_m \gamma^2 / k_B^2 \tag{13}$$

Table 2 shows that the different fractions of dextran, at 40 ℃, enhanced the overall linear growth rates of sucrose, in comparison with the pure system, through causing about 20% reduction to the interfacial free energy of that for the pure system. Khaddour et al. [21] suggested that the lower interfacial free energies in the case of sucrose crystals grown from dextran-doped solutions, at 40 ℃, is due to the hydrocarbon parts of the glucose moieties of the dextran molecule, i.e., they project outwards from the dextran-targeted faces of the crystal, so, reducing the value of the interfacial free energy, see Figure 9. In other words, such orientation achieves the maximum mutual interaction energy between molecules at the interface [24, 28-30]. In fact, this assumption is very logical as if the hydroxyl groups will be projecting outwards from the dextran-targeted faces, they will enhance the solubility of sucrose by contributing formation of stronger hydrogen bonding net at the interface layer, then reducing the crystallization rate. Further, van Enckervort and van den Berg [31] reported that when the interaction between the immobile impurity and the growth units is exceeding the bond energy between adjacent growth units, the impurities will promote rather than decrease the growth rate. Dextrans are macromolecules; as a result they mostly act like immobile impurities. So, the hypothesis of van Enckervort and van den Berg can be other aspect of the case of sucrose growth in the presence of different dextrans at 40 ℃. This assumption is also supported by the structural similarity between the dextran

and the sucrose, i.e., dextran and sucrose molecules contain glucose units in their structures.

On the other hand, sharp decrease in the growth rate of sucrose, at 50^{o}C, was occurred for the run at concentration of dextran (dextran fraction of 70 kDa) of 3.85 g/L of water in comparison with the run of the pure system, and with the run of dextran concentration of 1.28 g/L of water. Practically the same interfacial free energy is found for the runs with dextran concentrations of 1.28 and 3.85 g/L of water, so what determines the growth rate for the later run is the kinetic coefficient which is equal to 2.1×10^{-7}m/s, and it represents less than half of the value of the kinetic coefficient for the pure system run, and about 60 % of the kinetic coefficient of the run performed with dextran concentration of 1.28 g/L of water, see Table 2. Further, in the case of sucrose growth in presence of the dextran fractions 250000 and 2000000, it is found that the growth of sucrose is controlled by kinetic coefficients rather than by the interfacial free energy effect.

Similarly Kumar [32] studied the effect of non-ionic surfactant, Hodag CB6, on the growth kinetics of sucrose crystals at 30 and 50^{o}C. It is found that the added impurity increases the growth rate with increase in impurity concentration, see Figure 10. Growth data were analyzed using birth and spread model, and the results showed that the interfacial free energy of growth decreases with increasing of the impurity concentration. So, imparting a promoting effect on the growth rate of sucrose. In other words, the added surfactant decreases the solubility of sucrose in the mixture. BCF model poorly represents the data well at 50 ^{o}C, but poorly at 30 ^{o}C. However, Sgualdino et al. [26] reported that screw dislocation mechanism is dominating the growth at the faces $(10\bar{1})$, (100) and $(\bar{1}\bar{1}0)$, so the kinetics of growth of these faces is well described by the BCF model. Similarly, Valčić [33] found a good agreement of his experimental results on sucrose growth from pure solutions, at 30^{o}C, with the BCF surface diffusion model. Plausible reasoning of this discrepancy is that Kumar applied the BCF model to data represent the overall linear growth rate, and the other authors applied it to the growth of specific faces.

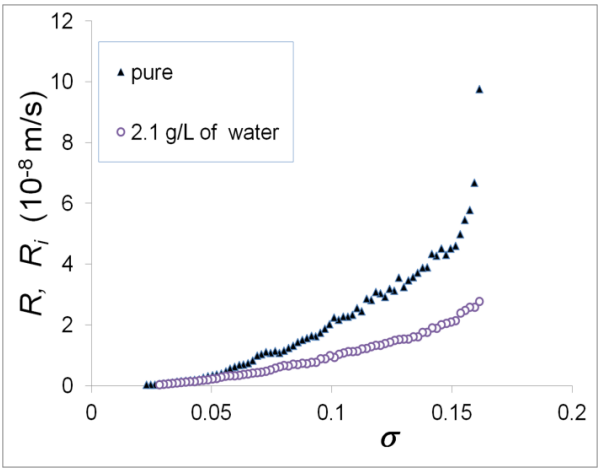

Figure 7. Occurrence od dead supersaturation zone during growth of sucrose from pure solutions and in presence of dextran at 50 ºC [21].

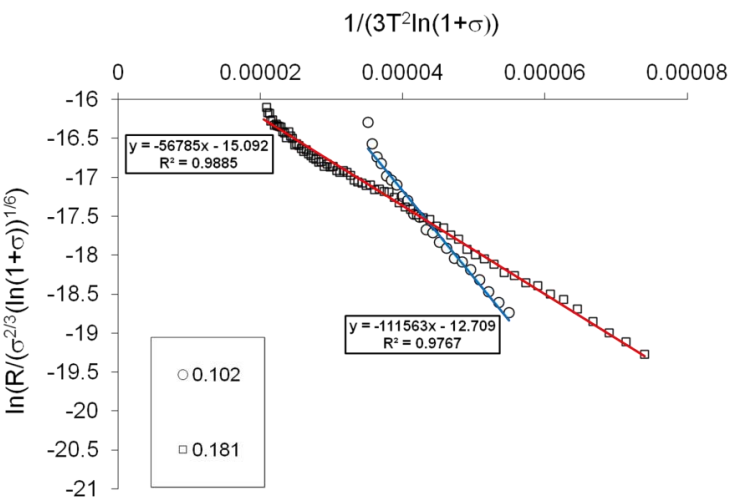

Figure 8. Examples of application of birth and spread model for sucrose growth from starting from two different initial supersaturations (0.102 and 0.181), where linear regression enables estimating the values of C_2 and C_4.

Table 2. Interfacial free energies γ and the kinetic coefficients C_4 of the growth of sucrose, at 40 and 50 ℃, from pure solutions and in the presence of different concentrations of the three used molecular weight fractions of dextran [21]

Run	40 ℃			50℃		
	Dextran g/L of water	$\gamma(10^{-3}$ J/m$^2)$	$C_4(10^{-7}$ m/s)	Dextran g/L of water	$\gamma(10^{-3}$ J/m$^2)$	$C_4(10^{-7}$ m/s)
Pure system	0	5.1	3.7	0	3.6	4.5
Dextran fraction (kDa)						
70	1.28	4.3	2.5	1.28	3.9	5.1
	3.85	4.2	2.5	3.85	4.0	2.1
	7.71	4.1	2.5	7.71	3.6	1.8
250	1.28	4.0	2.2	1.28	3.6	4.2
	3.85	4.1	2.3	3.85	3.4	3.8
	7.71	3.9	2.3	7.71	3.6	4.0
2000	1.28	4.0	2.5	1.28	4.0	2.3
	3.85	4.1	2.6	2.1	3.2	1.7
	7.71	4.1	2.6	3.85	-	-

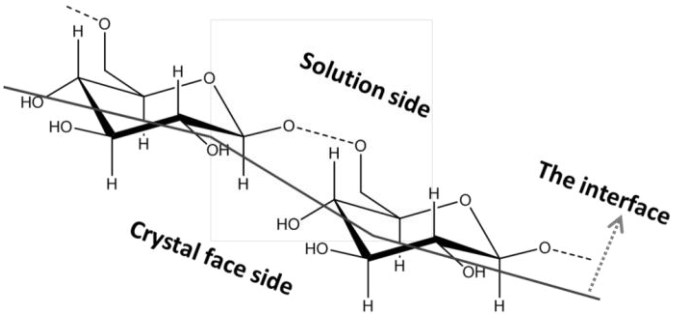

Figure 9. Hydrocarbon parts of glucose units of the dextran molecule projecting outwards, to the solution side, of a face-adsorbing dextran of a growing sucrose crystal.

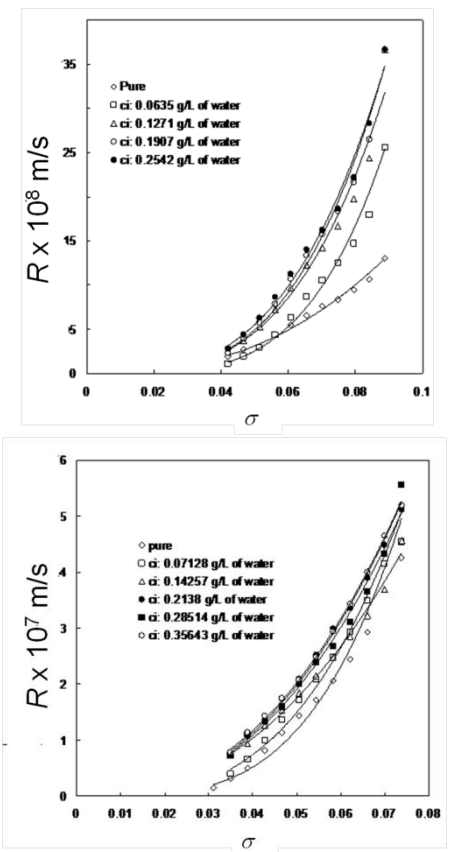

Figure 10. Plots of linear growth rate versus supersaturation ratio for different impurity concentrations: (top) at 30 ^{o}C and (down) at 50^{o}C, with permission from the author.

4. CRYSTAL ELONGATION DUE TO MACROMOLECULES ADDITIVES

Considering that the face-specific adsorption of a macromolecule additive results in anisotropic spread of steps across the targeted face, thinner (elongated) crystals than could be predicted on the basis of the proportionality between the face growth rate and the attachment energy of a face slice will be produced. Further, the degree of supersaturation is expected to be lowered at the surface points of the incorporation of the additive [34, 35], which decreases the incorporation of the solute molecules in directions normal to the alignment of the adsorbed macromolecule on the surface. In other words, the maximum interaction energy of orientation of the incorporating solute molecule is not achieved, which directs the growth to other directions to satisfy the higher interaction energy condition.

Further, and considering that the growth is limited to the direct integration mechanism, the impinge rate at which the sucrose molecules impinge a square array of the face of the crystal can be given by the relation

$$K_+ = f_v exp(\Delta\mu/k_B T) \tag{14}$$

where f_v is an overall frequency factor has the same unity of K_+ and includes any retardation of the attachment, $\Delta\mu$ (J) is the chemical potential difference at the interface from the crystal–fluid equilibrium value. The dissolution of the surface solute molecules occurs at rate K_- that depends on the coordination, [36]

$$K_- = f_v \exp(-n\phi/k_B T) \tag{15}$$

n denotes the number of the nearest neighbours of the solute molecules and ϕ (J) is the bond energy between pair of such neighbours. So, the ratio K_+/K_- is given by

$$K_+/K_- = exp((\Delta\mu + n\emptyset)/k_B T) \tag{16}$$

and can be used to evaluate the relative importance of the attachment and the detachment fluxes.

When the solute molecule is attempting to be added in the vicinity of the alignment of the macromolecule on a macromolecule-targeted face, and in

direction perpendicular to the alignment of the macromolecule, lower interaction energy ϕ and less number of neighbours at reduced chemical potential will prevail, so reducing the growth rate at this direction.

This theoretical discussion applies only for the case where the macromolecule has a reducing effect on the growth rate, or when it noticeably modifies the morphology of the growing crystal along the crystallographic direction parallel to the direction of the macromolecule alignment at the adsorption-targeted face, that in comparison with similar crystal grown from pure system.

CONCLUSION

The development in crystal growth science enabled crystal engineers to supervise and control, in very intelligent way, the quality and the properties of their final products. The term “additives” rather than the term “impurities” is being in use nowadays. So, the addition of certain additive can alter the shape of the crystal, increase or decrease the number of the crystal faces. Both growth retarding or enhancing effects of the additives provide powerful tools to better engineered crystals depending on their applications.

This chapter went beyond the scene trying to characterize the kinetics of the growth process in presence of additives. Effectiveness factor introduced in Kubota-Mullin model represents necessary measure to evaluate the impact of the interfacial free energy of growth at constant supersaturations. Both of studied additives, raffinose and dextran, in this chapter belong to the tailor-made class. Raffinose effects on the concerned faces of sucrose appear to be driven by the interfacial free energy parameter. However, dextran effects were interfacial free energy dependent in one case, and dependent on the kinetic coefficient in the other case. These findings enabled the development of theoretical interpretation of the formation of needle-like sucrose crystals in presence of macromolecules like dextran, as example.

REFERENCES

[1] Ohara, M.; Reid, R. C., *Modeling Crystal Growth Rates from Solurtion* ed.; Prentice-Hall Inc.: New Jersey, 1973.

[2] Davey, R. J.; Mullin, J. W.; Whiting, M. J. L., Habit modification of succinic acid crystals grown from different solvents. *Journal of Crystal Growth* 1982, 58, (2), 304-312.

[3] Weissbuch, I.; Popovitz-Biro, R.; Lahav, M.; Leiserowitz, L., Understanding and control of nucleation, growth, habit, dissolution and structure of two- and three-dimensional crystals using `tailor-made' auxiliaries. *Acta Cryst.* 1995, B51, 115-148.

[4] Lovette, M. A.; Browning, A. R.; Griffin, D. W.; Sizemore, J. P.; Snyder, R. C.; Doherty, M. F., Crystal Shape Engineering. *Industrial & Engineering Chemistry Research* 2008, 47, (24), 9812-9833.

[5] Mullin, J. W., *Crystallization*. 4th ed.; Butterworth-Heinemann: Oxford, 2001.

[6] Davey, R. J., The effect of impurity adsorption on the kinetics of crystal growth from solution. *Journal of Crystal Growth* 1976, 34, 109-119.

[7] Sangwal, K., *Additives and Crystallization Processes*. ed.; John Wiley & Sons: Chichester, 2007.

[8] Sgualdino, G.; Aquilano, D.; Tamburini, E.; Vaccari, G.; Mantovani, G., On the relations between morphological and structural modifications in sucrose crystals grown in the presence of tailor-made additives: effects of mono- and oligosaccharides. *Materials Chemistry and Physics* 2000, 66, (2-3), 316-322.

[9] Hall, R. N., Segregation of impurities during the growth of germanium and silicon crystals *Journal of Physical Chemistry* 1953, 57, 936-839.

[10] Burton, J. A.; Prim, R. C.; Slichter, W. P., The distribution of solute in crystals grown from the melt. *Journal of Chemical Physics* 1953, 21, 1987-1991.

[11] Mersmann, A., Quality of Crystalline Products. In *Crystallization Technology Handbook*, 2nd ed, ed.; Mersmann, A., Ed. Marcel Dekker: New York, 2001.

[12] Promraksa, A.; Flood, A. E.; Schneider, P. A., Measurement and analysis of the dextran partition coefficient in sucrose crystallization. *Journal of Crystal Growth* 2009, 311, (14), 3667-3673.

[13] Cabrera, N.; Vermilyea, D., The Growth of Crystals from Solution. In *Growth and Perfection of Crystals*, Doremus, R.; Roberts, B.; Turnbull, D., Eds. Wiley & Sons: New York, 1958.

[14] Davey, R. J.; Mullin, J. W., Growth of the faces of ammonium dihydrogen phosphate crystals in the presence of ionic species. *Journal of Crystal Growth* 1974, 23, (2), 89-94.

[15] Black, S. N.; Davey, R. J.; Halcrow, M., The kinetics of crystal growth in the presence of tailor-made additives. *Journal of Crystal Growth* 1986, 79, (1-3, Part 2), 765-774.

[16] Kubota, N.; Mullin, J. W., A kinetic model for crystal growth from aqueous solution in the presence of impurity. *Journal of Crystal Growth* 1995, 152, (3), 203-208.

[17] Khaddour, I. Crystallization of sucrose from pure solutions and in teh presence of dextran of different molecular weights. Porto Univ. Porto, 2011.

[18] Vekilov, P. G.; Feeling-Taylor, A. R.; Yau, S.-T.; Petsev, D., Solvent entropy contribution to the free energy of protein crystallization. *Acta Cryst.* 2002, D58, 1611-1616.

[19] Kubota, N.; Yokota, M.; Mullin, J. W., The combined influence of supersaturation and impurity concentration on crystal growth. *Journal of Crystal Growth* 2000, 212, (3-4), 480-488.

[20] Kubota, N., Effect of Impurities on the Growth Kinetics of Crystals. *Crystal Research and Technology* 2001, 36, (8-10), 749-769.

[21] Khaddour, I.; Ferreira, A.; Bento, L.; Rocha, F., Sucrose crystal growth in the presence of dextran of different molecular weights. *Journal of Crystal Growth* 2012, 355, (1), 17 - 25.

[22] Khaddour, I.; Rocha, F., Metastable zone width for secondary nucleation and secondary nucleation inside the metastable zone. *Cryst. Res. Tech.* 2011, 46, 373-382.

[23] Khaddour, I. A.; Bento, L. S. M.; Ferreira, A. M. A.; Rocha, F. A. N., Kinetics and thermodynamics of sucrose crystallization from pure solution at different initial supersaturations. *Surface Science* 2010, 604, (13-14), 1208-1214.

[24] Adamson, A. W.; Gast, A. P., *Physical Chemistry of Surfaces* 6th ed.; Wiley Interscience: New York 1997.

[25] Albon, N.; Dunning, W. J., Growth of sucrose crystals: determination of edge energy from the effect of added impurity on rate of step advance. *Acta Crystallographica* 1962, 15, (5), 474-476.

[26] Sgualdino, G.; Aquilano, D.; Cincotti, A.; Pastero, L.; Vaccari, G., Face-by-face growth of sucrose crystals from aqueous solutions in the presence of raffinose. I. Experiments and kinetic-adsorption model. *Journal of Crystal Growth* 2006, 292, (1), 92-103.

[27] Khaddour, I., Unpublished data. 2010.
[28] Langmuir, I. In *Colloid Symposium Monograph*, The Chemical Catalog Company: New York 1925; p 48.
[29] Hardy, W. B., The Influence of Chemical Constitution upon Interfacial Tension. *Proc. Roy. Soc. London* 1913, 88, 303-313.
[30] Hakins, W. D., *The Physical Chemistry of Surface Films*. ed.; Reinhold: New York, 1952.
[31] van Enckevort, W. J. P.; van den Berg, A. C. J. F., Impurity blocking of crystal growth: a Monte Carlo study. *Journal of Crystal Growth* 1998, 183, (3), 441-455.
[32] Vasanth Kumar, K., Transfer of impurities into crystals in industrial processes: mechanisms and kinetics, (Doctoral Thesis), Chemical Engineering Department, Porto University, Porto, 2010.
[33] Valcic, A. V., The influence of dislocations on the growth rate of saccharose crystals, *Journal of Crystal Growth* 1975, 30 (1), 129-136. DOI: 10.1016/0022-0248(75)90212-2.
[34] Malkin, A. J.; Kuznetsov, Y. G.; McPherson, A., Defect Structure of Macromolecular Crystals. *Journal of Structural Biology* 1996, 117, (2), 124-137.
[35] van Hoof, P. J. C. M.; Grimbergen, R. F. P.; Meekes, H.; van Enckevort, W. J. P.; Bennema, P., Morphology of orthorhombic n-paraffin crystals: a comparison between theory and experiments. *Journal of Crystal Growth* 1998, 191, (4), 861-872.
[36] Gilmer, G. H., Simulation of 2D nucleation and crystal growth. *Faraday Symposia of the Chemical Society* 1977, 12, 59-69.

INDEX

A

absorption spectra, 59, 60
academic motivation, 54
acid, 9, 90
active site, 76
actuators, vii, 1
additives, ix, 71, 72, 73, 82, 89, 90, 91
adsorption, ix, 71, 72, 75, 76, 78, 79, 80, 89, 90, 91
advancement, 76, 78, 79, 81
AFM, viii, 53, 55, 56, 57, 58, 66
alkali niobates, vii, 2
alters, 11
ammonium, 91
amplitude, 31
aqueous solutions, 3, 4, 91
atmospheric pressure, 16
atomic force, viii, 53, 55
atoms, 9, 13, 17, 26, 30, 34, 40, 42, 47, 72
attachment, 36, 41, 88

B

base, 17
bending, 39, 44, 46
benefits, 11
Boltzmann constant, 75
bonding, 83
bonds, 9, 36, 41, 42, 44
borate crystals, viii, 25, 26
borate melt structures, viii, 25, 27, 30, 31
boundary layer, viii, 25, 27, 28, 37, 40, 47, 74
Brazil, 13
breathing, 34, 39, 44, 46
bulk crystals, vii, 1

C

candidates, vii, 2, 54, 55
carbides, 3
cation, 16
chemical(s), vii, viii, 2, 3, 4, 6, 7, 9, 11, 25, 88, 89
chemical reactions, 3
chemical stability, 3, 11
China, 25, 47, 48, 53
cleaning, 19
clusters, 26, 31
color, viii, 53, 56, 60, 61, 66
commercial, 31
complexity, viii, 25, 30
composition, 5, 11, 15, 20, 22
compounds, 2, 4, 5, 6, 16, 19, 30, 47
compressibility, 6
compression, 13
computer, 17, 21
configuration, 30, 59
constituents, 7

Constitution, 92
contradiction, 80
cooling, 2, 9, 27
coordination, 16, 26, 88
correlation, 31
corrosion, 3, 11
cost, 13
cracks, 9, 11, 20
crystal growth, vii, viii, 1, 2, 3, 5, 7, 8, 9, 10, 11, 15, 16, 17, 18, 19, 20, 22, 25, 27, 28, 30, 32, 37, 40, 41, 42, 47, 55, 63, 66, 72, 73, 89, 90, 91, 92
crystal growth processes, vii
crystal growth systems, viii, 25, 28, 32, 47
crystal quality, 13
crystal structure, viii, 9, 26, 27, 33, 36, 41, 47
crystal surface, viii, 37, 53, 57, 58, 59, 72, 75, 83
crystalline, viii, 2, 9, 11, 19, 30, 32, 53, 60, 72, 73
crystallization, 2, 7, 73, 74, 75, 83, 90, 91
crystallization kinetics, 73
crystals, vii, viii, ix, 1, 3, 7, 8, 9, 11, 13, 15, 16, 17, 18, 20, 21, 22, 25, 26, 32, 37, 38, 40, 47, 53, 54, 55, 56, 57, 58, 59, 60, 61, 62, 63, 64, 65, 66, 67, 71, 72, 73, 74, 79, 83, 84, 88, 89, 90, 91, 92

D

decay, 63, 64, 65, 66
decomposition, 2, 3
defects, 11, 27
density functional theory (DFT), viii, 26, 31, 32, 44, 45, 47
deposition, 5, 7, 19
depth, 55
detachment, 88
detection, 44
diaphragm, 8
dielectric constant, 6
dielectric permittivity, 31
diffraction, 28, 57
diffusion, 6, 74, 83, 84
digital cameras, vii, 1
diodes, ix, 54, 56, 67
dislocation, 84
displacement, 31
dissociation, 6
distribution, 20, 73, 74, 90
diversity, 26, 30
DOI, 92
doping, viii, 53, 55, 58, 60, 61, 65, 66

E

electric charge, 11
electric field, 54
electroluminescence, 54, 55
electrolyte, 6
electromechanical coupling, vii, 2, 14
electron, 28, 31
electron microscopy, 28
emission, viii, 53, 55, 56, 59, 60, 61, 62, 63, 64, 65, 66, 67
energy, viii, 9, 36, 41, 53, 55, 59, 61, 62, 63, 64, 65, 66, 67, 72, 80, 83, 84, 88, 89, 91
energy transfer, viii, 53, 55, 59, 61, 63, 64, 65, 66, 67
entropy, 5, 73, 91
equilibrium, 5, 9, 31, 72, 73, 76, 83, 88
equipment, 11, 21
etching, 3
evacuation, 17
evolution, viii, 26, 40
excitation, 30

F

fabrication, 3, 6, 9, 13, 17
fatty acids, 73
films, 55, 61
filters, vii, 1
financial, 47
financial support, 47
fluid, 6, 88
fluorescence, 29, 62, 66
force, 17, 82

formation, 4, 17, 27, 54, 58, 83, 89
France, 1, 17, 20
free energy, ix, 5, 71, 72, 75, 78, 80, 83, 84, 89, 91
fructose, 81

G

geometry, 17
germanium, 15, 17, 18, 20, 90
Germanium Oxide, vii, 2, 11
glass transition, 27
glasses, 27, 31
glucose, 83, 87
growth, vii, viii, ix, 1, 2, 3, 4, 5, 6, 7, 8, 9, 15, 17, 18, 19, 21, 22, 25, 26, 27, 28, 30, 32, 36, 37, 38, 40, 47, 55, 58, 61, 71, 72, 73, 74, 75, 76, 77, 78, 79, 81, 82, 83, 84, 85, 86, 87, 88, 89, 90, 91, 92
growth mechanism, viii, 5, 26, 28
growth rate, 6, 7, 8, 9, 19, 36, 41, 72, 74, 77, 79, 80, 81, 82, 83, 84, 87, 88, 89, 92

H

Hamiltonian, 31
height, 56, 57, 58
host, viii, 53, 55, 58, 59, 60, 61, 66
hybrid, 31
hydrogen, 6, 40, 83
hydrogen atoms, 40
Hydrothermal crystal growth, vii, 1, 4, 5, 7, 19
hydrothermal process, vii, 1, 4, 5, 6
hydrothermal system, 5, 7, 21
hydroxyl, 83
hydroxyl groups, 83
hypothesis, 83

I

ideal, 63
image(s), 56, 57, 58, 82
impurities, ix, 11, 13, 15, 71, 72, 73, 74, 76, 83, 89, 90, 92
industries, 8
industry, 11
inhibition, 80
inhomogeneity, vii, 2, 15
integration, 72, 88
interface, viii, ix, 6, 7, 20, 26, 28, 33, 34, 35, 37, 38, 39, 40, 71, 72, 73, 74, 83, 88
intermolecular interactions, 54, 55, 59
ions, 15, 22, 32, 36, 42, 44, 46
irradiation, 64
isomerization, viii, 26, 37, 38, 39, 40, 47
issues, 54

J

joints, 17

K

kinetic model, 91
kinetics, ix, 4, 5, 18, 19, 71, 79, 82, 84, 89, 90, 91, 92
kinks, 72, 78, 80

L

laser radiation, 28
lasers, 29, 38, 44, 54, 55, 60
lasing threshold, 61
lattice parameters, 57
lattices, 58
leakage, 17
lens, 30
lifetime, 67, 75
light, 28, 29, 30, 54, 55, 60, 63
liquid phase, 3, 11
liquids, 32
low temperatures, 4
luminescence, 54, 55, 60
luminescent efficiencies, viii, 53, 60, 61
luminescent materials, viii, 25
Luo, 48

M

macromolecules, 73, 83, 89
magnetic resonance, 28
magnitude, 6, 7
management, 19
manufacturing, 11
mass, 5, 7, 26
materials, vii, viii, 1, 3, 4, 7, 11, 13, 15, 19, 25, 26, 32, 54, 55
matrix, 15
matter, 72
measurement, 35, 38, 39, 74
media, 9
melt, viii, 2, 25, 26, 27, 28, 29, 30, 31, 32, 34, 35, 36, 37, 38, 39, 40, 41, 42, 43, 44, 45, 46, 47, 74, 90
melting, vii, 1, 16, 26, 35, 36, 40, 42, 44, 45
melting point(s), vii, 1, 16, 35, 40, 45
melts, viii, 25, 26, 27, 30, 31, 32, 35, 38, 40, 41, 44, 47
metal ion(s), 38
Mg^{2+}, 36
microcavity, 54
microscope, 21
microscopy, viii, 53, 55, 82
microstructures, 4
military, 13
models, viii, ix, 26, 71, 73, 80
modifications, 9
mole, 73, 77
molecular mobility, 6
molecular orientation, 81
molecular structure, 55, 56
molecular weight, 73, 86, 91
molecules, viii, 8, 53, 54, 55, 57, 58, 59, 60, 61, 62, 65, 66, 74, 78, 80, 83, 88
monolayer, 57, 58
morphology, 3, 4, 6, 36, 37, 72, 89

N

nano-crystals, 55
nanoparticles, 3
nickel, 17
nitrides, 3
Nobel Prize, 28
nuclear magnetic resonance, 28, 49
nucleation, ix, 71, 78, 81, 82, 90, 91, 92
nucleus, 75
nutrient, 5, 7, 11, 18, 19, 20, 22

O

oligomers, 54
optical properties, viii, 53
ordered layer structures, viii, 53, 57
oscillators, 13
overlap, 54, 55
oxidation, 4
oxygen, viii, 9, 13, 26, 30, 34, 35, 38, 40, 41, 42, 44, 45, 47

P

parallel, 22, 41, 57, 89
partition, ix, 71, 74, 75, 90
passivation, 8
peptide, 73
perforation, 19
permission, 87
petroleum, 53
phase diagram, 9, 11, 15, 17
phase transformation, 2
phase transitions, 2, 3, 4, 9, 22
phosphate, 6, 91
phosphates, 3
photographs, 56, 60, 61
photoluminescence, 63
physical properties, viii, 6, 25
piezoelectric materials, vii, 1
piezoelectric properties, 13, 15, 17, 22
piezoelectricity, 11, 22
PL spectrum, 64
platinum, 30, 35, 37
polar, 6
polarity, 6
polymer(s), viii, 26, 42, 45, 54, 73

population, 40
preparation, 4, 18, 20
probe, 21
programming, 17
project, 83
propagation, 61
proportionality, 88
protein crystallization, 91
pure water, 9, 18, 20
purity, 9, 73, 74

Q

quantum yields, 59
quartz, vii, 2, 3, 4, 8, 9, 10, 11, 12, 13, 15, 16, 17, 18, 19, 20, 22, 61

R

radiation, 28, 29, 38
radius, 75
Raman spectra, viii, 26, 30, 31, 32, 34, 35, 37, 38, 39, 40, 42, 43, 45, 46, 47
Raman spectroscopy, viii, 25, 28, 30, 40, 41, 44, 47, 49
reasoning, 84
recrystallization, ix, 6, 15, 54, 71, 73
red shift, 59
regression, 83, 85
rejection, 74
researchers, vii, 2
resolution, 28, 29, 30
response, 31
retardation, 72, 76, 79, 83, 88
rings, viii, 25, 32, 33, 35, 36, 37, 38, 39, 40, 41, 44, 47
room temperature, 6, 28, 32
Russia, 13
rutile, 15, 16, 18

S

saturation, 73
scaling, 40
scattering, 28, 29, 30
scattering intensity, 29
science, 89
security, 17, 21
sediments, 13
seed, 5, 6, 7, 18, 19, 20
segregation, 74
semiconductor(s), 54
semiconductor lasers, 54
sensitivity, 28
sensors, 13, 17
shape, ix, 43, 46, 56, 71, 72, 78, 89
signals, 29
signal-to-noise ratio, 29
silica, 9
silicon, 9, 11, 18, 90
simulation, 40
single crystals, vii, 2, 3, 4, 5, 6, 8, 13, 17, 19, 22, 54
sintering, 4
SiO2, v, vii, 1, 2, 8, 9, 10, 11, 12, 13, 14, 15, 16, 17, 18, 19, 20, 22
sodium, 3, 6, 15, 17
sodium hydroxide, 6
software, 31, 40
solid solutions, 15, 20
solid state, 54, 73
solubility, 3, 5, 6, 7, 9, 15, 18, 20, 73, 83, 84
solution, viii, ix, 2, 3, 5, 7, 15, 19, 26, 37, 39, 40, 47, 59, 71, 72, 73, 74, 76, 77, 80, 83, 87, 90, 91
solvents, 3, 5, 8, 22, 90
species, 6, 19, 20, 74, 75, 91
specific adsorption, 88
spectroscopic techniques, 29
spectroscopy, 28, 32, 47, 66
spin, 55
stability, vii, 1, 9, 13, 17, 32
state(s), 4, 9, 15, 60, 66
steel, 7, 17, 30
stoichiometry, 11
stress, 20
stretching, 41, 42, 44, 46
strong interaction, 5
structural changes, 40

structural defects, 11
structural modifications, 90
structural transitions, 4
structure, vii, viii, 2, 10, 11, 13, 14, 15, 16, 17, 20, 26, 27, 28, 30, 32, 33, 34, 35, 36, 40, 41, 42, 43, 44, 54, 55, 58, 59, 66, 72, 80, 90
substitution, 15, 17
substrate(s), 44, 61
succession, 55
sucrose, ix, 71, 73, 74, 75, 79, 81, 82, 83, 84, 85, 86, 87, 88, 89, 90, 91
supercooling, 6
suppression, 78
surface tension, 27
surfactant(s), 73, 84
synthesis, 6
Syria, 71

T

techniques, vii, viii, 1, 2, 4, 5, 9, 25, 27, 28
technology, 4
temperature, vii, viii, 2, 3, 4, 5, 6, 7, 9, 11, 13, 16, 17, 18, 20, 22, 25, 26, 27, 28, 29, 30, 32, 35, 37, 38, 40, 41, 44, 47, 49, 61, 73, 78, 81
terraces, 80
thermal decomposition, 4
thermal expansion, 7
thermal stability, 2, 17, 54
thermal strain, vii, 1, 11
thermodynamical parameters, 11
thermodynamics, 91
time control circuits, vii, 1
time resolution, 29
total energy, 31
toxicity, vii, 2, 6
transformation(s), 13, 16, 18, 26, 42, 47
transition temperature, 9, 15
transmission, 28
transmission electron microscopy, 28
transparency, 38, 41
transport, viii, 5, 6, 19, 20, 26, 28, 53, 55, 66

U

uniform, 9, 18
universal gas constant, 73

V

vacuum, 55
valence, 15
valve, 21
vapor, viii, 2, 53, 55, 59, 66
variables, 78, 80
variations, 81
velocity, 76, 79
vessels, 5, 7, 17
vibration, 39, 42, 44, 46
viscosity, 6, 26, 27
volatilization, vii, 2

W

war, 4
Washington, 49
water, 3, 6, 7, 15, 18, 20, 30, 84, 86
wavelengths, 59, 61, 66, 67
weakness, 30
workers, 31
worldwide, vii, 2

X

X-ray diffraction(XRD), viii, 28, 53, 55, 57, 58, 66

Y

yield, 4, 62